

AD-A269 995



12

The Pennsylvania State University
APPLIED RESEARCH LABORATORY
P.O. Box 30
State College, PA 16804

ACOUSTIC INTENSITY MEASUREMENTS IN THE
PRESENCE OF LOW MACH NUMBER FLOW

by

T. McNeal
G. C. Lauchle

Technical Report No. TR 93-11
September 1993

DTIC
ELECTE
SEP 29 1993
S B D

Supported by:
Naval Surface Warfare Center

L.R. Hettche, Director
Applied Research Laboratory

Approved for public release; distribution unlimited

93-22537



93 9 29 053

REPORT DOCUMENTATION PAGE

FORM 107-100-100

OMB No. 0704-0157

Public reporting burden for this collection of information is estimated to average 1 hour per response, including the time for reviewing instructions, searching existing data sources, gathering and maintaining the data needed, and completing and reviewing the collection of information. Send comments regarding this burden estimate or any other aspect of this collection of information, including suggestions for reducing this burden, to Washington Headquarters Services, Directorate for Information Operations and Reports, 1215 Jefferson Davis Highway, Suite 1204, Arlington, VA 22202-4302, and to the Office of Management and Budget, Paperwork Reduction Project (0704-0157), Washington, DC 20503.

1. AGENCY USE ONLY (Leave blank)		2. REPORT DATE September 1993		3. REPORT TYPE AND DATES COVERED	
4. TITLE AND SUBTITLE ACOUSTIC INTENSITY MEASUREMENTS IN THE PRESENCE OF LOW MACH NUMBER FLOW				5. FUNDING NUMBERS	
6. AUTHOR(S) Toby McNeal and G. C. Lauchle					
7. PERFORMING ORGANIZATION NAME(S) AND ADDRESS(ES) Naval Surface Warfare Center Acoustic Research Detachment Code 752 P.O. Box 129 Bayview, ID 83803-0129				8. PERFORMING ORGANIZATION REPORT NUMBER TR-93-11	
9. SPONSORING/MONITORING AGENCY NAME(S) AND ADDRESS(ES) Naval Surface Warfare Center Acoustic Research Detachment Code 752 P.O. Box 129 Bayview, ID 83803-0129				10. SPONSORING/MONITORING AGENCY REPORT NUMBER	
11. SUPPLEMENTARY NOTES					
12a. DISTRIBUTION/AVAILABILITY STATEMENT Unlimited				12b. DISTRIBUTION CODE	
13. ABSTRACT (Maximum 200 words) Acoustic intensity is an important analysis tool since it provides wave propagation directionality along with absolute magnitude, and it can be measured in the near or far field of a source. Acoustic intensity measurements acquired in the presence of a mean flow are susceptible to errors due to the effects of the flow noise on the sensor. To determine if this error could be accurately quantified, intensity measurements were acquired, with the standard two microphone cross spectral technique, in a sound field that contained both mean flow and an independent random broadband noise source. The microphones were flush mounted, at several different separation distances, in the test section of a wind tunnel that provided the desired flow conditions, while a large speaker provided the independent random noise source. The error calculations were based on a technique that had already been derived theoretically and published, but had not been proven experimentally. The experiments performed validate that the error is indeed a bias error and that it can be accurately quantified. In addition, accurate quantification of the error is not limited to one-dimensional sound fields that contain only plane waves, and the method can be easily extended to two or three directions with complex wave propagation.					
14. SUBJECT TERMS acoustic intensity, low mach number, flow, two microphone, cross spectral, wind tunnel				15. NUMBER OF PAGES 99	
				16. PRICE CODE	
17. SECURITY CLASSIFICATION OF REPORT Unclassified	18. SECURITY CLASSIFICATION OF THIS PAGE Unclassified	19. SECURITY CLASSIFICATION OF ABSTRACT Unclassified	20. LIMITATION OF ABSTRACT		

ABSTRACT

Acoustic intensity is an important analysis tool since it provides wave propagation directionality along with absolute magnitude, and it can be measured in the near or far field of a source. Acoustic intensity measurements acquired in the presence of a mean flow are susceptible to errors due to the effects of the flow noise on the sensor. To determine if this error could be accurately quantified, intensity measurements were acquired, with the standard two microphone cross spectral technique, in a sound field that contained both mean flow and an independent random broadband noise source. The microphones were flush mounted, at several different separation distances, in the test section of a wind tunnel that provided the desired flow conditions, while a large speaker provided the independent random noise source. The error calculations were based on a technique that had already been derived theoretically and published, but had not been proven experimentally. The experiments performed validate that the error is indeed a bias error and that it can be accurately quantified. In addition, accurate quantification of the error is not limited to one-dimensional sound fields that contain only plane waves, and the method can be easily extended to two or three directions with complex wave propagation.

TABLE OF CONTENTS

LIST OF FIGURES	vi
LIST OF TABLES	viii
LIST OF SYMBOLS	ix
ACKNOWLEDGEMENTS	xii
CHAPTER 1. HISTORICAL BACKGROUND AND OBJECTIVES	1
1.1 Introduction	1
1.2 Historical Background	2
1.3 Research Objectives and Scope	4
CHAPTER 2. THE FUNDAMENTAL THEORY OF ACOUSTIC INTENSITY	6
2.1 Introduction and Definition	6
2.2 Derivation of the Estimators	9
CHAPTER 3. INTENSITY MEASUREMENT ERRORS AND THEIR ESTIMATION	14
3.1 Introduction	14
3.2 Bias Error	16
3.2.1 Finite Difference Approximation Errors	16
3.2.2 Near-Field Errors	21
3.2.3 Phase Errors	23
3.3 Random Errors	25
3.4 Quantifying and Minimizing Errors	28
3.4.1 Calibration	28
3.4.2 Pressure Intensity Indices	31
CHAPTER 4. ACOUSTIC INTENSITY MEASUREMENT CONSIDERATIONS IN THE PRESENCE OF FLOW	34

4.1	Background and Theory	34
4.2	Measurements with Flush Mounted Sensors	36
CHAPTER 5. MEASUREMENT TECHNIQUE AND EXPERIMENTAL FACILITY		41
5.1	Introduction	41
5.2	Facility	43
5.3	Measurement Considerations	44
5.4	Instrumentation	46
5.5	Calibration and Finite Difference Approximation Error ..	48
CHAPTER 6. EXPERIMENTAL RESULTS		51
6.1	An introduction to the Technique	51
6.2	The Bias Error	58
6.3	The Intensity Spectrum	58
6.4	The Non-Dimensionalized Bias Error	60
6.5	Pressure Intensity Indices	61
CHAPTER 7. CONCLUSIONS		63
7.1	Overview of the Results	63
7.2	Conclusions From the Bias Error Calculations	65
7.3	Conclusions From the Intensity Spectra	67
7.4	Conclusions From the Pressure Intensity Indices	68
7.5	Summary and Recommendations	69
REFERENCES		71
APPENDIX A. BIAS ERROR PLOTS		74
APPENDIX B. ACTIVE INTENSITY PLOTS		81
APPENDIX C. PRESSURE INTENSITY INDEX OVERLAY PLOTS ...		92

Accession For	
NTIS GRA&I	<input checked="" type="checkbox"/>
DTIC TAB	<input type="checkbox"/>
Unannounced	<input type="checkbox"/>
Justification	
By	
Distribution/	
Availability Codes	
Dist	Avail and/or Special
A-1	

LIST OF FIGURES

Figure 2.1	Microphone orientation.	11
Figure 3.1	Illustration of the error due to finite difference approximation	17
Figure 4.1	Illustration of boundary layer flow over a flat surface that contains flush mounted acoustical pressure measurement sensors	37
Figure 5.1	The Pennsylvania State University, Applied Research Laboratory, Subsonic wind tunnel	43
Figure 5.2	Microphone orientation in the wind tunnel test section	45
Figure 5.3	Experiment instrumentation set-up	47
Figure 5.4	Error in intensity level resulting from the finite difference approximation for the case of a plane wave, for three separation distances	50
Figure 6.1	Non Dimensionalized bias error for intensity estimate	52
Figure 6.2	Relationship between turbulence correlation length, Λ , sensor separation, Δr , frequency, and the non-dimensional quantity $k_c \Delta r$	54
Figure 6.3	Autospectral density functions for turbulent pressure	56
Figure 6.4	Cross-spectral density function comparisons	57
Figure 7.1	Verification that the calculated errors are bias errors	64
Figure A-1	Bias Error, 6 m/s flow, $\Delta r = 25.4$ mm	75
Figure A-2	Bias Error, 6 m/s flow, $\Delta r = 50.8$ mm	75
Figure A-3	Bias Error, 9 m/s flow, $\Delta r = 13.5$ mm	76
Figure A-4	Bias Error, 9 m/s flow, $\Delta r = 25.4$ mm	76
Figure A-5	Bias Error, 9 m/s flow, $\Delta r = 50.8$ mm	77

Figure A-6	Bias Error, 18 m/s flow, Delta $r = 13.5$ mm	78
Figure A-7	Bias Error, 18 m/s flow, Delta $r = 50.8$ mm	78
Figure A-8	Bias Error, 30.5 m/s flow, Delta $r = 13.5$ mm, 0-2500 Hz	79
Figure A-9	Bias Error, 30.5 m/s flow, Delta $r = 13.5$ mm, 0-5000 Hz	79
Figure A-10	Bias Error, 30.5 m/s flow, Delta $r = 50.8$ mm	80
Figure B-1	Active Intensity, 6 m/s flow, Delta $r = 25.4$ mm	82
Figure B-2	Active Intensity, 6 m/s flow, Delta $r = 50.8$ mm	83
Figure B-3	Active Intensity, 9 m/s flow, Delta $r = 13.5$ mm	84
Figure B-4	Active Intensity, 9 m/s flow, Delta $r = 25.4$ mm	85
Figure B-5	Active Intensity, 9 m/s flow, Delta $r = 50.8$ mm	86
Figure B-6	Active Intensity, 18 m/s flow, Delta $r = 13.5$ mm	87
Figure B-7	Active Intensity, 18 m/s flow, Delta $r = 50.8$ mm	88
Figure B-8	Active Intensity, 30.5 m/s flow, Delta $r = 13.5$ mm	89
Figure B-9	Active Intensity, 30.5 m/s flow, Delta $r = 13.5$ mm	90
Figure B-10	Active Intensity, 30.5 m/s flow, Delta $r = 50.8$ mm	91
Figure C-1	Intensity Indices, no flow, Delta $r = 13.5$ mm	93
Figure C-2	Intensity Indices, 9 m/s flow, Delta $r = 13.5$ mm	94
Figure C-3	Intensity Indices, no flow, Delta $r = 25.4$ mm	95
Figure C-4	Intensity Indices, 9 m/s flow, Delta $r = 25.4$ mm	96
Figure C-5	Intensity Indices, no flow, Delta $r = 50.8$ mm	97
Figure C-6	Intensity Indices, 9 m/s flow, Delta $r = 50.8$ mm	98
Figure C-7	Intensity Indices, 30.5 m/s flow, Delta $r = 50.8$ mm	99

LIST OF TABLES

Table 3.1	Minimum distance between source and receive sensors for a nearfield error less than 1 dB.	22
Table 6.1	Parameters associated with the bias error data of appendix A	59
Table 6.2	Pressure Intensity Indices data included in Appendix C	62

LIST OF SYMBOLS

\bar{a}	Particle acceleration
$b[]$	Bias error
B	Frequency bandwidth
c	Sonic speed also called speed of sound
$E[]$	Expectation operator, Expected value of $[]$
f	Frequency, Hz
G_{11}	One-sided autospectral density function for sensor 1
G_{22}	One-sided autospectral density function for sensor 2
G_{12}	One-sided cross-spectral density function between sensors 1 and 2
G_{TT}	One-sided autospectral density function for turbulent pressure
$G_{T_1T_2}$	One-sided cross-spectral density function for turbulent pressure
\hat{G}	Estimate of one-sided spectral density function
\bar{I}	Active intensity vector
\bar{I}_i	Instantaneous intensity vector
I_r	Active intensity component in r-direction
\hat{I}_r	Estimate of active intensity in r-direction
$\text{Im}[]$	Imaginary part
\bar{J}	Reactive intensity
\hat{J}	Estimate of reactive intensity
k	Acoustic wavenumber

k_c	Convection wavenumber
L_{ϵ_f}	Level, in dB, of finite difference approximation error
$L_{\epsilon_{\Delta\phi}}$	Level, in dB, of instrumentation phase mismatch error
L_i	Intensity level in dB re $1\text{pW}/\text{m}^2$
L_p	Pressure level in dB re $20\text{ }\mu\text{Pa}$
M	Mach number
M_c	Convective Mach number
n_d	Number of distinct sample records
p	Total pressure
p_a	Acoustic pressure
p_T	Turbulence pressure
r	An arbitrary direction, r-direction
Re	Reynolds number
S	Surface of interest
T	Averaging Time
u	Local flow velocity
u_o	Mean background flow velocity
u_c	Convection velocity
\vec{u}	Particle velocity vector
u_r	Particle velocity in r-direction
\hat{u}	Estimate of particle velocity
W	Acoustic power

Greek Symbols

ΔL_i	The calculated bias error in an intensity estimate acquired in flow
Δr	Sensor separation distance
$\Delta\alpha$	Instrumentation phase mismatch
$\delta(x_i)$	Boundary layer thickness as function of streamwise coordinate, x_i
δ_{pi}	Pressure intensity index
δ_{piR}	Residual pressure intensity index
ε_b	Normalized bias error
ε_r	Normalized random error
Λ	Turbulence correlation length
γ^2	Ordinary coherence function
λ	Wavelength
ν	Kinematic viscosity
ϕ_p	Phase angle of acoustic pressure
ϕ_u	Phase angle of particle velocity
$\nabla\phi_p(r)$	Acoustic pressure spatial phase gradient
Φ	Arbitrary error quantity
ρ_o	Ambient fluid density
σ	Standard deviation
$\sigma[]$	Random error
ω	Radian frequency

CHAPTER 1

HISTORICAL BACKGROUND AND OBJECTIVES

1.1 Introduction

The theory of acoustic intensity has been established for many years as evidenced by the absence of new papers in technical journals that emphasize fundamental aspects of acoustic intensity. In addition, with modern electronics, the measurement of sound intensity in air has been proven to be practical and reliable.

Major applications of sound intensity measurements in widespread use today include the determination of sound power output from individual sources in the presence of others, source localization, and mapping of the sound field. Recent research in the area has concentrated largely on new innovative applications of intensity measurements and minor enhancements to existing measurement techniques.

Examples of intensity measurement applications which are less developed and are the focus of more current research include structural intensity^{1,2} (or structural power flow), near field intensity measurements for broadband acoustic holography,³ intensity measurements in the presence of flow,^{4,5,6,7} in-situ evaluation of the acoustic impedance and sound absorption properties of materials, and underwater sound

intensity measurements.

The experimental research discussed in this paper deals with intensity measurements from flush mounted microphones in the presence of low Mach number flow.

1.2 Historical Background

Attempts to measure the flow of sound energy go back many years. In 1932 a patent was granted to Harry Olson of the Radio Corporation of America for a "System responsive to the energy flow of sound waves".⁸ This device utilized a pressure microphone and a particle velocity microphone. The device apparently did not achieve practical utilization however, and in 1941, Clapp and Firestone⁹ constructed an acoustic wattmeter to measure the flow of sound energy. In their journal article describing the device, they stated that the term sound intensity was discussed often and was the basis for the measurement of loudness level, but to their knowledge, there were no previous attempts to measure sound intensity directly. Their acoustic wattmeter consisted of a crystal pressure microphone and a small ribbon velocity microphone, connected through separate amplifiers and phase equalizing networks. The device could be calibrated up to 2000 Hz and was reported to perform relatively well at measuring sound fields in standing wave tubes. It was also noted that considerable problems and consequent errors were

encountered as a result of ribbon resonances in the velocity microphone. These were however corrected by suitable electronic networks.

Many years passed without further mention of these devices. This led many to conclude that subsequent use proved them to be inadequate. Thus for many years theoretical analysis of sound intensity continued but seldom were measurements of sound intensity acquired.

Schultz,¹⁰ in 1956, constructed an instrument that gave pointer indications of acoustic intensity over a 50 dB range and at frequencies up to 10,000 Hz. He implemented a principle developed by Bolt and Petrauskas¹¹ (in 1943) whereby two pressure microphones were used to obtain a velocity estimate. With this technique Schultz generated the particle velocity signal by integrating the difference between two closely spaced pressure microphone outputs, and utilizing the linearized Euler equation to relate the pressure gradient and the particle velocity. Schultz obtained satisfactory results under ideal laboratory conditions but the results from other measurements were disappointing. One of the key problems was the demand placed on the electronic circuitry of the time.

The work by Schultz, Bolt, and Petrauskas, was the foundation for many of the future developments in acoustic intensity measurements. With later demonstration of the relationships between the active and reactive components of intensity and the spatial gradients of phase and

squared pressure, plus advances in digital signal processing, led to a surge of developments in the mid to late 1970's. In this time, FFT analyzers were developed, electronic circuitry improved considerably, and sound intensity meters were developed. Techniques were further refined and measurement errors were quantified.

Since the late 1970's advances have continued but most have merely improved upon and expounded the two pressure sensor measurement technique. This method of measuring sound intensity remains the most frequently used and usually the most practical method for acquiring field measurements of sound intensity and sound power. Improvements in electronics and digital signal processing also continue to make sound intensity measurements more feasible, reliable, accurate, and commonplace.

1.3 Research Objectives and Scope

This paper is divided into seven chapters. The first chapter provides an introduction to acoustic intensity along with some historical background.

The second chapter reviews the fundamental theory and basic relationships before providing a derivation of the estimators used to measure acoustic intensity.

Chapter 3 then discusses the considerations that need to be taken

into account when acquiring acoustic intensity data. These considerations include errors inherent in the measurement technique, and calibration.

Chapter 4 contains a brief discussion of measurement considerations in the presence of flow.

In Chapter 5 a description of the experiment performed for this research is presented. The specifics of the experiment, the test facility, instrumentation, calibration, and measurement techniques are explained.

Chapter 6 then presents and explains the results of the experiment.

Chapter 7 concludes the report with some final comments and recommendations.

CHAPTER 2

THE FUNDAMENTAL THEORY OF ACOUSTIC INTENSITY

2.1 Introduction and Definition

Urick¹² gives a thorough definition of acoustic intensity as follows:

A propagating sound wave carries mechanical energy with it in the form of the kinetic energy of the particles in motion plus the potential energy of the stresses set up in the elastic medium. Because the wave is propagating, a certain amount of energy per second will flow across a unit area oriented normal to the direction of propagation. This amount of energy per second (power) crossing a unit area is the *intensity* of the wave.

Thus it is apparent that sound waves transport energy and the intensity is merely the energy per second that crosses a unit area. The unit of intensity is thus W/m^2 or power per unit area. A relationship of intensity to pressure and particle velocity can easily be seen from a simple units comparison¹³ shown below.

$$\text{Intensity} = \frac{\text{Power}}{\text{Area}} = \frac{\text{Energy}}{\text{Area} * \text{Time}} = \frac{\text{Force} * \text{Distance}}{\text{Area} * \text{Time}} = \text{Pressure} * \text{Vel}$$

Sound intensity is a vector quantity describing both magnitude and direction of the net flow of acoustic energy at a given location.

Measurements of intensity are usually done in a direction normal to a specified unit area through which the sound energy is flowing. Intensity measurements can provide a complete analysis of sound radiation and

propagation.

Sound fields will usually (except for the special case of a plane progressive wave) contain both active and reactive components. The active component corresponds to a local net transport of sound energy while the reactive component represents a local oscillatory transport of energy and thus no net flow of energy. The instantaneous intensity may be split up into these two components (an active component and a reactive component) where the total instantaneous intensity can be expressed as:¹⁴

$$\vec{I}_i = p \cdot \vec{u} \quad (2.1)$$

The arrow indicates a vector quantity, $p = p(r, t) = P(r)\exp[i(\omega t + \phi_p(r))]$ is the total acoustic pressure, and $\vec{u} = \vec{u}(r, t) = U(r)\exp[i(\omega t + \phi_u(r))]$ is the particle velocity. As commonly defined, $P(r)$ and $U(r)$ are the spatial pressure and velocity amplitudes in the direction of wave propagation, and ϕ_p and ϕ_u are the corresponding phases. The explicit indication of time, t , and general spacial dependence, r , will usually be suppressed for convenience. The symbol ϕ represents the respective phase.

The time average complex intensity is^{14,15}

$$\vec{I}^c = \frac{1}{2} p \cdot \vec{u}^* = \vec{I} + i\vec{J} \quad (2.2)$$

where \vec{u}^* is the complex conjugate of \vec{u} , \vec{I} is the active intensity, and \vec{J}

is the reactive intensity. From equation (2.2), and the forms of p and \vec{u} ,

$$\vec{I} = \frac{1}{2} \text{Re}[p \cdot \vec{u}^*] = \frac{1}{2} P \cdot U \cos(\phi_p - \phi_u) \quad (2.3)$$

and

$$\vec{J} = \frac{1}{2} \text{Im}[p \cdot \vec{u}^*] = \frac{1}{2} P \cdot U \sin(\phi_p - \phi_u) \quad (2.4)$$

The active intensity component represents the magnitude and direction of the acoustic energy propagation through space, and is the in-phase time average product of the pressure and particle velocity. It describes the time averaged power flux through a point and is proportional to the acoustic pressure spacial phase gradient¹⁶, denoted by $\nabla\phi_p(r)$. This is apparent since the active intensity vector points in a direction perpendicular to surfaces of constant pressure phase or wavefronts. The active intensity is high in regions where the wavefronts are compressed and consequently where the squared pressure amplitude $P^2(r)$ is large.¹⁶ The active intensity is the primary concern in this research and will be the focus of most of this paper. An example of a purely active sound field is a plane wave propagating in free space.

The reactive intensity represents acoustic energy that does not propagate, and is the time average product of the pressure and the phase quadrature component of the particle velocity. It is proportional

to the spacial gradient of the pressure amplitude,¹⁶ is generally high in the nearfield, and points toward pressure minima (and away from pressure maxima). The reactive intensity indicates the presence of standing waves or the direction of the nearfield components of the reactive field. Examples of reactive sound fields are an ideal standing wave, an ideal diffuse sound field where the energy flow at a given location is the same in all directions, and the nearfield of simple and complex sources. Measurements in the nearfield have the benefit of increased signal-to-noise and are often used for source localization and sound power determination. The reactive intensity is also crucial in distinguishing between "hard" sources and "soft" sources in air-borne noise,¹⁶ where a "hard" source may be a steel plate or machine, and a "soft" source may be sound radiating from an opening such as a tube termination.

2.2 Derivation of the Estimators

Since the instantaneous intensity vector, \vec{I} , is the net rate of flow of energy per unit area at a given position, the acoustic power, W , passing through a surface, S , is:

$$W = \int_{\vec{S}} \vec{I} \cdot d\vec{S} = \int_S I_n \cdot dS \quad (2.5)$$

where I_n is the vector component normal to the surface, S.

In a medium without flow the intensity vector equals the time averaged product of the instantaneous pressure and the corresponding instantaneous particle velocity at the same position.

$$\vec{I} = \overline{p \cdot \vec{u}} \quad (2.6)$$

where the bar indicates time averaging. In a specific direction, r, this can be expressed as:

$$I_r = \overline{p \cdot u_r} \quad (2.7)$$

The sound pressure can be measured directly, but an accurate direct measurement of the particle velocity is very difficult. However, from Euler's equation, which is based on Newton's second law ($F=ma$), we know that for a sound field propagating in a fluid, the particle acceleration, \vec{a} , is given by the ratio of the pressure gradient to the fluid density, ρ_0 :

$$\vec{a} = - \frac{1}{\rho_0} \frac{\partial p}{\partial r} \quad (2.8)$$

or equivalently,

$$\frac{\partial \vec{u}}{\partial t} = - \frac{1}{\rho_0} \frac{\partial p}{\partial r} \quad (2.9)$$

and in a specific direction, r,

$$u_r = -\frac{1}{\rho_0} \int \frac{\partial p}{\partial r} dt \quad (2.10)$$

The pressure gradient is a continuous function which in practice can be approximated by measuring the pressures, p_1 and p_2 , at two closely spaced points and dividing the pressure difference ($p_2 - p_1$) by the transducer separation distance Δr (see Figure 2.1). This is commonly

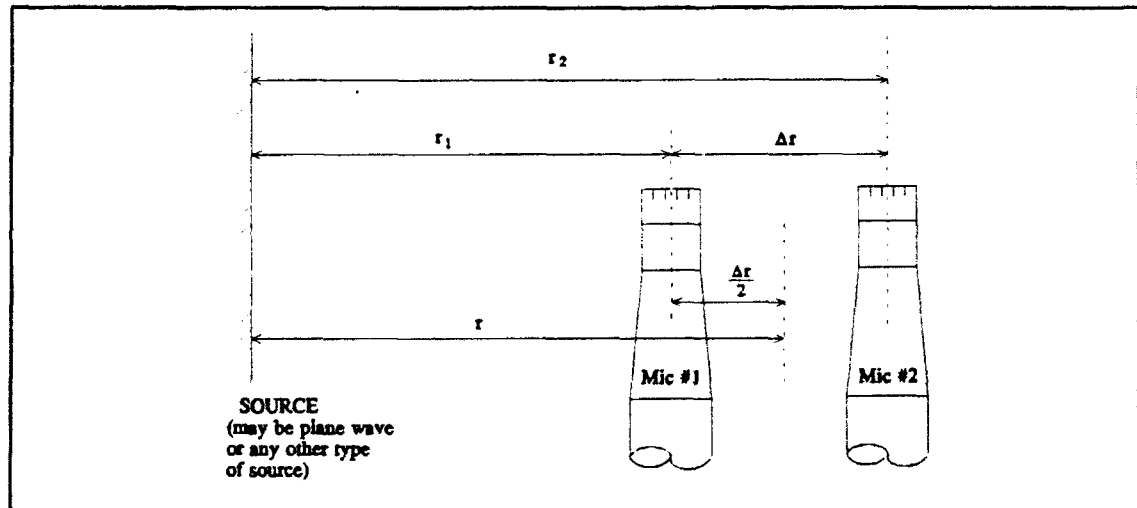


Figure 2.1 Microphone Orientation (From reference [24])

referred to as the finite difference approximation and is valid as long as the sensor separation, Δr , is small compared with the wavelength ($\Delta r \ll \lambda$). Thus the pressure gradient can be approximated as

$$\frac{\partial p}{\partial r} \approx \frac{(p_2 - p_1)}{\Delta r} \quad (2.11)$$

Therefore, the estimate for the particle velocity component, \hat{u}_r , in the direction r becomes:

$$\hat{u}_r = -\frac{1}{\rho_o \Delta r} \int (p_2 - p_1) dt \quad (2.12)$$

where the carrot (^) symbol over the quantity u_r , denotes an estimate of that quantity.

Equation 2.11 gives an approximation for the pressure gradient at the center of the microphone pair. The pressure at this point is estimated from the average pressures of the two microphones:

$$\hat{p} = \frac{(p_1 + p_2)}{2} \quad (2.13)$$

Substituting equations 2.12 and 2.13 into equation 2.7, the intensity vector component in the direction r is,¹⁷

$$\hat{I}_r = \frac{1}{2\rho_o \Delta r} \overline{(p_1 + p_2) \int (p_1 - p_2) dt} \quad (2.14)$$

Assuming stationary data and utilizing the definition of time averaging equation 2.14 may be written equivalently as,¹⁸

$$\hat{I}_r = \lim_{T \rightarrow \infty} \frac{1}{2\rho_o \Delta r T} \int_0^T \int (p_1 + p_2)(p_1 - p_2) dt d\tau \quad (2.15)$$

Equations (2.14) and (2.15) may be implemented directly using

sum, difference, multiplication, and integration circuits, plus filters (analog or digital). These equations may also be implemented indirectly using FFT analyzers as introduced by Fahy and Chung^{19,20} and demonstrated by others.²¹ This refinement allows a frequency domain representation in terms of the cross spectral density between the two measured pressures as,

$$\hat{I}_r(\omega) = - \frac{\text{Im } G_{12}}{\omega \rho_0 \Delta r} \quad (2.16)$$

where ω is the radian frequency and $\text{Im } G_{12}$ is the one-sided quad spectrum as measured by the pair of pressure transducers.

The reactive intensity spectrum may be expressed as,

$$\hat{J}_r(\omega) = \frac{1}{2\omega\rho_0\Delta r} (G_{11} - G_{22}) \quad (2.17)$$

where G_{11} and G_{22} are the one sided autospectral density functions for microphones 1 and 2 respectively.

It can be inferred correctly from equations 2.16 and 2.17 that the active component of intensity is proportional to the spatial gradient of phase, and the reactive component is proportional to the spatial gradient of mean square pressure.

CHAPTER 3

INTENSITY MEASUREMENT ERRORS AND THEIR ESTIMATION

3.1 Introduction

It is the errors associated with intensity measurements that impose the majority of limitations in sound intensity measurements. These errors originate from many phenomena including instrument *phase mismatch*, *finite difference approximation*, *scattering by transducers and holding fixtures*, *near field effects*, *uncertainty of sensor separation distance*, and *finite sampling*. An understanding of the cause and effect of these errors is critical if reliable measurements are to be obtained.

This chapter will summarize the effects and estimation techniques for those errors most significant in general applications and most applicable to the measurements performed for this research. In addition, it should be recognized that error analysis can usually only be demonstrated for simple cases where the sound field can be precisely described. In most actual measurement scenarios the sound field is unknown and often the fundamental reason for acquiring the measurements. The actual sound field may be quite complicated and hence the error analysis is in general only an approximation. These error approximations do however provide bounds which should always

be considered.

Errors may be divided into two general categories, 1) bias errors, and 2) random errors. Both types are present in acoustic intensity measurements. Before proceeding with an explanation of these errors it will be useful to first define some general error formulas²² that will be applied.

Let a carrot (^) symbol over an arbitrary quantity Φ , namely $\hat{\Phi}$, denote an estimate of the quantity as in chapter 2. The quantity $\hat{\Phi}$ will be an estimate of Φ based on a finite time interval or finite number of sample points. The bias of the estimate, denoted $b[\hat{\Phi}]$ is equal to:

$$\text{bias error} = b[\hat{\Phi}] = E[\hat{\Phi}] - \Phi \quad (3.1)$$

where $E[]$, is the expectation operator.

The standard deviation for the estimate, called the standard error or random error is,

$$\text{random error} = \sigma[\hat{\Phi}] = \sqrt{E[\hat{\Phi}^2] - E^2[\hat{\Phi}]} = \sqrt{\text{Var}[\hat{\Phi}]} \quad (3.2)$$

where σ , indicates standard deviation.

The error may also be defined in terms of a fractional portion of the quantity being estimated. This is done by dividing the error by the quantity being estimated to obtain a normalized error. For $\Phi \neq 0$, the normalized bias and random errors are thus given by,

$$\text{normalized bias error} = \epsilon_b = \frac{b[\hat{\Phi}]}{\Phi} \quad (3.3)$$

$$\text{normalized random error} = \epsilon_r = \frac{\sigma[\hat{\Phi}]}{\Phi} = \frac{\sqrt{\text{Var}[\hat{\Phi}]}}{\Phi} \quad (3.4)$$

where

$$\text{Var}[\hat{\Phi}] = E[\hat{\Phi}^2] - E^2[\hat{\Phi}] \quad (3.4a)$$

3.2 Bias Errors

The bias errors are systematic and represent deviations of the expected value of the estimate from the true or exact values as shown in equation (3.1). Secondary acoustic sources can bias the acoustic intensity even when these sources are uncorrelated with the primary source.²³ Descriptions of the most influential bias errors in intensity measurements will now be provided.

3.2.1 The Finite Difference Approximation Error

With the two microphone measurement technique, the pressure gradient and the pressure at the midpoint between the two microphones are approximated by equations (2.11) and (2.13) respectively. One

source of error from these approximations arises from the fact that the acoustic center, corresponding to the location where the pressure field best matches the microphones output, may not coincide with the geometric center. A secondary uncertainty associated with the acoustic center is that the effective center for the particle velocity approximation may not be the same as the effective center of the mean pressure.

In addition, the pressure gradient approximation will be good for low frequencies where the wavelength, λ , is large compared to the sensor separation, Δr , but will have an increasing error for larger separations or higher frequencies as depicted in figure 3.1.

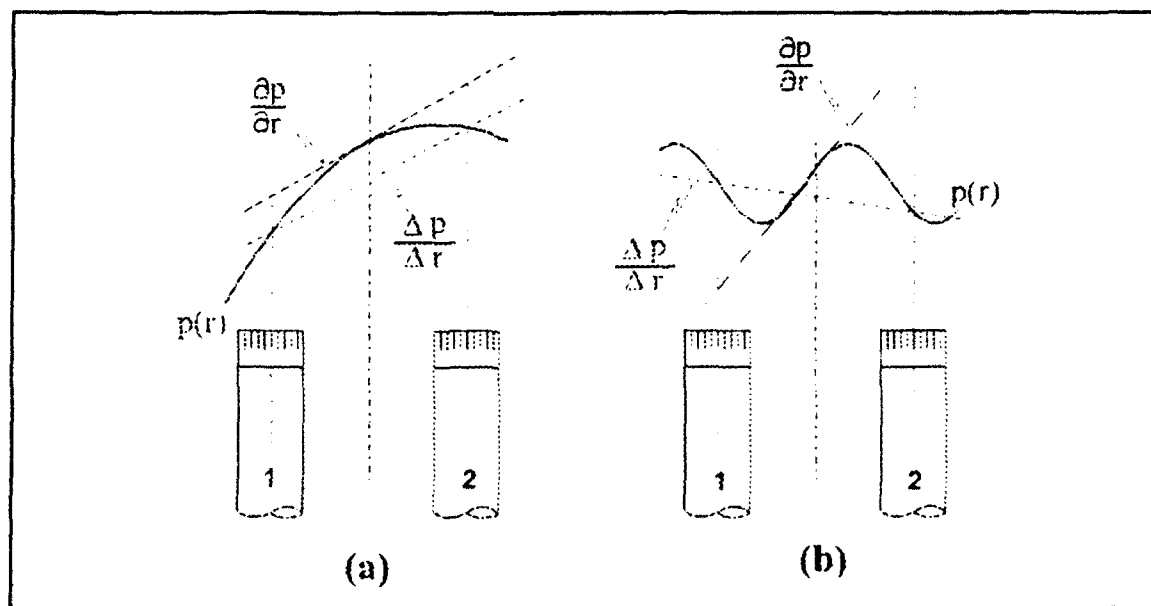


Figure 3.1 Illustration of the error due to finite difference approximation. a) good approximation for low frequencies; b) poor approximation for high frequencies. (From reference [21]).

This approximation error can be demonstrated for various sound fields. First consider the situation where a plane progressive wave propagates in the positive r -direction (see figure 2.1 for orientation). Let the pressures at the two sensors be written as

$$P_{r_1} = P_o e^{-ik(r - \frac{\Delta r}{2})} \quad (3.5)$$

and

$$P_{r_2} = P_o e^{-ik(r + \frac{\Delta r}{2})} \quad (3.6)$$

The true intensity, I_r , is given by

$$I_r = \frac{P_{rms}^2}{\rho c} \quad (3.7)$$

and the measured intensity is given by

$$\hat{I}_r = \frac{P_{rms}^2}{\rho c} \frac{\sin k\Delta r}{k\Delta r} \quad (3.8)$$

The ratio of the measured intensity to the true intensity is thus given by

$$\frac{\hat{I}_r}{I_r} = \frac{\sin k\Delta r}{k\Delta r} \quad (3.9)$$

Thus, the intensity is underestimated, particularly at high frequencies and for large separation distances. The level, in dB, of this bias error for the case of a plane progressive wave would be,

$$L_{\epsilon_f} = 10 \log_{10} \left(\frac{\hat{I}_r}{I_r} \right) = 10 \log_{10} \left(\frac{\sin k\Delta r}{k\Delta r} \right) \quad (3.10)$$

For the case of a monopole source the level of the bias error would be,²⁴

$$L_{\epsilon_f} = 10 \log_{10} \left[\frac{\sin k\Delta r}{k\Delta r} \frac{r^2}{r_1 r_2} \right] \quad (3.11)$$

where the reader is referred to figure 2.1 for a definition of the variables used in this equation. Graphing of equation (3.11) for various values of frequency and separation distance, Δr , reveal that the measurement accuracy is a function not only of $k\Delta r$, but also of $\Delta r/r$. Generally, the finite difference errors are minimized by employing the smallest possible values of $k\Delta r$, and $\Delta r/r$. Thus, even though $k\Delta r$ may be small, errors increase as one moves closer to the source.

The level of the on-axis bias error for a dipole source has been shown to be,²⁴

$$L_{\epsilon_f} = 10 \log_{10} \left[\frac{\sqrt{1 + (kr_1)^2} \sqrt{1 + (kr_2)^2} \sin(k\Delta r + \varphi_1 - \varphi_2)}{k^3 \Delta r r_1 r_2} \frac{r^2}{r_1 r_2} \right] \quad (3.12)$$

where $\varphi_1 = \tan^{-1} (-1/kr_1)$ and $\varphi_2 = \tan^{-1} (-1/kr_2)$. The measurement accuracy for the dipole source is more sensitive to the parameters $k\Delta r$ and $\Delta r/r$, than is the measurement accuracy for a monopole source.

Thus, the range over which accurate measurements may be acquired is significantly lower for the dipole source than for the monopole source.

Thompson and Tree²⁴ also provide an expression for the bias error from a lateral quadrupole from which it can be observed that errors for a quadrupole source are even more sensitive to $k\Delta r$ and $\Delta r/r$, indicating that the effects of these parameters increase with source complexity. In addition, for quadrupole source measurements there are both low frequency and high frequency measurement accuracy limits.

Since sound fields encountered in common measurements vary in complexity, Thompson and Tree²⁴ recommend a good practice is to select measurement parameters based on a worst case scenario, such as the lateral quadrupole. The parameter limits would consequently be $0.1 \leq k\Delta r \leq 1.3$ and $0 \leq \Delta r/r \leq 0.5$ for a maximum inaccuracy of ± 1.5 dB. If measurements are acquired in a duct, below the cutoff frequency and where consequently there is plane wave propagation, a more suitable limit for the first parameter would be $k\Delta r \leq 1.4$ for the same maximum inaccuracy of ± 1.5 dB. Recall that the finite difference error for plane wave propagation is a negative bias. However, the finite difference error can be a positive or negative bias, \pm bias, for more complex sound fields. The positive bias will occur at low frequencies as with the quadrupole source measurement where there are both low frequency and high frequency accuracy limits since the bias error can be extreme (well in

excess of 2 dB) at low frequencies. Monopole and dipole sources only have high frequency limits²⁴ so long as the parameters $k\Delta r$ and $\Delta r/r$ are minimized ($k\Delta r \leq 1.3$ and $\Delta r/r \leq 0.5$).

As an alternative guideline, Bruel and Kjaer¹³ recommend that "for accuracy to within 1 dB, the wavelength measured must be greater than six times the spacer distance".

3.2.2 Near-Field Errors

The two sensor cross spectral intensity measurement error associated with near-field effects depends on the parameter $\Delta r/r$ in much the same manner as the finite difference error depends on $k\Delta r$. Specifically, it will be shown that $\Delta r \ll r$ is generally desired to minimize errors associated with near-field effects.

Consider that the far-field directivity of a spatially extended source can be explained in terms of interference between the wavefronts from its various source regions. Then, in the farfield, the effect of differences in spherical spreading losses on the resultant sum is negligible compared to the delay, or phase differences, of the various paths. In the nearfield both terms are significant and the intensity may be quite different at the two sensor locations. In the nearfield, the relationship between pressure and particle velocity is an extremely complex function of position.

Thus, considering the pressure and particle velocity as a function of position, for a monopole source, the ratio of the measured to the true intensity is,

$$\frac{\hat{I}_r}{I_r} = \frac{1}{\left[1 - \frac{(\Delta r)^2}{4r^2}\right]} \frac{\sin k\Delta r}{k\Delta r} \quad (3.13)$$

It can be seen that the error approaches the result for a plane wave if measurements are sufficiently far from the source.

This analysis can be performed for all kinds of deterministic sources in which case it would be shown that the more complex the source, the greater the relative distance $r/\Delta r$ should be. Table 3.1 shows the relationship between r and Δr to maintain a near-field error of less than 1 dB for some standard deterministic sources.

Table 3.1 Minimum distance between source and receive sensors for near-field error less than 1 dB (from reference 21).

<u>Source Type</u>	<u>Distance, r, from source for error less than 1 dB</u>
Monopole	$r > 1.1 \Delta r$
Dipole	$r > 1.6 \Delta r$
Quadrupole	$r > 2.3 \Delta r$

3.2.3 Phase Errors

The amount of phase mismatch between the two channels in the intensity measurement system will affect the low frequency limit of the measurement. This is obvious since the lower the frequency the less the actual physical phase difference between the two pressure sensors and consequently the more influence any instrumentation phase mismatch will have on the measured acoustic phase difference. For a good microphone and analyzer combination a conservative estimate for this instrumentation phase mismatch error, denoted as $\Delta\alpha$, is roughly $\pm 0.3^\circ$. The intensity may be underestimated or overestimated according to the sign of the phase mismatch.

Rasmussen²⁵ states that the actual acoustic phase difference over the separation distance, Δr , should be a factor of ten greater than the instrumentation phase mismatch. Bruel and Kjaer¹³ state that to obtain accuracy within 1 dB, with a good probe and analyzer combination, "the phase change over the sensor distance should be more than five times the phase mismatch". Methods of measuring the phase mismatch are described in detail by Rasmussen.²⁵ However, as will be explained later, measuring this quantity is not necessary if phase calibration techniques are employed. Such calibrations will negate the majority of the instrumentation phase mismatch error.

Rasmussen²⁵ showed that the actual acoustic phase (in degrees), $\Delta\phi$

$= (\phi_1 - \phi_2)$, between the two pressure sensors can be expressed as

$$\Delta\phi = \frac{k\Delta r}{2\pi} = \frac{\Delta r f \rho_o I}{p_{rms}^2} \cdot 360^\circ \quad (3.14)$$

Where, $I = p_{rms}^2 / \rho_o c$ is the active intensity for an ideal plane progressive wave, p_{rms} is the rms value of acoustic pressure, and the other variables are as defined previously.

This representation is useful to point out some important relationships. It can be seen from equation (3.14) that the acoustic phase difference, $\Delta\phi$, is proportional to the frequency, and also dependent on the relation of the active intensity, I , to the mean-square pressure p_{rms}^2 . When the active intensity is low and the pressure is high, the phase difference becomes small, and consequently, measurements become more susceptible to any instrumentation phase mismatch.

The difference between pressure and active intensity depends both on the reactivity of the sound field and the orientation of the sensors. In a free field, where there is no reactivity, the active intensity level and pressure level will be highly correlated. In a totally reactive sound field the active intensity will be zero and the acoustic phase difference, $\Delta\phi$, will be zero. If, however, there is a phase mismatch error in the microphones or instrumentation, a residual intensity level will be measured. How to use this quantity to assess data quality will be

discussed in section 3.4.2.

The effect of instrumentation phase mismatch can be shown for plane waves where the ratio of the measured intensity to the true intensity would be

$$\frac{\hat{I}_r}{I_r} \approx \frac{\Delta\phi \pm \Delta\alpha}{\Delta\phi} \approx 1 \pm \frac{\Delta\alpha}{\Delta\phi} \quad (3.15)$$

and the measured error in dB is given by

$$L_{\epsilon_{\Delta\alpha}} \approx 10 \log \left(1 \pm \frac{\Delta\alpha}{\Delta\phi} \right) \quad (3.16)$$

3.3 Random Errors

Random errors represent mean-square fluctuations of the estimators around the expected value. Random errors arise mostly from finite sample lengths and may be large at low frequencies, or where the coherence between the two sensors is low, but they are usually not significant at high frequencies.

Using the definition of equation (3.4), the normalized random error for a random time dependent Gaussian, zero-mean, distributed quantity, say Φ , is given by

$$\epsilon_r[\hat{\Phi}] \approx \frac{1}{\sqrt{BT}} \quad (3.17)$$

where B is the frequency bandwidth of the signal, and T is the averaging time. This is valid when direct filtering is used in the processing to determine infinite duration time averaged quantities from finite duration averaging.

However, when FFT analysis is applied to stationary signals, the time averaged spectral quantities are estimated by computing an ensemble of estimates from n_d different subrecords, each of length T , and averaging these subrecords (ensemble averaging) to obtain a final "smooth" estimate. In this case the quantity BT in the previous equation is replaced by n_d and the random error for the spectral estimates can be minimized by increasing the number of ensembles in the averaging, i.e.,

$$\epsilon_r[G_{11}(f)] = \epsilon_r[G_{22}(f)] \approx \frac{1}{\sqrt{n_d}} \quad (3.18)$$

The quantities $G_{11}(f)$ and $G_{22}(f)$ are the one sided autospectral density functions. These frequency dependent spectral quantities are used in the estimation of the reactive intensity as described in equation 2.17. The frequency argument for these quantities will be omitted in most of this discussion to simplify notation.

The estimation of the active intensity is proportional to $\text{Im}[G_{12}(f)] = |G_{12}| \sin \phi_{12}$ as shown in equation 2.16. The normalized random error in

an estimate of the magnitude of the cross-spectral density function, $|G_{12}|$, is shown by Fahy¹⁴ and Seybert²³ to be,

$$\epsilon_r[|G_{12}|] = \frac{1}{\sqrt{\gamma_{12}^2 n_d}} \quad (3.19)$$

where γ_{12}^2 is the ordinary coherence function defined as

$$\gamma_{12}^2(f) = \frac{|G_{12}(f)|^2}{G_{11}(f)G_{22}(f)} \quad (3.20)$$

Equations for the normalized random error of active and reactive intensity have been derived²⁶ and verified¹⁴ to be

$$\epsilon_r[\hat{I}_r] = \frac{1}{\sqrt{2n_d}} \sqrt{(1 + \gamma_{12}^{-2}) + (\gamma_{12}^{-2} - 1)\cot^2 \phi_{21}} \quad (3.21)$$

for the active intensity and

$$\epsilon_r[\hat{J}] = \frac{1}{\sqrt{n_d}} \sqrt{1 + \frac{(2G_{11}G_{22})(1 - \gamma_{12}^2)}{(G_{22} - G_{11})^2}} \quad (3.22)$$

for the reactive intensity. The phase term, ϕ_{21} in equation (3.21) is the acoustic field phase difference between the two measurement points.

Equations (3.21) and (3.22) are valid for $\phi_{21} \neq 0$.

The measurement of the phase is also subject to a random error. However, a normalized random error for the phase is normally not used

since the true phase could be zero and division by zero is meaningless. Therefore, the random error for the phase is expressed as the standard deviation of the phase estimate which is defined²¹ in units of radians as

$$\sigma[\hat{\phi}_{12}] = \sqrt{\frac{(1 - \gamma_{12}^2)}{2\gamma_{12}^2 n_d}} \quad (3.23)$$

This result for the cross-spectrum phase angle estimate, varies with frequency as do the other quantities.

The reader should also be reminded that these equations for random error assume sound fields with random time dependence and normal amplitude probability distribution.

3.4 Quantifying and Minimizing Errors

3.4.1 Calibration

A key advantage of the two pressure microphone technique is the ease with which accurate calibration can be carried out. When calibrating for sound intensity measurements both amplitude and phase calibration need to be considered. For microphones, the amplitude calibration is commonly performed with a pistonphone, which provides a 124 dB re 20 μ Pa sound pressure level at 250 Hz. This will yield accurate amplitude calibration unless the microphones do not have a flat frequency response over the measurement range of interest. In

those cases other relatively simple and accurate calibration techniques are available. The microphones used for this research and the majority of transducers used for sound intensity measurements are high quality and have flat responses over a wide frequency range.

Phase accuracy is of primary importance in sound intensity measurements and consequently phase calibration considerations are critical. Adequate phase calibration will almost eliminate the phase mismatch error described in section 3.2.3. In addition, phase matched microphones and precision instrumentation can be utilized. In many cases this alone will be adequate for the intensity measurements required and thus phase mismatch errors will be small without a phase calibration. With simple phase calibration techniques available as summarized below more affordable sensors may be employed with little or no loss in data accuracy. These calibration techniques can still be employed in conjunction with phase matched microphones to eliminate instrumentation phase errors and further improve data accuracy at low frequencies and small sensor separations.

One method of phase calibration which is described in detail in reference [25] and used frequently with Bruel & Kjaer intensity systems is accomplished by placing the intensity probe in a small coupler which provides a completely reactive field. From the intensity and pressure measured in the coupler, the phase error in the system can be

calculated and accounted for.

Another common phase calibration method is the transfer function method. The intent is to measure the instrumentation phase shift at each frequency and then correct for the error numerically. The microphone calibration is accomplished by mounting both microphones on a rigid disk at the end of a duct so they will be exposed to the same sound field. The transfer function between the two channels is then measured²⁷ and used to correct measurements. Calculations for this method are easy but it is difficult to determine the transfer function over a wide frequency range due to duct resonances. Duct diameters must be set to assure plane wave propagation at the highest frequency of interest.

The method which was used for the measurements performed in this research is the microphone switching technique. With this method the microphones are placed in a fixed sound field. Intensity measurements are acquired with the sensors in a fixed arrangement and then the microphone locations are interchanged without disconnecting the cables or changing inputs to the instrumentation. An average is then taken between the intensity measured with the first arrangement and the switched arrangement. The average used for complex numbers is the geometric mean which corresponds to the positive root of the product of the two numbers. Subsequently, an elimination of the

instrumentation phase error occurs which results because the phase has an opposite sign for each orientation and thus will cancel.

The switching technique requires more intensive arithmetic since the square root of a complex data block must be computed. With modern computers this is generally not a limitation. The switching technique is often not subjected to the frequency limitations of the transfer function method.

Gade²⁶ reports the bias error formula for phase error between the two channels, after implementation of the microphone switching technique, to be

$$\frac{\hat{I}_r}{I_r} = \frac{\sin k\Delta r}{k\Delta r} \cos \Delta\alpha \quad (3.24)$$

where $\Delta\alpha$ is the instrumentation phase mismatch as previously defined. This phase mismatch error is less than 1 dB for $\Delta\alpha = 8^\circ$, and $k\Delta r \leq 1.12$. For the instrumentation used in this research the phase mismatch, $\Delta\alpha$, was measured to be in the range of $0.15^\circ \leq \Delta\alpha \leq 7.4^\circ$ from 20 Hz to 5000 Hz.

3.4.2 Pressure Intensity Indices

The pressure intensity index, δ_{pi} , (also called reactivity index) describes the phase change over the separation distance, Δr , and is a primary indicator of the accuracy of an intensity measurement. It is a

function of the type of sound field and the orientation of the microphones. By definition it is merely the difference between the pressure level, L_p , and the intensity level, L_I , as measured in the experimental sound field,¹⁴

$$\delta_{pl} = L_p - L_I = 10 \log \left[\frac{k\Delta r}{(\phi_{12} \pm \Delta \alpha)} \right] \quad (3.25)$$

It should be noted that δ_{pl} is sometimes defined as $L_I - L_p$. This is perfectly valid as long as the convention is maintained.

The residual pressure intensity index, δ_{pIR} , (also called residual intensity index) is defined as the pressure level minus the intensity level but for the special case when the microphones are placed in a controlled sound field of uniform pressure, in which $\phi_{12} = 0$, thus $I = 0$, and the ratio $k\Delta r / (\phi_{12} \pm \Delta \alpha)$ becomes equal to $\pm k\Delta r / \Delta \alpha$. This provides an indication of the error in intensity due to phase mismatch. The residual pressure intensity index is thus written as

$$\delta_{pIR} = L_p - L_{IR} = 10 \log \left[\frac{k\Delta r}{\Delta \alpha} \right] \quad (3.26)$$

Since the sound field is controlled for this index, and $\phi_{12} = 0$, the intensity should be zero. However, a residual intensity, I_{re} , will be measured due to the instrumentation phase mismatch, $\Delta \alpha$. The effect of this phase mismatch may be effectively eliminated by taking half the difference between the signed intensities measured with the microphones

in a given position and again after switching them by a precise 180° .

For an error in the estimate of intensity of less than ± 1 dB, the phase change along the microphone separation distance must be 5 times the instrument phase mismatch. This corresponds to $\delta_{pIR} - \delta_{pl} > 7$ dB. It is noted that δ_{pl} can approach δ_{pIR} as the sound field becomes more and more reactive, i.e., $\phi_{12} \rightarrow 0$ in a totally reactive field.

It should also be noted that this technique of utilizing the pressure intensity indexes to evaluate dynamic measurement capability and error can be employed in sound power measurements. Jacobsen and Ren²⁸ developed a compensation technique whereby the residual pressure intensity from the equipment is applied to the completed sound power estimate to correct for lack of instrumentation performance due to the phase mismatch.

CHAPTER 4

INTENSITY MEASUREMENT CONSIDERATIONS IN THE PRESENCE OF
FLOW

4.1 Background and Theory

The work of Munro and Ingard²⁹ provides a mathematical description of acoustic intensity measurements in the presence of flow, and identifies two fundamental problems that must be considered. The first relates to the definition of acoustic intensity in a field where there is mean flow. The second problem lies in the uncertainty of what exactly the microphone placed in the moving flow field measures.

To address the first problem, recall that in the absence of a mean flow a pressure gradient can arise only because of a time rate of change of the acoustic velocity as shown in equation (2.9). Thus, the two sensor technique utilizes the assumption that all the particle acceleration is due to the acoustic wave. However, in the presence of mean flow, a pressure gradient can also arise from changes in the particle velocity with respect to position. Consequently, the linearized Eulers equation for the case of uniform steady background flow would be

$$\rho_o \left(\frac{\partial \vec{u}}{\partial t} + \vec{u}_o \cdot \nabla \vec{u} \right) + \nabla p = 0 \quad (4.1)$$

where ρ_o , and u_o , are assumed to be constant in both time and space

and the second term is the new term considered. Munro and Ingard point out for the case of plane waves, that when using the cross spectral two microphone method, an error proportional to the first power of the Mach number ($M = u_o/c$) of the flow can be expected from this convection effect. As confirmed by Oswald and Donovan⁴ this error would be too small to measure under most experimental situations when the Mach number is less than 0.1.

Comparin⁷ developed a new formulation that extends the method to the case of spherically spreading waves in uniform one-dimensional flow but requires that a specific source model be known or assumed.

The second problem is the question of what exactly is measured by a pressure sensor (microphone or hydrophone) located in turbulent flow. This problem was not studied by Munro and Ingard²⁹ but has been investigated by others.^{4,5,6} This problem is often the most significant cause of error since the mean convection effect is essentially negligible for $M \leq 0.1$ as mentioned above. In essence the problem then, is the ability to (or lack of ability to) discriminate against noise associated with the unsteady turbulent flow present at the individual pressure sensors. This turbulence noise would be a factor for sensors situated in the free stream or flush mounted. Experimental measurement results from sensors situated in the free stream, presented by Oswald and Donovan,⁴ and by Fahy,⁹ demonstrate that reliable intensity measurements can be

obtained in flow fields with $M < 0.1$ if precautions are taken such as using nose cones and wind screens.

Lauchle⁵ presented a technique for determining the bias in intensity measurements in a field with turbulent boundary layer flow using flush mounted sensors. He concluded that the bias error would be small when the sensor separation distance is large compared to the correlation lengths of the turbulent pressure fluctuations; however, no experimental results were provided. Chapters 5 and 6 will provide some experimental results for this theoretical finding. Section 4.2 provides an overview of this technique along with a physical description of the phenomena which must be considered when using flush mounted sensors to acquire intensity measurements in a field with flow.

A final consideration is that, in principle, the two sensor intensity measurement technique has a certain degree of built in capacity to negate the random effects of turbulence as a consequence of the time averaging of the input signals. However, as reported by Fahy,¹⁴ this beneficial effect is small, but does increase with sensor separation.

4.2 Measurements with Flush Mounted Sensors

This section summarizes the theoretical basis of the technique presented by Lauchle.⁵ Information specific to the application of the technique is presented in Chapters 5 and 6 along with experimental

results from utilization of the technique.

The planar flow model schematic of figure 4.1 illustrates some physical phenomena to consider when acquiring acoustic intensity measurements with flush mounted sensors in the presence of a mean flow velocity, u_o .

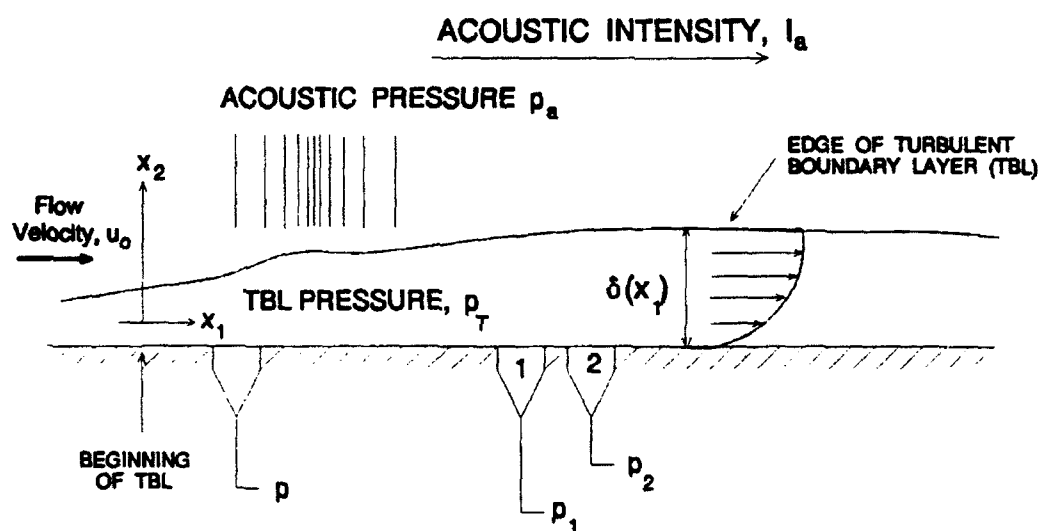


Figure 4.1 Illustration of boundary layer flow over a flat surface that contains flush mounted acoustical pressure measurement sensors. I_a represents the acoustic intensity from the acoustic source of interest in the direction parallel to the surface.

Assuming viscous flow, a boundary layer develops over the surface. The thickness of the boundary layer, δ , is a function of the streamwise coordinate, x_1 , and is defined by the value of x_2 where the velocity, $u = 0.99u_o$. The boundary layer is laminar near the leading edge of the surface and has no fluctuations in pressure or velocity. However, after some distance the boundary layer transitions into a turbulent boundary layer (TBL) where pressure and velocity fluctuations are prominent. The transition location can be defined from the Reynolds number, $Re = u_o x_1 / \nu$, where ν is the kinematic viscosity. This transition normally occurs in the range of $10^5 \leq Re \leq 10^6$ for a smooth flat plate. The transition range is sensitive to surface finish and will be lower for rougher surfaces.

Assume the purpose of the test is to measure the acoustic intensity, I_a , from an independent source outside the turbulent boundary layer. The measurement sensors are mounted flush to the surface and consequently are exposed to the turbulent boundary layer. The acoustic pressure originating from the source of interest is denoted as p_a , and the turbulence pressure is denoted as p_T . The total pressure at the face of the sensor will contain contributions from both p_a and p_T , and is shown as,

$$p = p_a + p_T \quad (4.2)$$

Utilizing the intensity definition of equation (2.16) and the bias error definition of equation (3.1), Lauchle⁵ derived an expression for the bias error in the intensity spectrum calculated from measurements made with the pair of sensor. This expression is:

$$b[\hat{I}_a(\omega)] = \frac{-Im\hat{G}_{12}}{\omega\rho_o\Delta r} + \frac{ImG_{12}}{\omega\rho_o\Delta r}, \quad (4.3)$$

where \hat{G}_{12} is defined as the cross spectrum measured between the two sensors in the presence of flow, and G_{12} is the cross spectrum measured in the absence of flow. Thus, the carrot, ^, is used here to denote measurements, or estimates, acquired in the presence of both a mean flow and an acoustic field. The absence of the carrot here does not imply that the quantity is not measured, or estimated, but rather implies the measurement was acquired with only one of the variables (flow or acoustic source) in effect. Thus the absence of the carrot means the measurement was acquired either with flow and no independent acoustic source, or with an acoustic source in the absence of flow.

The total pressure at sensors 1 and 2 would be expressed as

$$\hat{p}_1 = p_{a_1} + p_{T_1}, \quad (4.4)$$

and

$$\hat{p}_2 = p_{a_2} + p_{T_2} . \quad (4.5)$$

The corresponding one-sided cross-spectral density function as presented by Lauchle⁵ is,

$$\hat{G}_{12} = G_{12} + G_{T_1 T_2} + G_{a_1 T_2} + G_{T_1 a_2} . \quad (4.6)$$

Because of the statistical independence between p_a and p_T , equation (4.6) reduces to:

$$\hat{G}_{12} = G_{12} + G_{T_1 T_2} . \quad (4.7)$$

From this, Lauchle⁵ concluded that if the separation distance between the sensors, Δr , is greater than the streamwise correlation length, Λ , of the turbulent pressure fluctuations, then the turbulence cross spectrum, $G_{T_1 T_2}$, is approximately zero. Review of equation (4.3) shows that with these conditions, the intensity estimate would be unbiased.

CHAPTER 5

MEASUREMENT TECHNIQUE AND EXPERIMENTAL FACILITY

5.1 Introduction

The objective of the experimental research was to determine the bias error in intensity measurements caused by turbulent boundary layer pressure fluctuations when the measurements are acquired in low Mach number flow ($M < 0.1$) with flush-mounted pressure transducers of a given size and shape. The sound field thus contains energy contributions from the flow as well as the acoustic energy from a source which we desire to measure. Consequently, the subsonic non-propagating turbulent boundary layer pressure fluctuations are considered to be unwanted noise at the face of the transducer. The technique employed is based on an analysis by Lauchle⁵ in which he predicted the bias error for intensity estimates in the presence of low Mach number flow.

The purpose of this pursuit stems from the considerable interest over the past 15 years in acquiring intensity measurements in the presence of flow. Formulations currently used are generally limited to zero flow, or plane waves, and most methods devised for measurements in flow require cumbersome sensor apparatus such as the combination Z probe with turbulence tube apparatus used by Fahy,^{6,14} and the probe

used by Oswald and Donovan,⁴ which utilized pointed nose cones and clay fairings. In the evaluation of Lauchle's technique, the test conditions included mean flow and acoustic waves above the plane wave cutoff frequency of the wind tunnel test section, in order to assess if the technique would be useful in many in-situ applications where the sound field contains higher order modes, and flow.

The technique is non intrusive to the acoustic field, is easy to setup, and is not susceptible to scattering type errors from sensors and holding fixtures. These desirable attributes were another reason for investigating the technique.

During the experimentation, measurements were obtained with the standard two microphone intensity technique for the case of an acoustic source in the presence of mean flow, with the acoustic source in the absence of mean flow, and again with the acoustic source off and mean flow retained. The specific measurements either acquired or calculated include the active and reactive intensities, auto and cross spectral densities, coherence, phase, equivalent far field pressure, residual pressure intensity index, and bias errors. This was performed along one coordinate axis with the understanding that the technique could easily be extended to two or three dimensions and provide a more complete picture of the sound field if proven to be accurate.

5.2 Facility

The measurements were acquired in a subsonic wind tunnel located in the Applied Research Laboratory, Garfield Thomas Water Tunnel Building, of the Pennsylvania State University. The wind tunnel is a closed circuit system with a 150 HP motor driving a variable speed, axial-flow, blower which can provide test section flow up to 45.72 m/s. It has a test section 1.219m wide x 4.88m long, and a large settling section with fine mesh screen located upstream of the test section as depicted in figure 5.1. The settling section reduces the background turbulence level to a value of less than 0.2%.

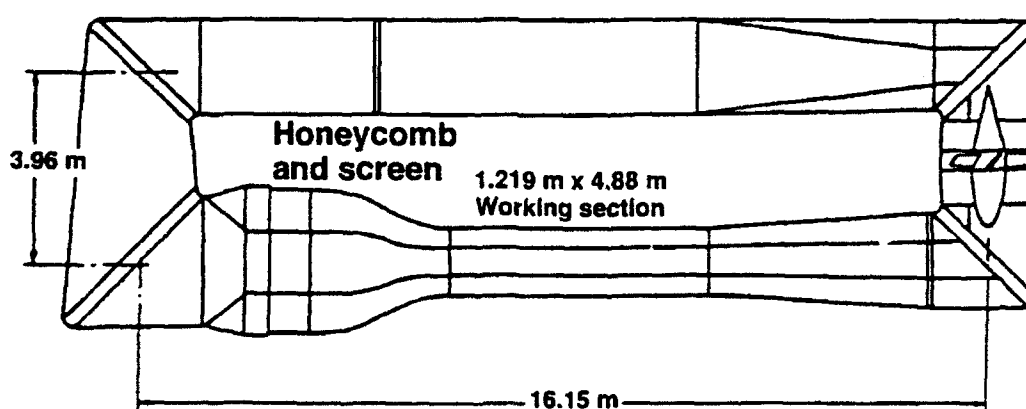


Figure 5.1 The Pennsylvania State University, Applied Research Laboratory, subsonic wind tunnel [Provided by ARL]

5.3 Measurement Considerations

Measurements were acquired with flow speeds of 6, 9, 18, and 30.5 m/s, at sensor separation distances of 13.5, 25.4, and 50.8 mm. Most data were acquired over the frequency range from 0 - 2500 Hz, but several tests were also conducted over the range of 0 - 5000 Hz. The one-half inch (12.7 mm) diameter B & K microphones were flush mounted in a 16 mm thick flat plexiglass window located in the farthest downstream window frame of the test section (see figure 5.2). This placed the microphones 4.3 meters from the leading edge of the test section. At this location the boundary layer was clearly turbulent, for all flow speeds used, based on boundary layer measurement presented by Josserand and Lauchle.³⁰ These measurements for the streamwise location of the on-set of transition, and the on-set of the turbulent boundary layer in the wind tunnel, are relative to a virtual origin of the laminar boundary layer which is approximately 1.05 meters upstream of the leading edge of the tunnel test section. With these measurements, the on-set of the turbulent boundary layer would be some 4 to 6 meters upstream of the measurement location, depending on flow velocity.

If the distance between the sensors and the leading edge of the tunnel test section is used as the characteristic length, x_1 , in the Reynolds number calculation (recall from section 4.2 that $Re = u_\infty x_1 / \nu$), the Reynolds numbers range from 2.6×10^6 to 8×10^6 , for the speeds

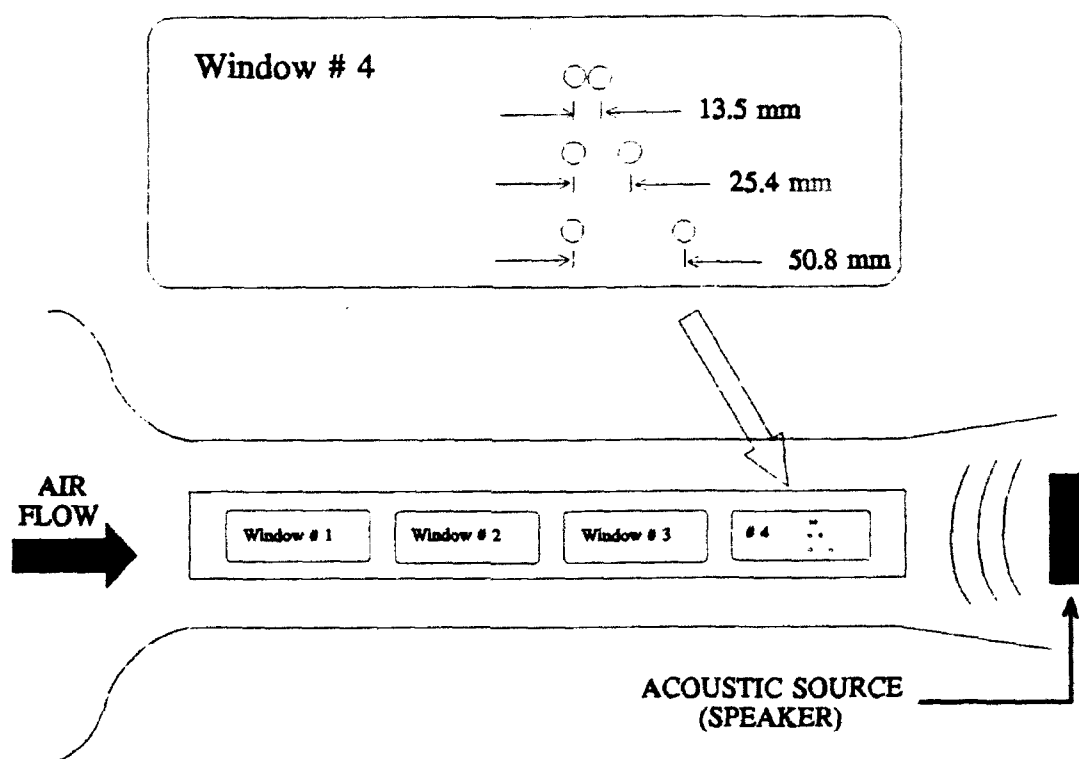


Figure 5.2 Microphone orientation in the wind tunnel test section

tested. If the distance between the virtual origin of the boundary layer and the sensors is used as the characteristic length, the corresponding Reynolds numbers range from 3.3×10^6 to 1.1×10^7 . These Reynolds numbers also imply that the boundary layer was turbulent at the sensor location since even for a *smooth* flat plate the boundary layer typically transitions to a turbulent boundary layer in the range $10^5 \leq Re \leq 10^6$.

The experiments for this research took many days due to the length of time to acquire the large number of ensembles desired to achieve reliable low frequency phase information. Equation (3.23) shows that the random error of the phase is dependent on the coherence and the number of ensembles. The coherence could not be controlled or varied for each test condition so the number of ensembles acquired were kept high. Typically, 2048 ensembles were used, although as few as 1024 and as many as 4096 were used in some instances.

5.4 Instrumentation

The instrumentation used is shown schematically in figure 5.3. It shows a pair of B&K model 4181 phase matched microphones, associated adapters, power supply, and Ithaco amplifiers, all making up the front end of the instrumentation suite. The acquisition and computation was performed with a Zonic System 7000 parallel signal processor equipped with Zeta software, connected to a DEC Micro-VAX

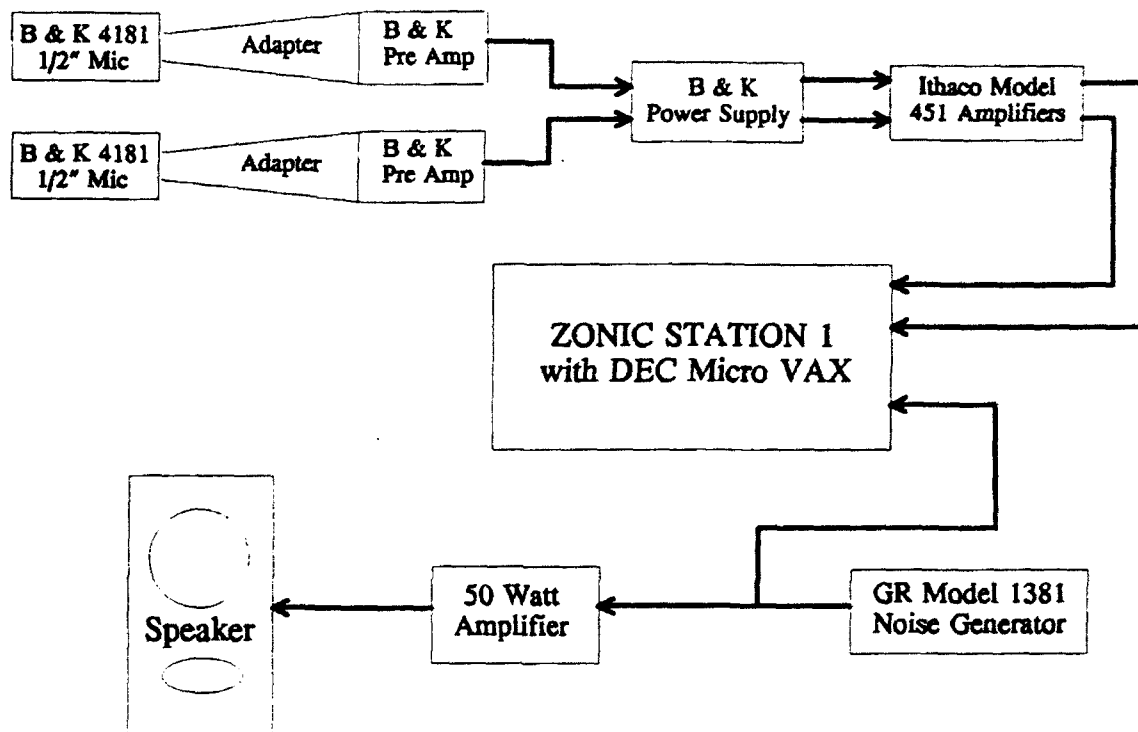


Figure 5.3 Experiment Instrumentation Set-up

computer. The sound source was an Altec 604E speaker with a 13 inch woofer and a horn, fed with random noise from a GR 1381 random noise generator.

Overall the instrumentation was satisfactory. The Zonic system provided true parallel processing, real time display, and powerful computational capability. With the Zeta software there was considerable flexibility to perform nearly any measurement or calculation if the proper programming was performed. This flexibility was, however, at the expense of user friendliness, since any measurement or calculation requires use of Zeta commands, block arithmetic, and/or programming. Consequently, familiarity with the Zeta software language and VAX VMS is required for even the most trivial measurement or operation. A major instrumentation shortcoming was in reliability. The system would repeatedly crash or lock up during calibration, acquisition, and processing operations, due to its interconnection with a VAX mainframe computer system. Various solutions were being investigated.

5.5 Calibration and Finite Difference Approximation Error

Amplitude and phase calibrations were performed each day measurements were acquired. For the amplitude calibration both channels were calibrated separately using a Bruel and Kjaer type 4228 Pistonphone which subjected each microphone to a steady 124 dB re 20

μ Pa sound pressure level at 250 Hz. This tone calibration was adequate for the microphones used since they had a flat frequency response over the frequency range measured.

Phase calibration was performed by placing the microphones in a plane wave calibration tube and using the switching technique discussed in chapter 3. Two separate plane wave calibration tubes were required for the complete frequency range of interest. One tube covered the frequency range from 70 - 950 Hz and the other tube went from 800 to 5270 Hz. In the overlapping frequency region, where the spectra were below the plane wave cutoff frequency in both tubes, the phase calibrations from the two tubes were nearly identical as would be expected. Therefore, a cut-and-paste operation was performed with the two phase calibration files to obtain one phase calibration for the entire frequency range.

The finite difference approximation error in the intensity estimate is shown in Figure 5.4 for the sensor separations used in these experiments. Most of the data for these experiments were acquired over the frequency range of 0 to 2500 Hz but some data were acquired up to 5000 Hz, which is the range of the calculations of Figure 5.4.

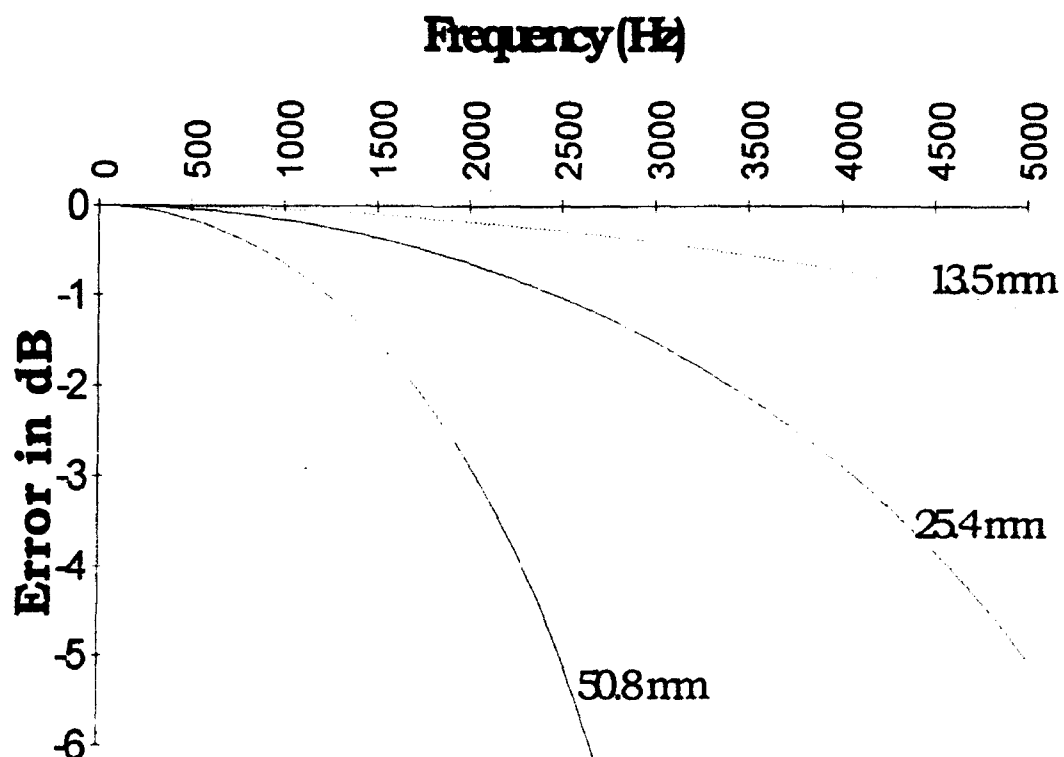


Figure 5.4 Error in intensity level resulting from the finite difference approximation for the case of a plane wave, for three sensor separations.

CHAPTER 6

EXPERIMENTAL RESULTS

6.1 An Introduction to the Technique

The experiments performed were designed to validate a theory developed by Lauchle⁵ for calculating the bias error of intensity estimates acquired in the presence of low Mach number turbulent boundary layer flow. This bias error formula was shown in equation (4.3) and is repeated here as equation (6.1),

$$b[\hat{I}_r(\omega)] = \frac{-Im\hat{G}_{12}}{\omega\rho_0\Delta r} + \frac{ImG_{12}}{\omega\rho_0\Delta r} . \quad (6.1)$$

This can be rewritten as,

$$b[\hat{I}_r(\omega)] = \hat{I}_r(\omega) - I_r(\omega) . \quad (6.2)$$

Here, $\hat{I}_r(\omega)$ is the measured intensity spectrum with low Mach number mean flow and $I_r(\omega)$ is the measured intensity spectrum in the absence of the mean flow. In both cases there exists an acoustic field (sound from a speaker in these experiments) which is statistically independent of the pressure field generated by the turbulent boundary layer. As discussed in chapter 5, the ability to quantify accurately such an acoustic field, in the presence of the low Mach number mean flow, is the underlying intent of this technique.

Lauchle⁵ predicted the bias error would reduce to the non-dimensionalized form shown in figure 6.1, where $k_c \Delta r$ is the independent variable. The term k_c is ω/u_c and is called the convection wavenumber, since $u_c = 0.7u_0$ represents the speed at which the pressure producing turbulence is "convected". The term, G_{TT} , in the ordinate, is the auto-spectrum of the turbulent boundary layer pressure field as measured by either of the flush mounted sensors.

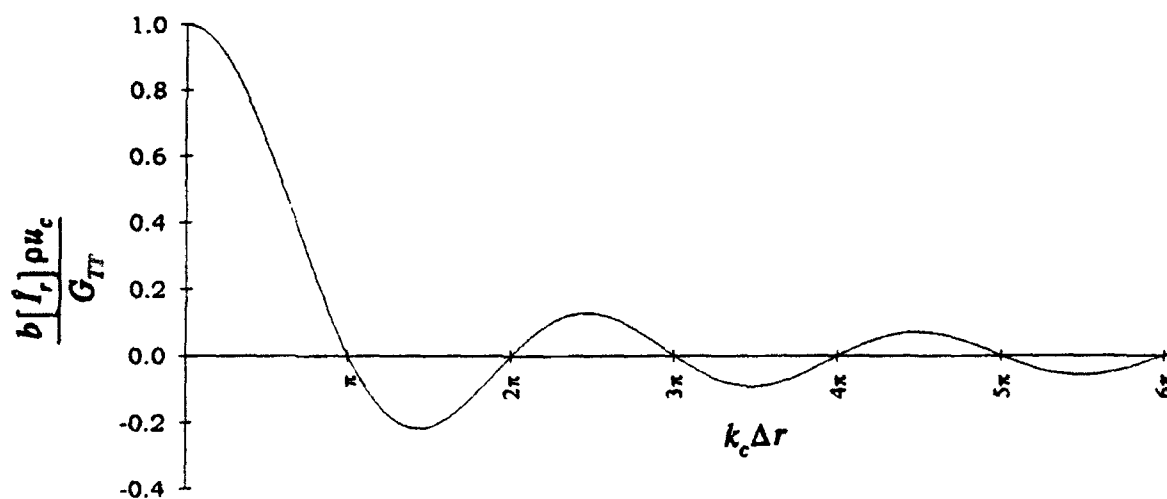


Figure 6.1 Non-dimensionalized bias error for intensity estimate (from Lauchle⁵)

Figure 6.1 shows the rapid decrease of the bias error as $k_c \Delta r$ increases. Figure 6.1 could easily be plotted using an alternate

abscissa, $\Delta r/\Lambda$, that is proportional to $k_c \Delta r$. It is then apparent that the intensity estimate becomes less sensitive to the turbulent pressure fluctuations as the separation distance between the two sensors increases relative to the turbulence correlation length, Λ . Based on the Corcos model for turbulent pressure spectra, Lauchle⁵ showed this correlation length to be approximated as,

$$\Lambda = \frac{11\pi}{4k_c} = \frac{11u_c}{8f} . \quad (6.3)$$

Equation (6.3) shows that the turbulence correlation length, Λ , is inversely proportional to the frequency and directly proportional to the velocity. For the case of a 30.5 m/s mean flow velocity, figure 6.2 illustrates the relationship between the correlation length, Λ , and frequency, for $\Delta r = 13.5\text{mm}$, $\Delta r = 25.4\text{mm}$, and $\Delta r = 50.8\text{mm}$. Figure 6.2 also shows how the quantity $k_c \Delta r$ relates to the frequency for these sensor separation distances.

Equation (6.2) is in the standard form for the bias error as defined in equation (3.1) and can be rearranged to yield

$$\frac{\hat{I}_r(\omega)}{I_r(\omega)} = 1 + \frac{b[\hat{I}_r(\omega)]}{I_r(\omega)} , \quad (6.4)$$

or equivalently,

$$U_o = 30.5 \text{ m/s}$$

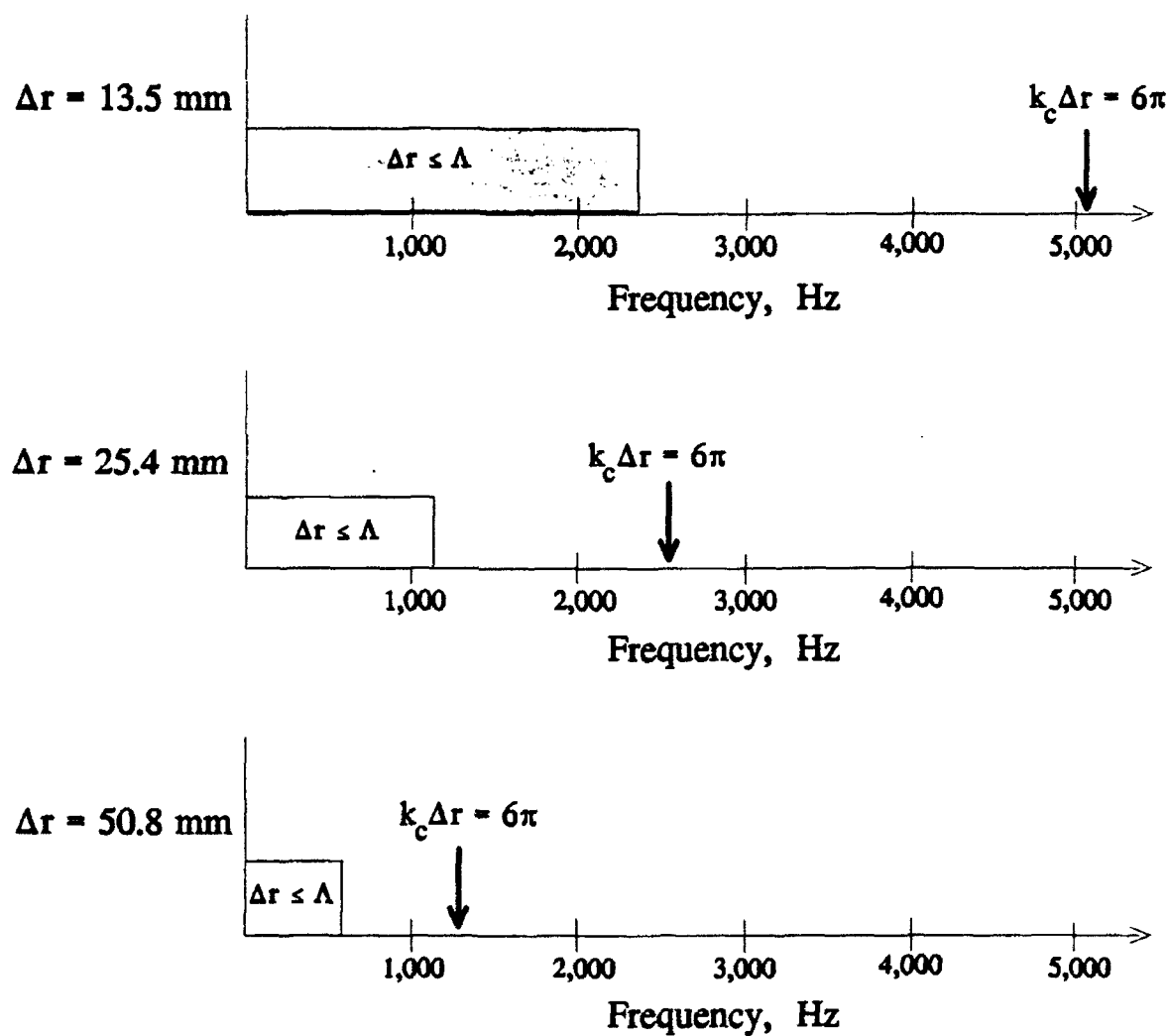


Figure 6.2 Relationship between turbulence correlation length, Λ , sensor separation, Δr , frequency, and the non-dimensional quantity $k_c \Delta r$

$$L_{\hat{I}_r} - L_{I_r} = 10 \log \left(1 + \frac{b[\hat{I}_r]}{I_r} \right), \quad (6.5)$$

where the frequency dependence is suppressed. Substituting in the normalized bias error term as defined in equation (3.3), yields the following bias error expression,

$$L_{\hat{I}_r} - L_{I_r} = 10 \log(1 + \epsilon_b) = \Delta L_I. \quad (6.6)$$

This bias error is plotted in Appendix A. The normalized bias term, ϵ_b , in equation (6.6) is not what is plotted in figure 6.1. Figure 6.1 is the non-dimensionalized bias error, while the normalized bias error, ϵ_b , is related to the ordinate of figure 6.1 by:⁵

$$\epsilon_b = \left(\frac{b[I_r] \rho u_c}{G_{TT}} \right) \cdot \left(\frac{G_{TT}}{\hat{I}_r |G_{12}| M_c} \right), \quad (6.7)$$

where, $M_c = u_c/c$, is the convective Mach number. Representative G_{TT} and G_{12} spectra are shown in figures 6.3 and 6.4 respectively.

Equation (6.6) can be rearranged to yield,

$$L_{I_r} = L_{\hat{I}_r} - 10 \log(1 + \epsilon_b) = L_{\hat{I}_r} - \Delta L_I. \quad (6.8)$$

Equation (6.8) states that the true intensity level (the intensity level due solely to the acoustic field of the statistically independent external source) is equal to the intensity level measured in the presence of the

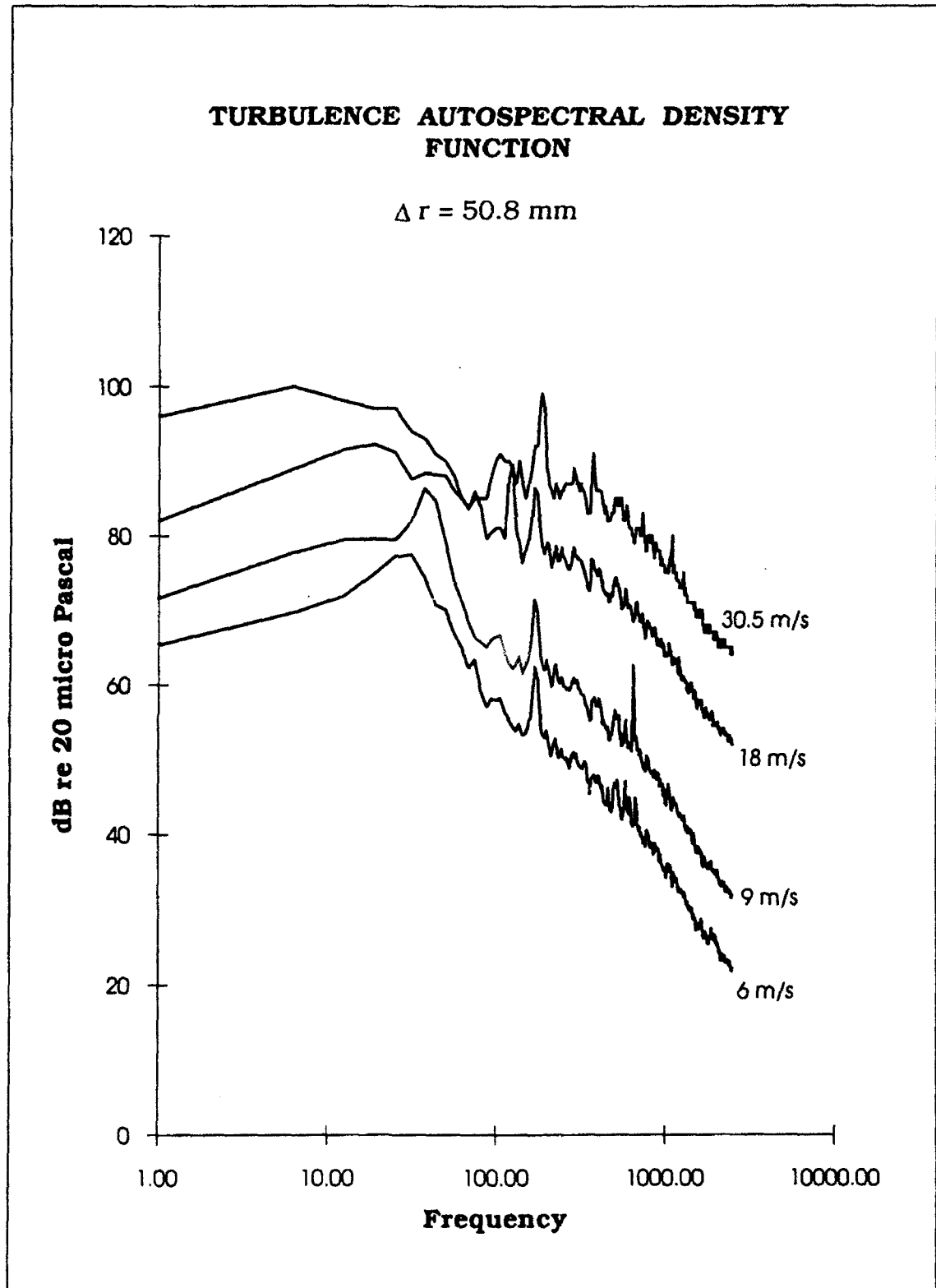


Figure 6.3 Autospectral density functions for turbulent pressure

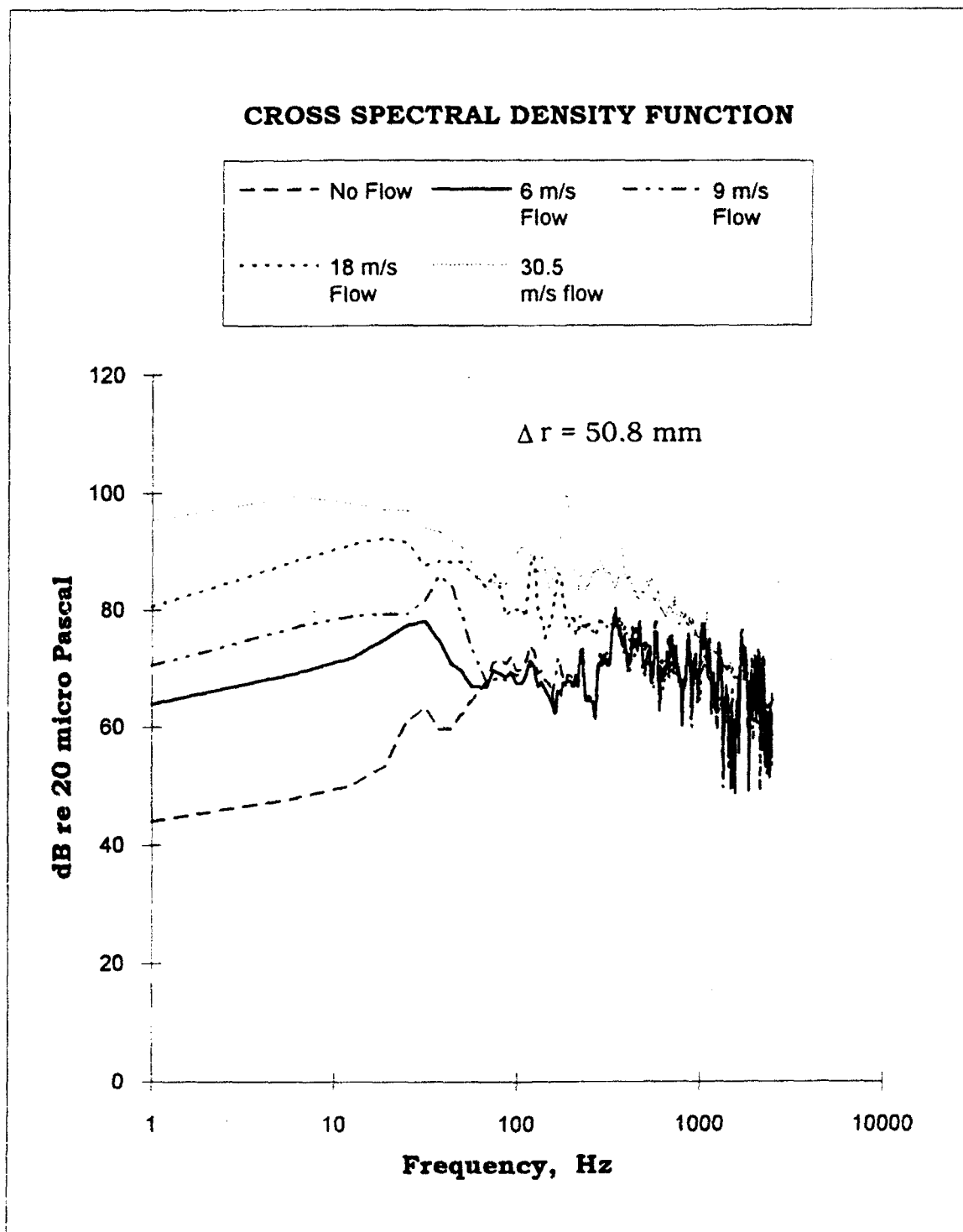


Figure 6.4 Cross-spectral density function comparisons

mean flow (which contains contributions from the non propagating turbulent boundary layer pressure field), minus a bias error. Thus, if the bias error of equation (6.6) can be calculated, then the true acoustic intensity level can be derived.

6.2 The Bias Error

Appendix A contains plots of the experimentally determined bias errors, defined by equation (6.6), for various velocities of mean flow and various sensor separation distances. Table 6.1 shows the specific velocity and separation parameters represented in the bias error plots of Appendix A.

The coherence function measured between the two pressure sensors in the presence of the mean flow is overlaid with the bias error curves of Appendix A. This coherence curve is useful in assessing the validity of the bias error value at the corresponding value of $k_c \Delta r$, as well as providing the necessary input for computing a random error as in equation (3.21).

6.3 The Intensity Spectrum

The individual intensity spectra used to calculate the bias errors of equation (6.6) are shown in Appendix B. The intensity spectra of equation (6.6) are overlaid in a plot at the top of each page in Appendix

B. The plot on the bottom of each page in Appendix B is an overlay of the intensity spectra for the case where the source is ON and there is a mean flow, vs the case where the source is OFF and the mean flow is retained. This condition (with the source OFF and with mean flow) was incorporated into the experimental program to provide further information for validating the data integrity, and also to provide the data necessary to non-dimensionalize the bias error.

Table 6.1 Parameters associated with the figures of Appendix A and B

Flow Velocity	Sensor separation parameters		
u_o (m/s)	$\Delta r = 13.5$ mm	$\Delta r = 25.4$ mm	$\Delta r = 50.8$ mm
6		Fig. A-1, B-1	Fig. A-2, B-2
9	Fig. A-3, B-3	Fig. A-4, B-4	Fig. A-5, B-5
18	Fig. A-6, B-6		Fig. A-7, B-7
30.5	Fig. A-8, A-9, B-8, B-9		Fig. A-10, B-10

The specific velocity and separation parameters represented in Appendix B are the same as in Appendix A and are summarized in table

6.1.

The direction of energy propagation is also depicted on the plots of Appendix B. The speaker was specifically oriented so the direction of acoustic energy propagation was opposite to the direction of mean flow. This provides another tool to help distinguish the acoustic source from the non propagating turbulent boundary layer interference. Energy propagating away from the source would travel upstream and will appear above the abscissa in the plots of Appendix B. Energy traveling in the downstream direction, such as turbulence energy when $\Delta r < \Lambda$, will appear below the abscissa in the plots of Appendix B.

6.4 The Non-Dimensionalized Bias Error

The non-dimensionalization introduced by Lauchle⁵ should yield results similar to those shown in figure 6.1. The non-dimensionalized bias error results calculated with data from these experiments were inconsistent. In an effort to improve consistency, the calculations were performed only at frequencies where the coherence function was greater than 0.95, 0.9, and 0.8, respectively. At higher values of coherence, γ^2 , the estimates will be more accurate since the phase estimate is highly dependent on the coherence as shown in equation (3.23). There were insufficient data points above $\gamma^2 = 0.95$ and $\gamma^2 = 0.9$ to draw any clear conclusions. At $\gamma^2 = 0.8$, there were sufficient data points, but the

results were still inconsistent and inconclusive.

The non-dimensionalization requires utilization of the turbulent boundary layer pressure spectrum as measured by one of the intensity probe pressure sensors. These spectra were not "smoothed" which contributed to the inconsistent results. Fluctuation in G_{π} of only 2 or 3 dB will cause extreme fluctuation in the linear non-dimensionalization indicated on the ordinate of Figure 6.1. In essence, the non-dimensional form of the bias utilizes the ratio of measured intensity spectra to measured pressure spectra. Because these spectra are estimates in themselves, it seems inappropriate to non-dimensionalize the biases measured since an additional error is introduced when dividing one measured spectrum by another. What is important, however, is that the bias plots shown in Appendix A exhibit trends very similar to those predicted by Lauchle⁵ and shown in Figure 6.1.

6.5 Pressure Intensity Indices

Overlays of representative pressure intensity index vs residual pressure intensity index curves are shown in the top plot of each figure in Appendix C. These overlays provide further validation of the intensity spectrum accuracy by showing that $\delta_{piR} - \delta_{pi} \gg 7$ dB, (the lower plot on each figure is the difference curve of $\delta_{piR} - \delta_{pi}$). The amplitude value of $\delta_{piR} - \delta_{pi}$ is generally negative since the Zonic software used the

convention of $\delta_{pl} = L_l - L_p$ instead of $\delta_{pl} = L_p - L_l$. See section 3.4.2 for further explanation. Table 6.2 shows specifically what data are included in Appendix C.

Table 6.2 Pressure Intensity Indices conditions presented in Appendix C

Mean Flow Velocity (u_o)	Sensor separation distance (Δr) mm		
	$\Delta r = 13.5$	$\Delta r = 25.4$	$\Delta r = 50.8$
No Flow	Fig. C-1	Fig. C-3	Fig. C-5
9 m/s	Fig. C-2	Fig. C-4	Fig. C-6
30.5 m/s			Fig. C-7

CHAPTER 7

CONCLUSIONS

7.1 Overview of the Results

The overall quality of the measured intensity data is very good. The pressure intensity indices presented in Appendix C prove that the phase mismatch was insignificant and that the associated error in the estimate of intensity was consequently much less than ± 1 dB. These pressure intensity indices also indicate that the acoustic field was not significantly reactive over the frequency range of interest even though a large portion of the data was acquired at frequencies above the plane wave cutoff frequency of the tunnel test section. The cutoff frequency is at approximately 160-185 Hz depending on whether a square or circular cross section is assumed (recall the test section is actually octagonal).

The data are also very repeatable. This is evident from comparisons of 0-2500 Hz and 0-5000 Hz data sets that were acquired at different times. Figure 7.1 is an overlay of the bias error calculated from data acquired over each of these frequency ranges, for the case of 30.5 m/s flow, and $\Delta r = 13.5$ mm. It can be seen that even though the data were acquired at different times and with different resolution bandwidths, the bias error calculations are very similar over the common frequency range. Appendix A contains the individual bias error calculations for

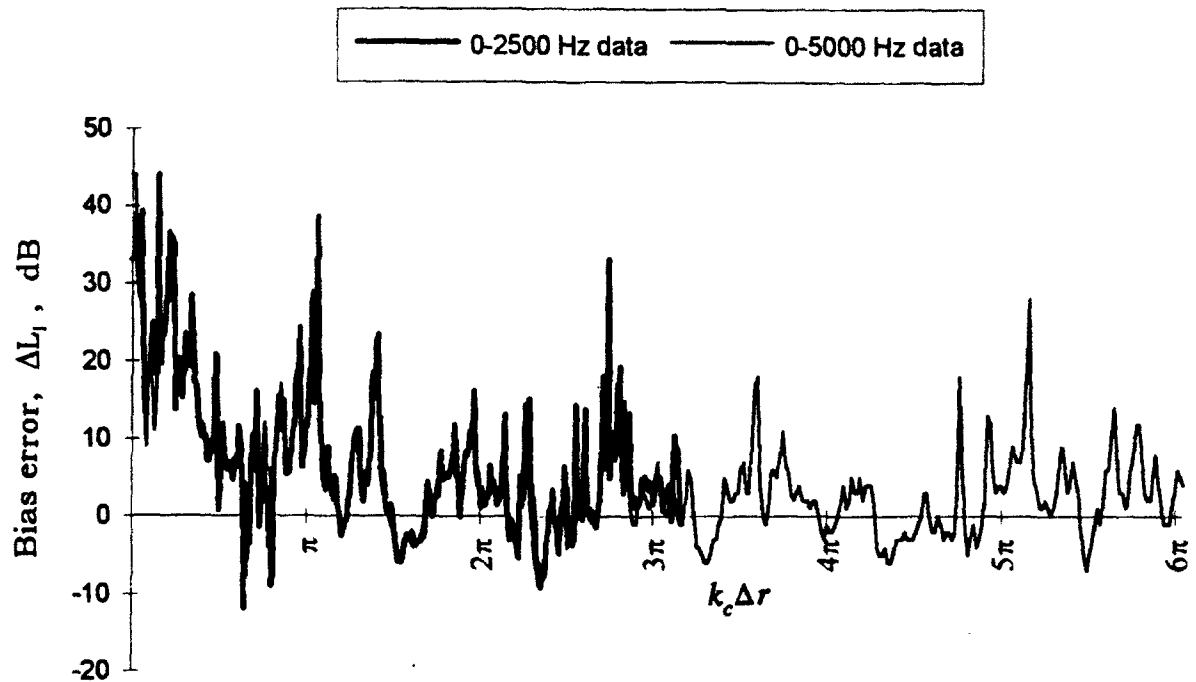


Figure 7.1 Verification that the calculated errors are bias errors

each of the curves in figure 7.1 (table 6.1 may help to identify these figures). Appendix B contains the individual intensity spectra for the same conditions and show that the intensity spectra are also basically equivalent over the common frequency range.

This repeatability helps validate the data and also proves that the error calculated is indeed a bias error and not a random error. The repeatability further assures that this error can be measured accurately in a severe environment where: the mean flow Mach number approaches 0.1; the acoustic field contains higher order modes (not pure plane wave

propagation); and the coherence between adjacent sensors is not necessarily close to 1. The bias error calculations presented in Appendix A are repeatable even when the coherence ranges from 0.5 to 0.9. Repeatability degrades when the coherence is less than 0.5.

7.2 Conclusions From the Bias Error Calculations

The bias error plots of Appendix A generally follow the shape of a $(\sin x)/x$ curve as shown in figure 6.1 and predicted by Lauchle.⁵ This is especially true at lower mean flow velocities. As the mean flow velocity increases and approaches $M = 0.1$, the bias error increases at all the separation distances. This is attributed to the decrease in the signal-to-noise (S/N) ratio as the mean flow velocity increases. Lauchle,⁵ expressed the signal-to-noise ratio for pressure spectrum measurements as

$$\frac{S}{N} = \frac{G_{aa}}{G_{\tau\tau}},$$

where G_{aa} is the acoustic pressure auto-spectrum as measured with the acoustic source on and no mean flow, while $G_{\tau\tau}$ is the auto-spectrum of the turbulent boundary layer pressure field as defined previously. As the flow velocity increases $G_{\tau\tau}$ increases but the source output level remained constant for all the tests; thus, the S/N ratio decreases as flow velocity increases. If the S/N ratio were to remain constant for all

conditions, it is predicted that the bias error curves would maintain the form shown in figure (6.1); even as the Mach number approached 0.1. This particular S/N ratio may not be appropriate for intensity measurements. Oswald and Donavan⁴ defined a S/N ratio where the signal term was the intensity of the acoustic source and the noise term was the intensity measured on just one sensor in the presence of flow, defined to be $\overline{p^2}/\rho c$. Here, $\overline{p^2}$ is the mean square pressure (flow and acoustic) measured by the microphone and ρc is the characteristic acoustic impedance of the medium.

The reader should be aware that although the bias error increased as the mean flow velocity increased, the ability to calculate accurately the bias error did not degrade. This ability to calculate accurately the bias error, even at relatively high flow velocities and sensor separations, is vital to realizing the potential of this technique.

The fact that the bias error plots agree (in principle) with figure (6.1) indicates, as Lauchle⁵ predicted, that there is indeed a rapid decorrelation of the turbulent energy as $k_c \Delta r$ increases. The correlation length, Λ , approximately equals the sensor separation distance, Δr , at the value $k_c \Delta r = 2.75$. Above this value of $k_c \Delta r$, $\Delta r > \Lambda$ and there should be little or no correlation in the turbulent pressure field between the two adjacent microphones.

The coherence between the sensors generally tends to decrease as

sensor separation distance increases. The exception was at the highest flow speed tested, 30.5 m/s, where the Mach number approached 0.1. In this case the coherence increased as Δr increased. The associated bias error increased with the increase in Δr .

7.3 Conclusions From the Intensity Spectra

Intensity spectra overlay plots are shown in Appendix B. The directionality of the intensity vector clearly indicates that the region of correlated turbulence energy decreases as sensor separation increases. This is as expected. The directionality also shows that the correlated turbulent pressure field contributions are most significant below $k_c \Delta r = \pi$, which is again expected based on predictions by Lauchle.⁵ This is true for all flow speeds and sensor separation distances considered.

The overlay plots at the bottom of each figure in Appendix B provide an indication of the signal-plus-noise-to-noise $\left(\frac{S+N}{N}\right)$ ratio. Comparison for the different parameters reveals that this ratio decreases as the sensor separation, Δr , increases and also decreases as the mean flow velocity increases. This can be seen by comparing figures B-3 to B-5 for the effects of increasing Δr , and figures B-3 to B-6 for the decrease observed when increasing flow velocity. The same is true for the signal-

to-noise (S/N) ratio, where this ratio is defined here as the ratio of the acoustic intensity (source ON, no flow) to that of the turbulence intensity (Source off, with flow).

For each test condition with given mean flow and sensor separation, both the $\left(\frac{S+N}{N}\right)$ ratio and the S/N ratio increases with increasing $k_c \Delta r$.

This is illustrated in Figure B-4 for the $\left(\frac{S+N}{N}\right)$ ratio.

Oswald and Donovan⁴ reported that when the S/N ratio was low, the acoustic intensity oscillated in direction. This could explain some of the oscillations in direction for the intensity spectra, especially above $k_c \Delta r = 2.75$ which is approximately where $\Delta r = \Lambda$. This would also explain the corresponding increase in the bias error that often occurs in these regions of energy flow oscillations.

7.4 Conclusions From the Pressure Intensity Indices

Recall from Chapter 3 that $|\delta_{pIR} - \delta_{pl}| > 7\text{dB}$ indicates an error in the estimate of intensity of less than 1dB. The absolute value sign is used here since the Zonic software utilizes the alternate convention $\delta_{pl} = L_i - L_p$ as opposed to the more commonly accepted $\delta_{pl} = L_p - L_i$. The plots in Appendix C show that $|\delta_{pIR} - \delta_{pl}|$ is generally much greater than 7 dB and consequently the error due to phase mismatch is negligible. This was expected due to the careful phase calibrations and the quality

instrumentation employed.

The pressure intensity index data helps to characterize the acoustic field. If the acoustic field is reactive $\phi_{12} \rightarrow 0$, and $\delta_{pIR} - \delta_{pl} \rightarrow 0$. Since $|\delta_{pIR} - \delta_{pl}| \gg 0$ in this study, the reactivity of the acoustic field was not a significant concern. This is an important point because a large portion of the data was acquired at frequencies above the cutoff frequency for plane wave propagation in the tunnel test section; consequently, higher order modes exist in the intensity data presented.

7.5 Summary and Recommendations

The technique developed by Lauchle⁵ appears to be a very viable method for determining the contributions of the non propagating turbulent pressure field acting on the face of flush-mounted sensors when acquiring acoustic intensity measurements in the presence of low Mach number mean flow. The data generally yield similar trends in the intensity bias error for all the various combinations of sensor separation distances and flow velocities.

It would be desirable to conduct another independent experiment for comparison. In such an event, it would be recommended that a broader resolution bandwidth be used during the data acquisition. This will decrease the data acquisition time for a comparable number of ensembles and also decrease the size of each data file. The narrower

bandwidths require large data sets that utilize large amounts of computer memory, take longer to process, and are generally more difficult to handle during calculations and data manipulation. Shortening the data acquisition time reduces the possibility of additional errors due to non-stationary behavior of the facility.

Now that the technique has been validated for an arbitrary and spatially complex sound field, it would be desirable to conduct the experiment in a plane wave acoustic field to determine if the bias error at flow velocities near $M=0.1$ will even better match that shown in figure 6.1. Evaluating the non-dimensionalized bias error in such a field would also be desired. Incorporation of a smoothing algorithm for the turbulent pressure spectrum, G_{TT} , (as well as the intensity spectra) may need to be considered for this non-dimensionalization.

Varying the S/N ratio to evaluate its effect on the bias error would be very useful. A S/N threshold could be determined, above which the bias error is minimized. Oswald and Donovan⁴ did S/N measurements for the case where an intensity probe equipped with pointed nose cones was situated in the free stream. They determined that there was no error (less than 0.5 dB was considered no error) until the S/N ratio fell below - 5 dB. Thus, the acoustic intensity could be as much as 5 dB lower than the turbulence wind noise intensity.

REFERENCES

1. Williams, E.G., Dardy, H.D., and Fink, R.G., "A Technique for Measurement of Structure-borne Intensity in Plates," *J. Acoust. Soc. Am.*, **78** (1985) pp. 2061-2068.
2. Carrol, G.P., "Structural Response and Power Flow Measurements Utilizing Cross Spectra" Ph.D. Thesis, Catholic University, (1987).
3. Loyau, T., Pascal, J., Gaillard, P., "Broadband Acoustic Holography Reconstruction From Acoustic Intensity Measurements. I: Principle of the method." *J. Acoust. Soc. Am.*, **84** (5) (1988) pp. 1744-1750.
4. Oswald, L.J., and Donovan, P.R., "Acoustic Intensity Measurements in Low Mach Number Flows of Moderate Turbulence Levels," General Motors Research Publication GMR-3269, April 24, 1980.
5. Lauchle, G.C., "Effect of Turbulent Boundary Layer Flow on Measurement of Acoustic Pressure and Intensity," *Noise Control Eng. J.*, **23** Sep-Oct (1984) pp. 52-59.
6. Fahy, F.J., "Measurement of Sound Intensity in Low Speed Turbulent Airflow," in *Proc of the 2nd Symposium on Acoustic Intensity*, (Jan 1988) pp. 127-134.
7. Comparin, R.J., "Acoustic Intensity Measurements in the Presence of Mean Flow with Application to Noise Measurements in a Wind Tunnel," *J. Acoust. Soc. Am.*, **90**(4) (1991) pp. 1733-1741.
8. Olson, H. F., "System Responsive to the Energy Flow of Sound Waves." U.S. Patent No, 1,892,644 (1932).
9. Clapp, C. W. & Firestone, F. A., "The Acoustic Wattmeter, an Instrument for Measuring Sound Energy Flow." *J. Acoust. Soc. Am.*, **13** (1941) pp. 124-136.

10. Schultz, T. J., "Acoustic Wattmeter", *J. Acoust. Soc. Am.*, **28** (1956) pp. 693-99.
11. Bolt, R. H. & Petrauskas, A. A., "An Acoustic Impedance Meter for Rapid Field Measurements", *J. Acoust. Soc. Am.*, **15** (1943) 79(a).
12. Urick, R.J., *Principles of Underwater Sound*, 3rd Edition, McGraw Hill Inc., New York, 1983.
13. *Sound Intensity*, a booklet by Bruel & Kjaer, 1986.
14. Fahy, F.J., *Sound Intensity*, Elsevier Applied Science, New York, 1989.
15. Elko, G.W., "Frequency Domain Estimation of the Complex Acoustic Intensity and Acoustic Energy Density," Ph.D. Thesis, Pennsylvania State University, (1984).
16. Brungart, T.A., Lauchle, G.C., Tichy, J., "Case History: Acoustic Diagnostics of an Automotive HVAC System," *Noise Control Eng. J.* **39** (1992) pp. 31-42.
17. Gade S., "Sound Intensity (Part 1 Theory)" Bruel & Kjaer Technical Review 3, (1982) pp. 3-39.
18. Shirahatti, U.S., and Crocker, M.J., "Two-Microphone Finite Difference Errors in the Interference Fields of Point Dipole Sources", *J. Acoust. Soc. Am.*, **92**(1) (1992) pp. 258-267.
19. Fahy F.J., "Measurement of Acoustic Intensity Using the Cross - Spectral Density of Two Microphone Signals," *J. Acoust. Soc. Am.*, **62**(4), (1977) pp. 1057-1059.
20. Chung J.Y., "Cross-Spectral Method of Measuring Acoustical Intensity," General Motors Research Publication GMR-2617 (December 1977).
21. Waser, M.P., and Crocker, M.J., "Introduction to the Two Microphone Cross-Spectral Method of Determining Sound intensity," *Noise Control Eng. J.*, **22** (1984) pp. 76-85.

22. Bendat, J.S. & Piersol, A.G., *Random Data*, 2nd Edition, John Wiley & Sons Inc, New York, 1986.
23. Seybert, A.F., "Statistical Errors in Acoustic Intensity Measurements", *J. Sound & Vib.*, **75**(4) (1981) pp. 519-526.
24. Thompson, J.K. & Tree, D.R., "Finite Difference Approximation Errors in Acoustic Intensity Measurements," *J. Acoust. Soc. Am.*, **75**(2) (1981) pp. 229-238.
25. Rasmussen, G., "Phase Errors in Intensity Measurements," *Intensity Measurements - a collection of papers*, Bruel & Kjaer, (1984) pp. B1-B8.
26. Pascal, J.C., "Analytical Expressions for Random Errors of Acoustic Intensity," *Proceedings of Inter-noise 86*, edited by Robert Lotz, Noise Control Foundation, New York, (1986) pp. 1073-1076.
27. Gade, S., "Sound Intensity (Part II. Instrumentation and Applications," *Bruel & Kjaer Technical Review 4*, pp. 3-32 (1982).
28. Jacobsen, F. and Ren, M., "A Simple Technique for Improving the Performance of Intensity Probes", *Noise Control Eng. J.*, **38** Jan-Feb (1992) pp. 17-25.
29. Munro, D.H. and Ingard, K.U., "On Acoustic Intensity Measurements in the Presence of Mean Flow", *J. Acoust. Soc. Am.*, **65** (6) (1979) pp. 1402-1406.
30. Josserand, M.A., and Lauchle, G.C., "Modeling the Wavevector-Frequency Spectrum of Boundary-Layer Wall Pressure During Transition on a Flat Plate", *Trans. ASME, J. Vib. and Acoust.*, **112** (1990) pp 523-524.

Appendix A
BIAS ERROR PLOTS

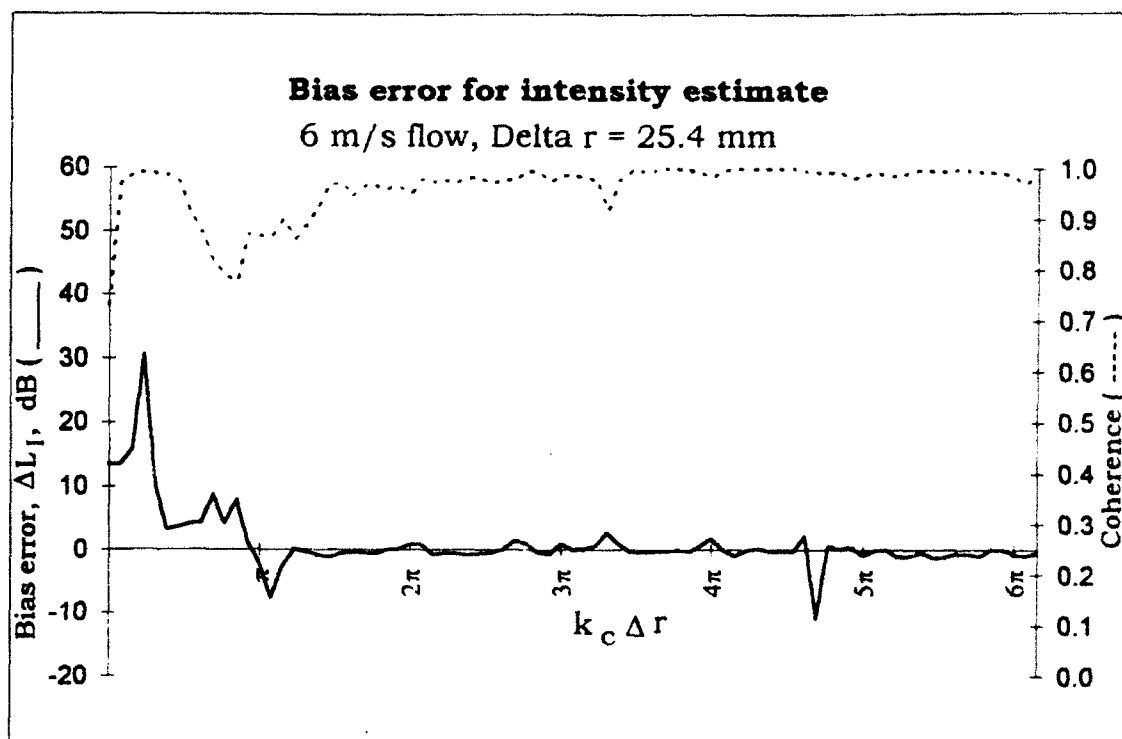


Figure A-1 Bias Error, 6 m/s flow, $\Delta r = 25.4$ mm

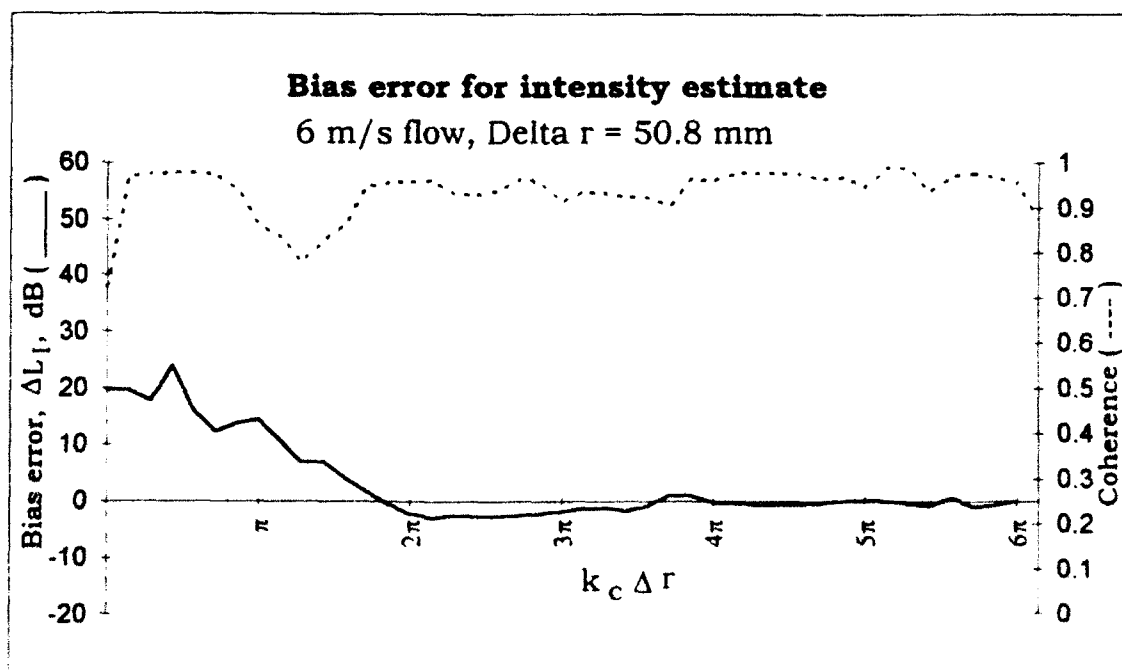


Figure A-2 Bias Error, 6 m/s flow, $\Delta r = 50.8$ mm

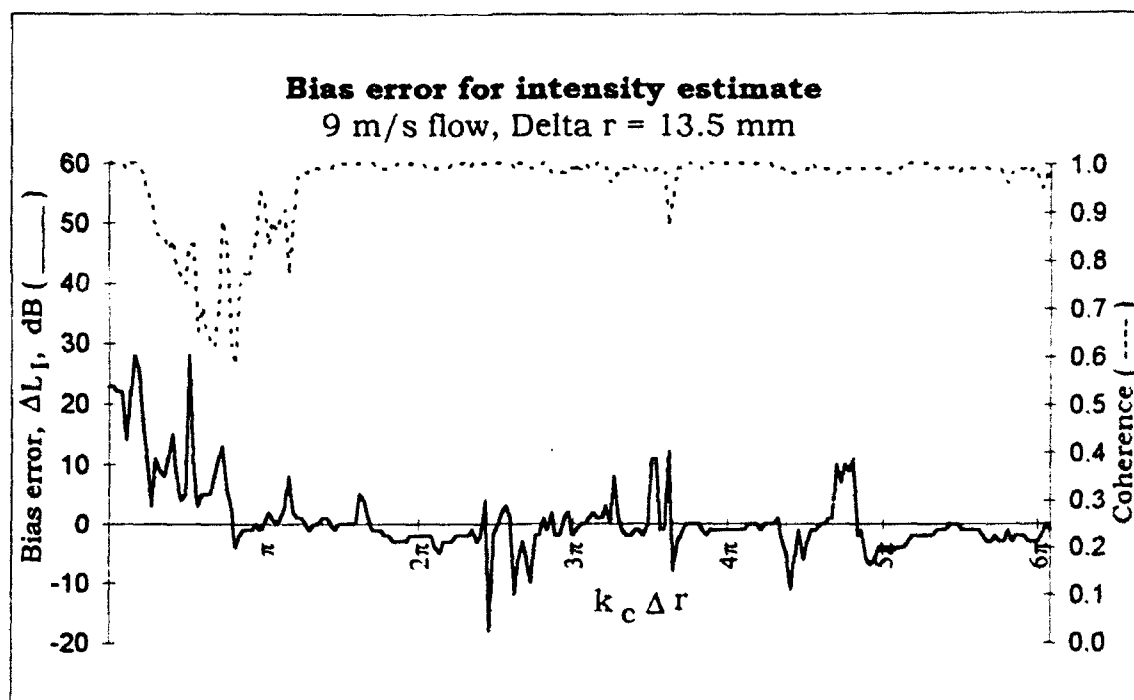


Figure A-3 Bias Error, 9 m/s flow, Delta r = 13.5 mm

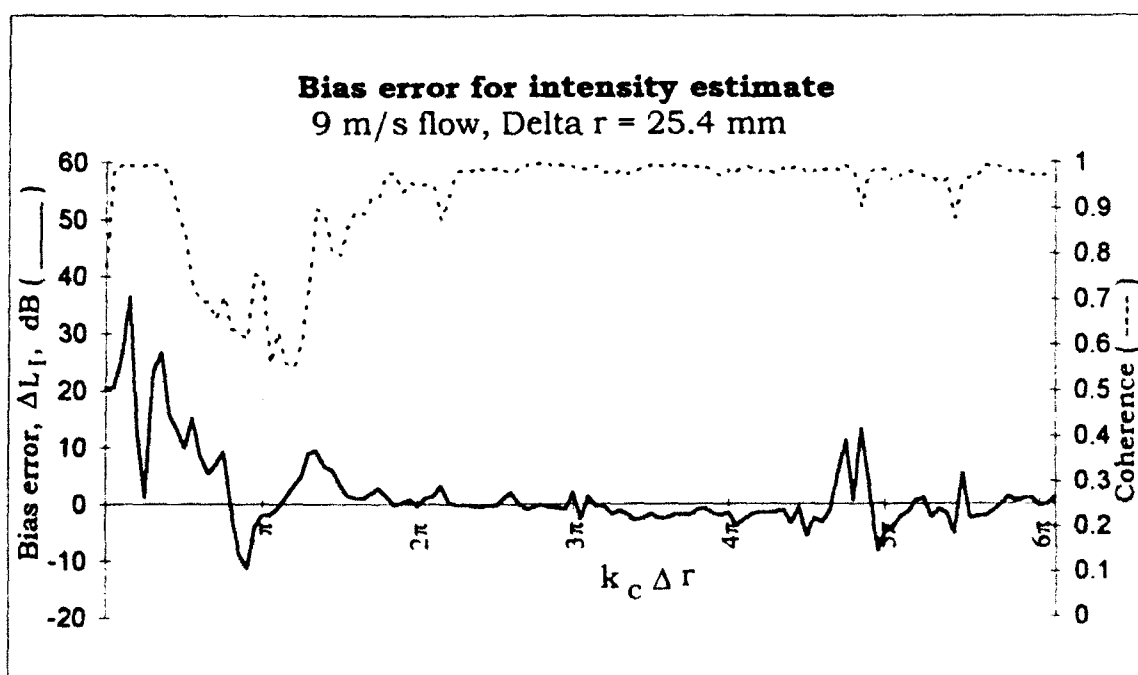


Figure A-4 Bias Error, 9 m/s flow, Delta r = 25.4 mm

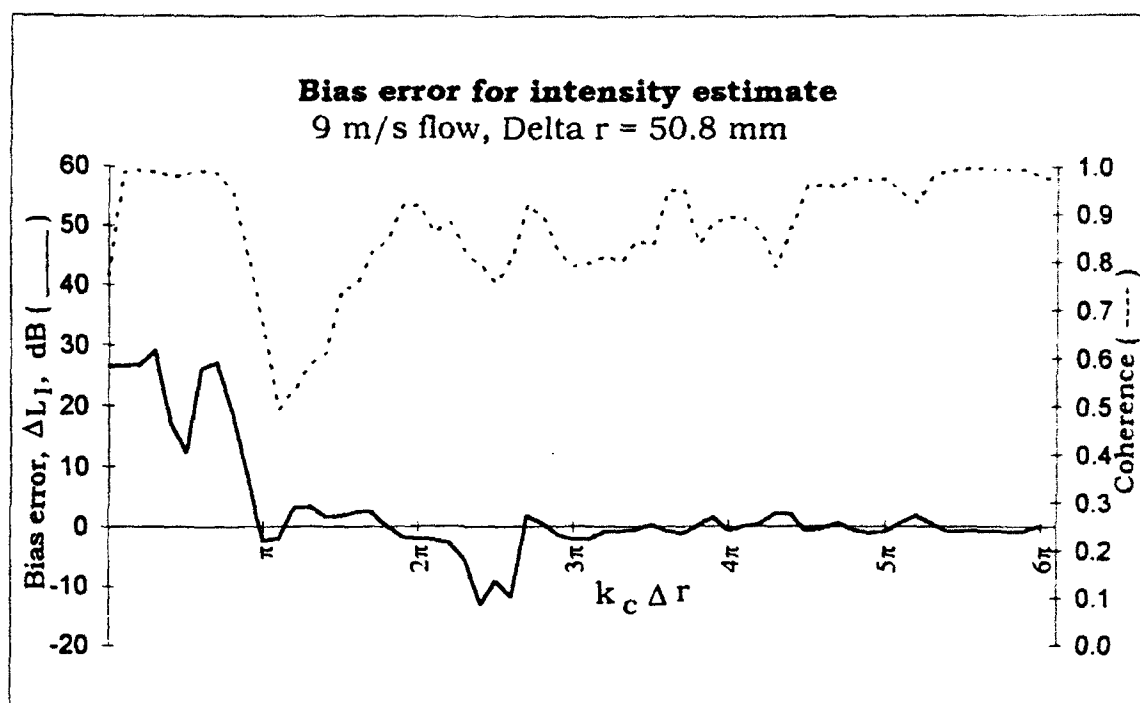


Figure A-5 Bias Error, 9 m/s flow, $\Delta r = 50.8$ mm

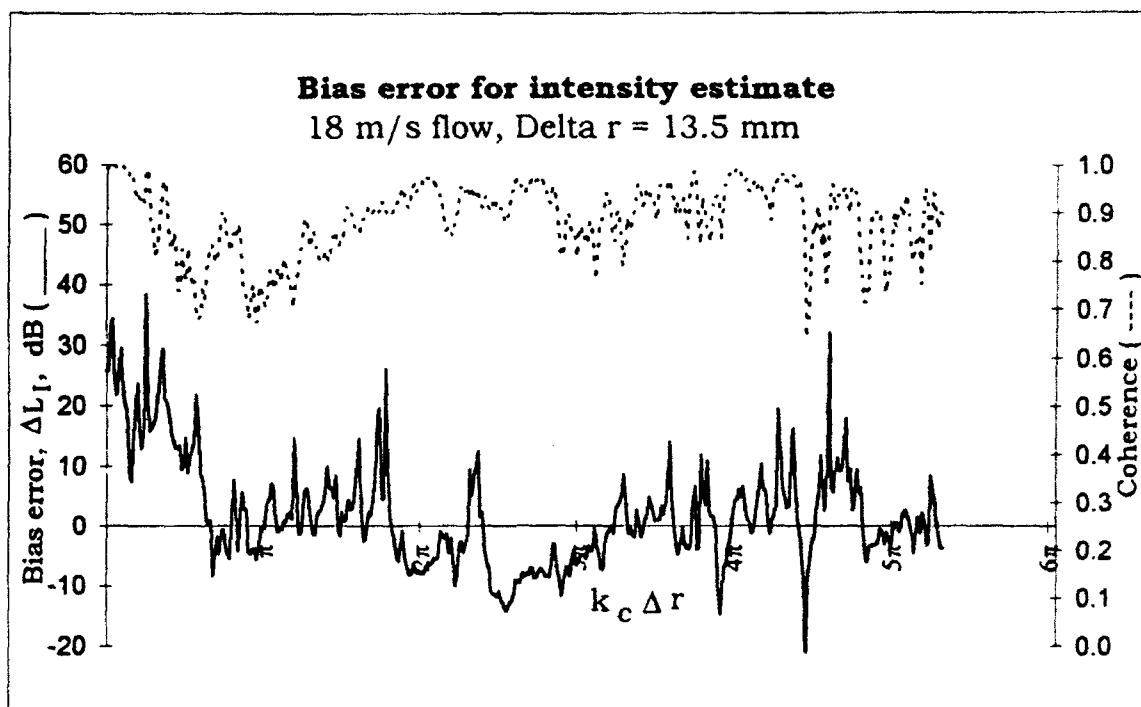


Figure A-6 Bias Error, 18 m/s flow, Delta r = 13.5 mm

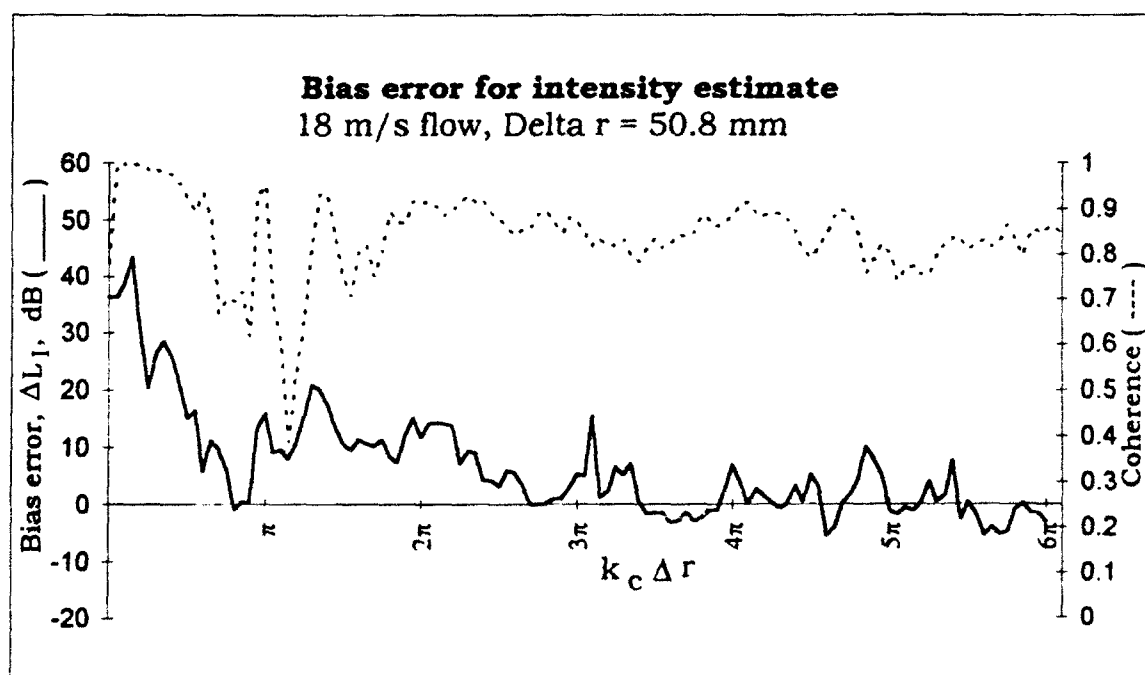


Figure A-7 Bias Error, 18 m/s flow, Delta r = 50.8 mm

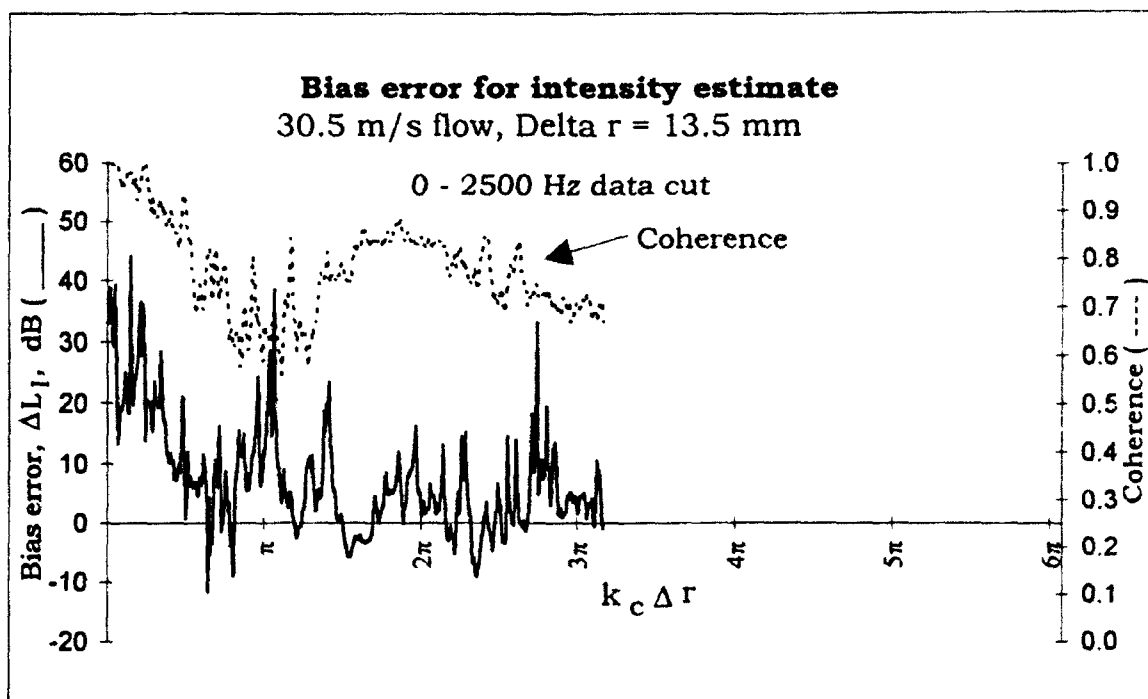


Figure A-8 Bias Error, 30.5 m/s flow, $\Delta r = 13.5$ mm, 0-2500 Hz

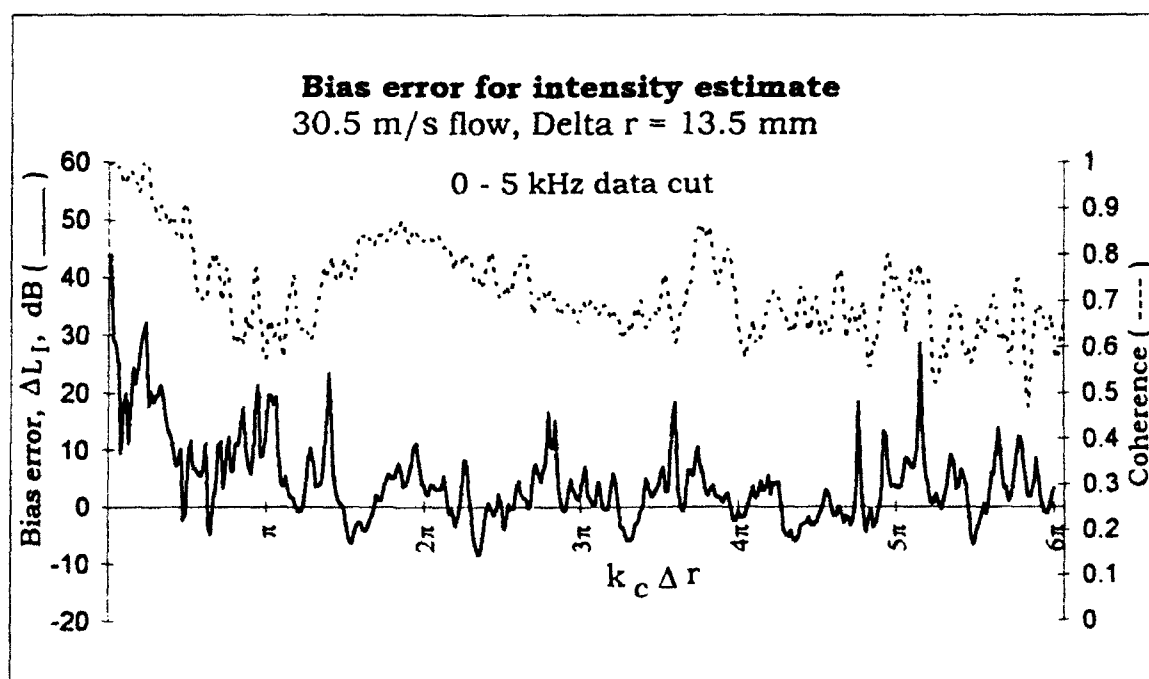


Figure A-9 Bias Error, 30.5 m/s flow, $\Delta r = 13.5$ mm, 0-5000 Hz

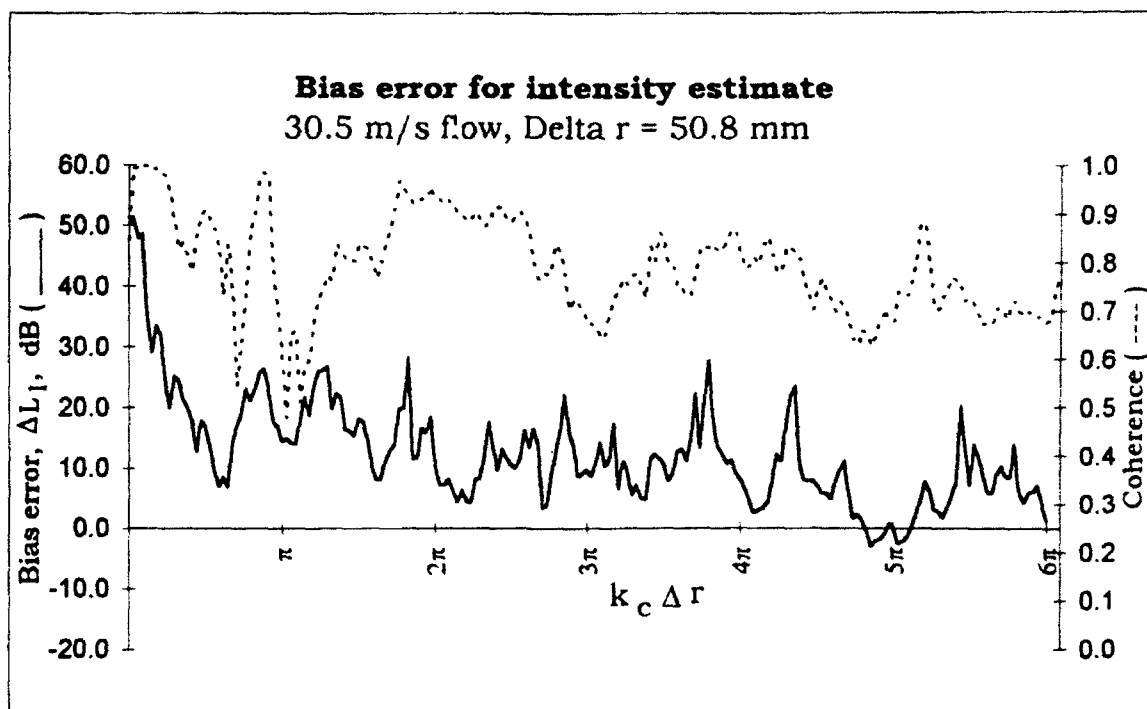


Figure A-10 Bias Error, 30.5 m/s flow, Delta r = 50.8 mm

Appendix B
ACTIVE INTENSITY PLOTS

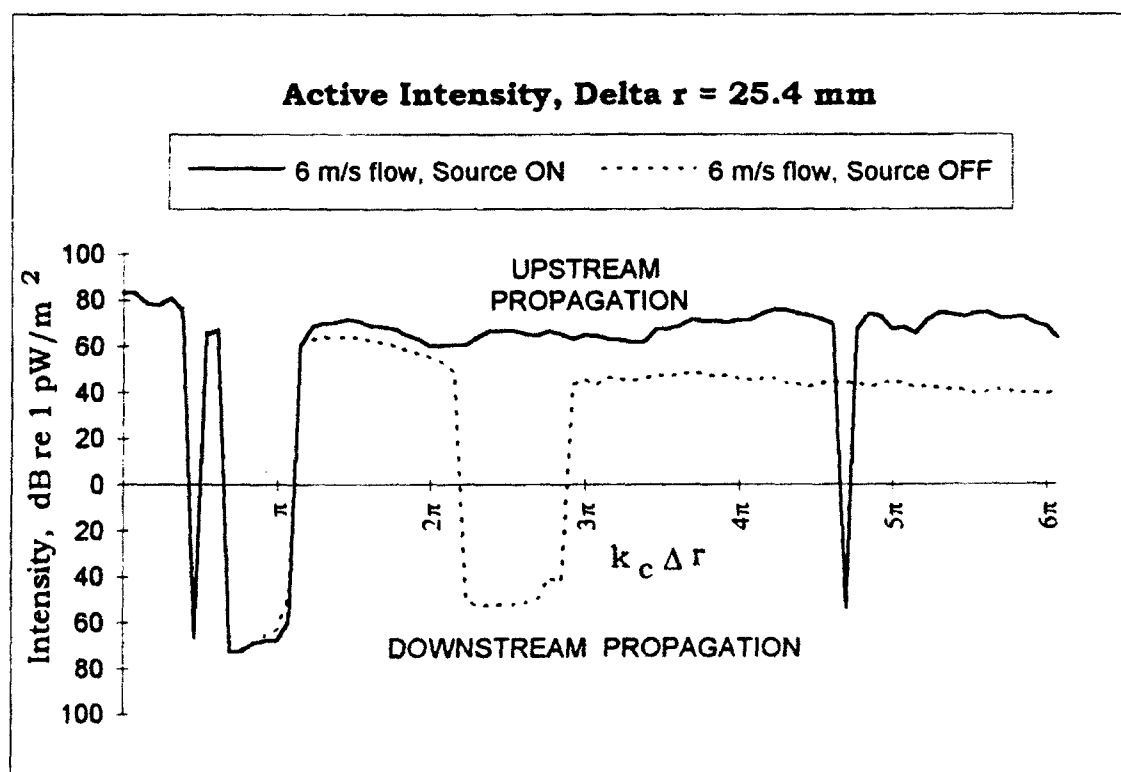
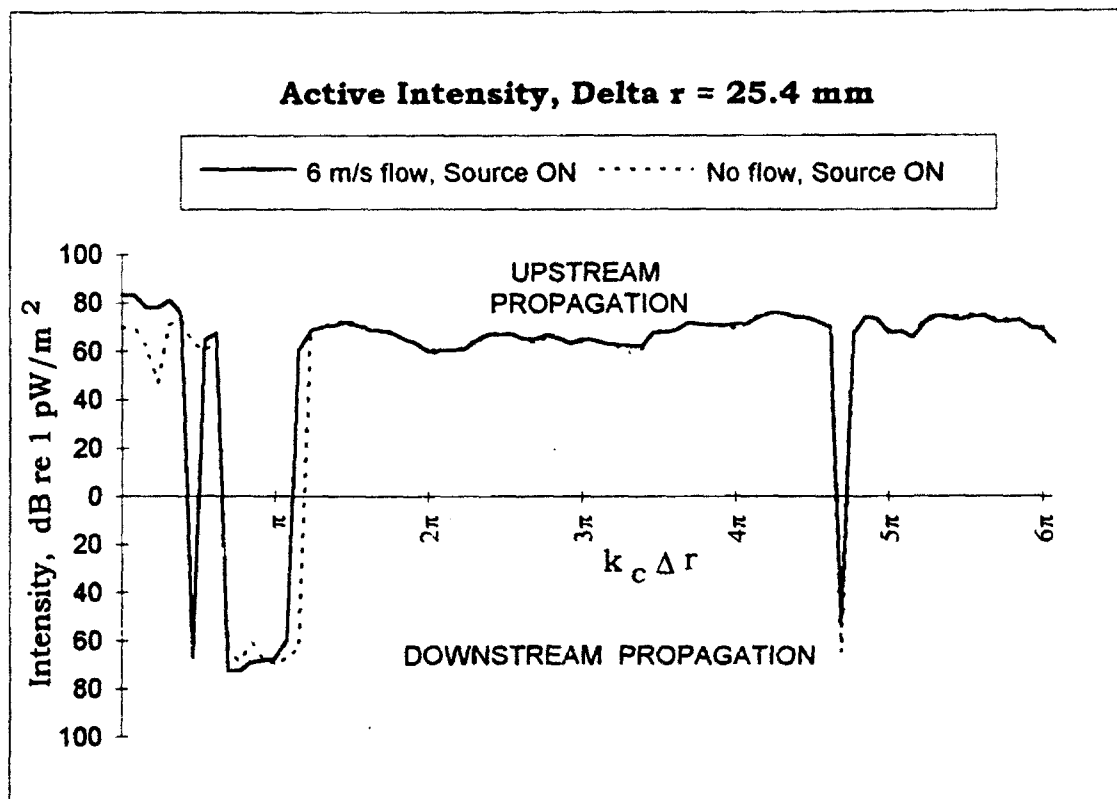


Figure B-1 Active Intensity, 6 m/s flow, Delta $r = 25.4$ mm

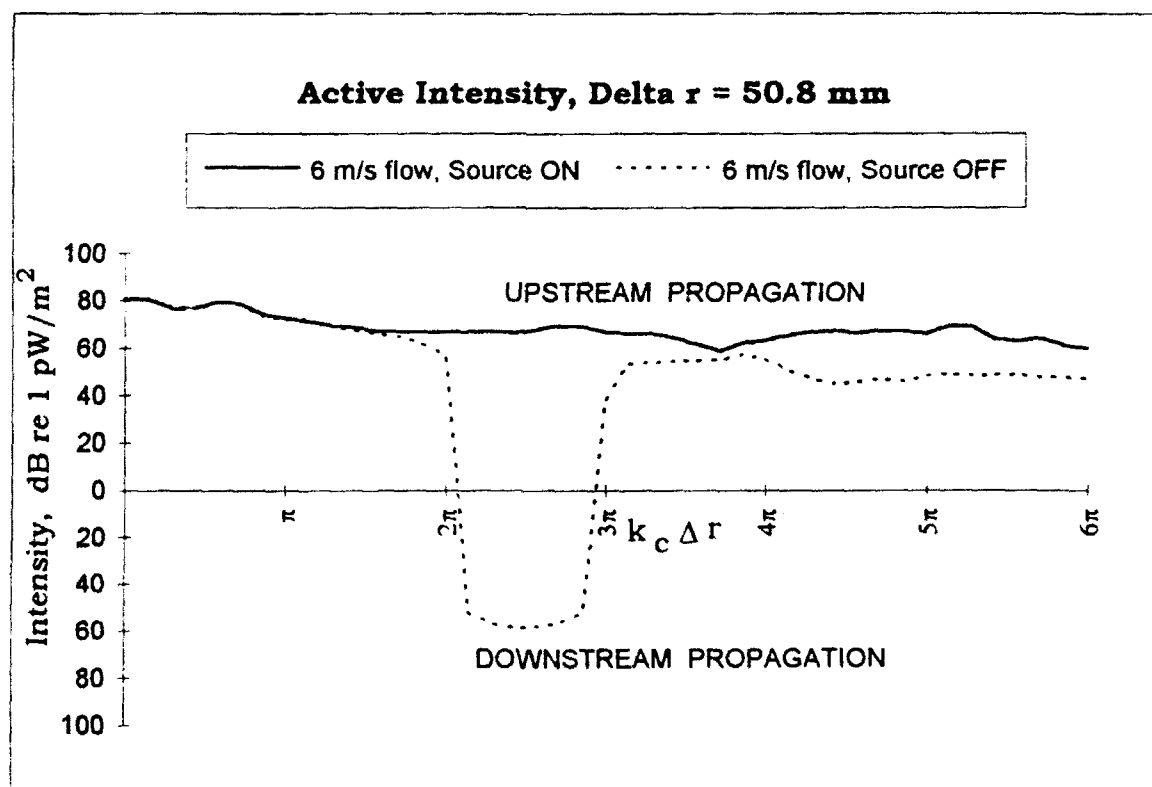
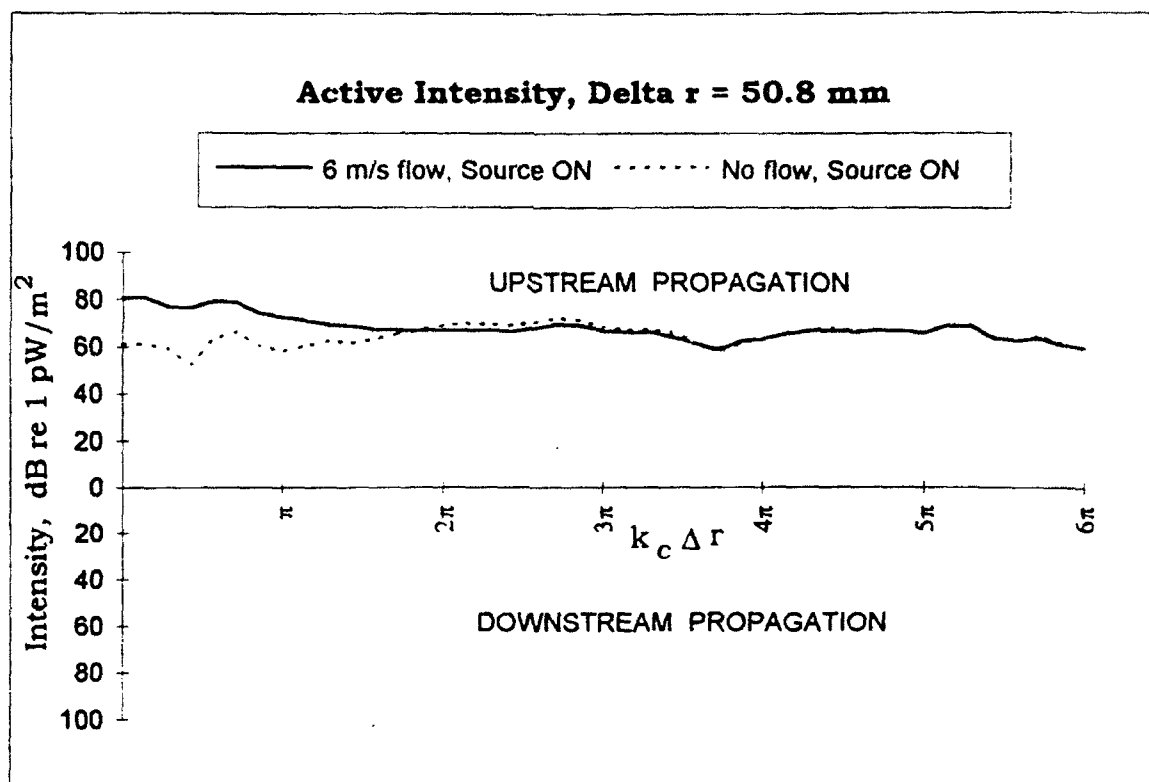


Figure B-2 Active Intensity, 6 m/s flow, Delta $r = 50.8$ mm

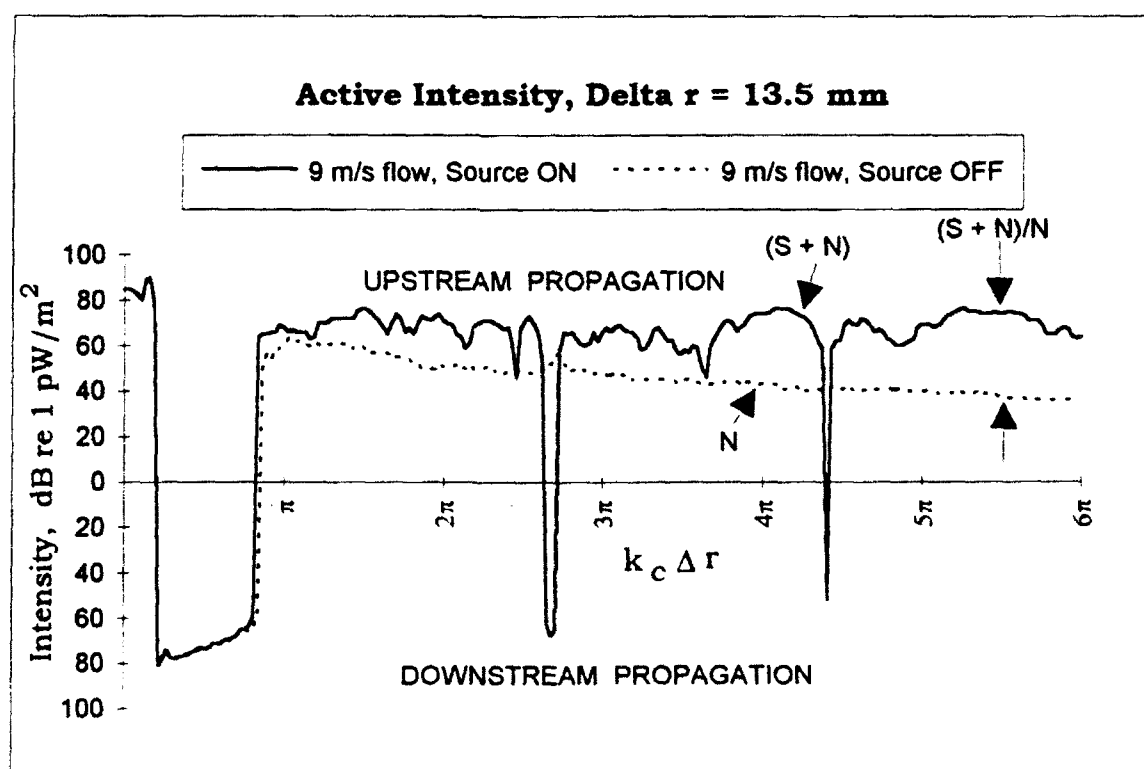
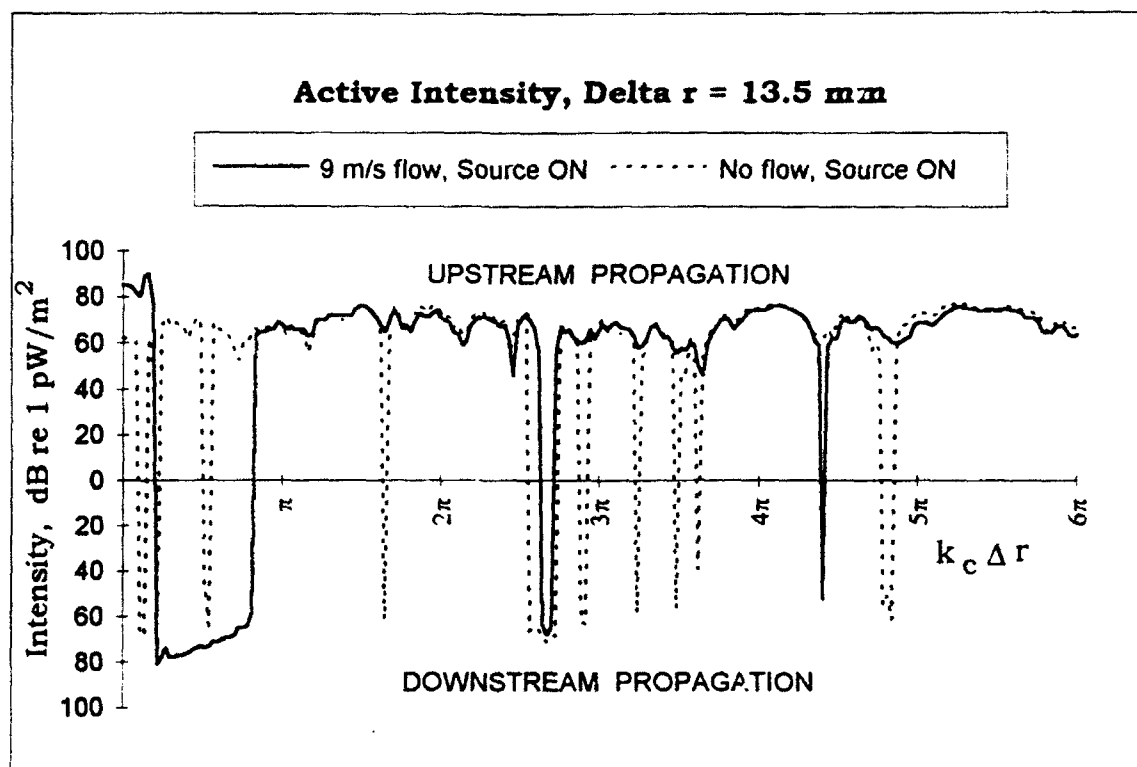


Figure B-3 Active Intensity, 9 m/s flow, Delta $r = 13.5$ mm

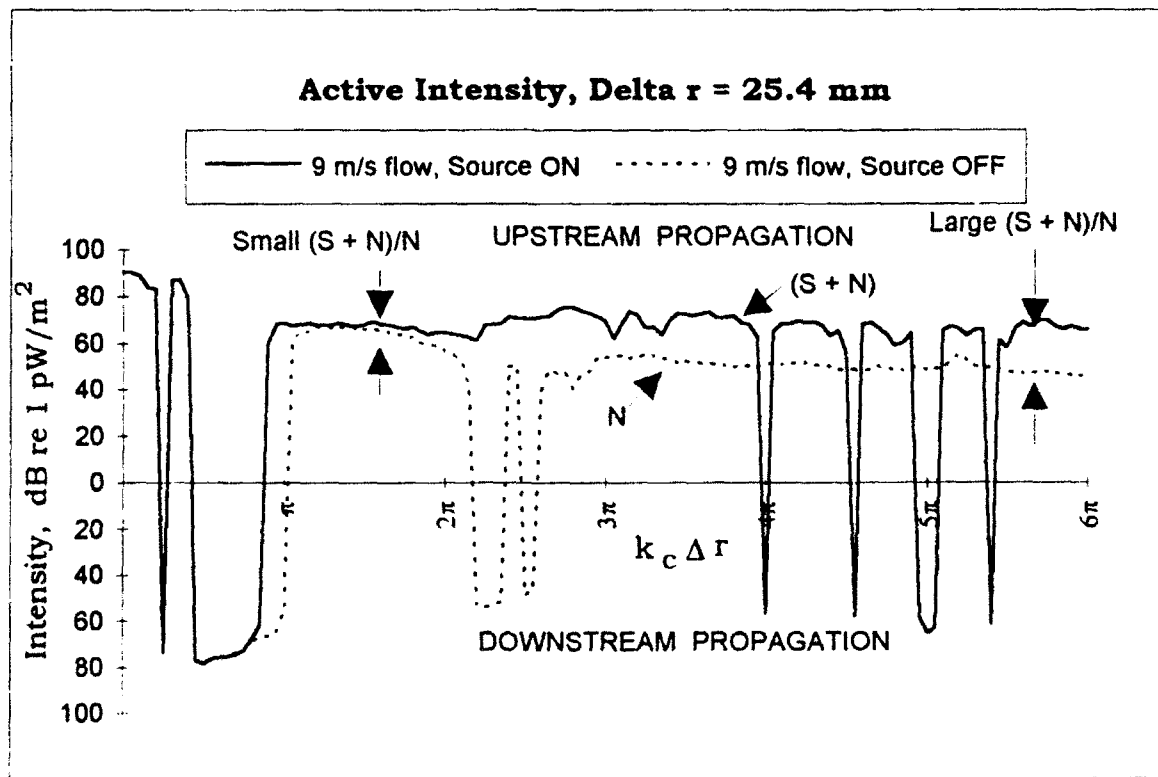
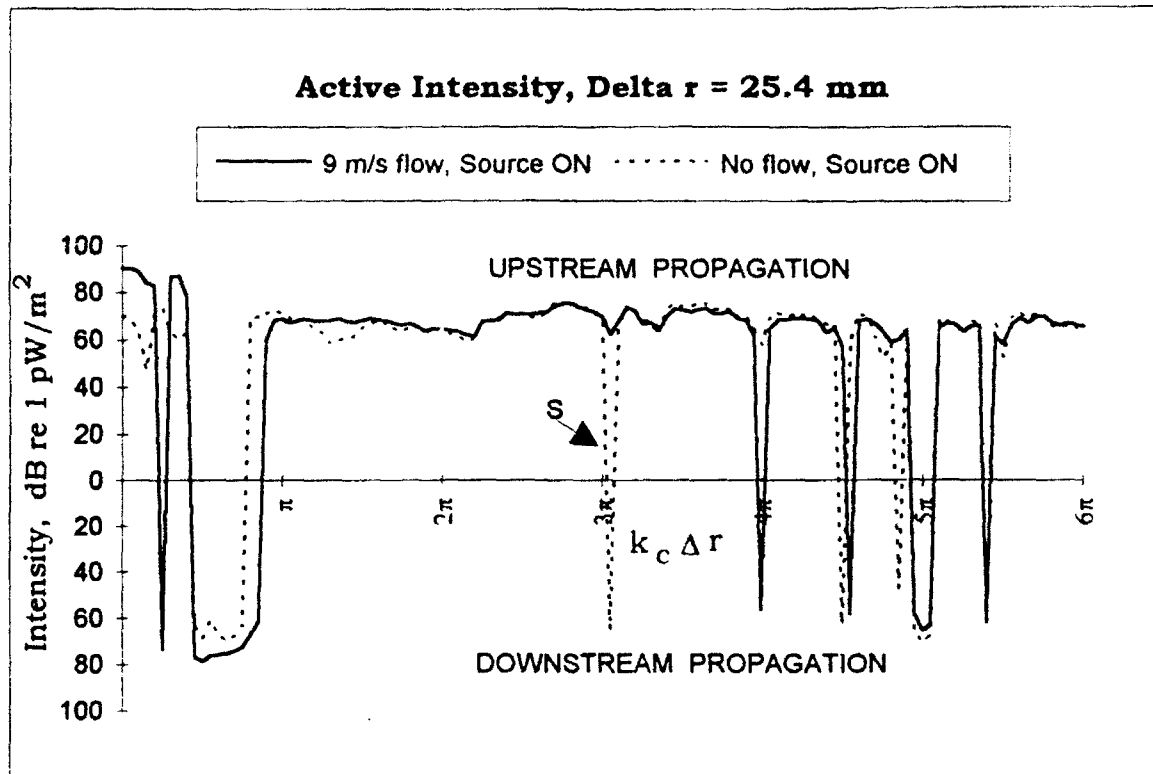


Figure B-4 Active Intensity, 9 m/s flow, Delta $r = 25.4$ mm

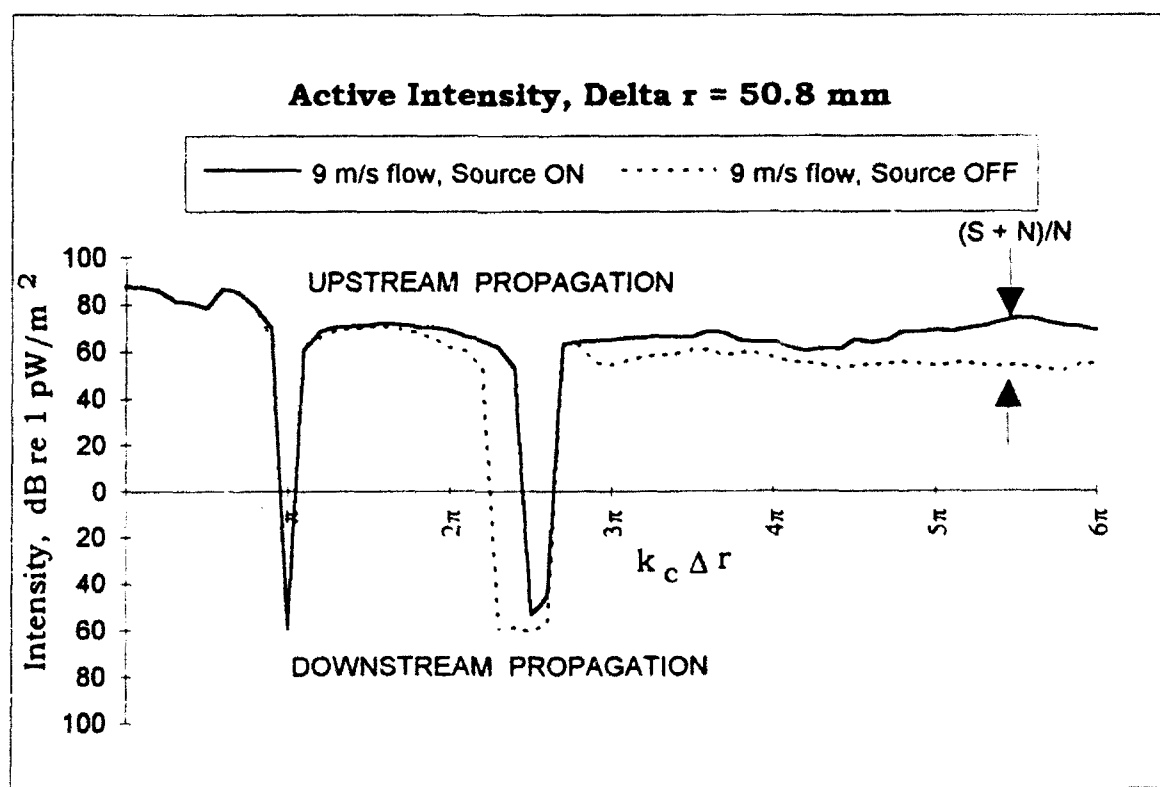
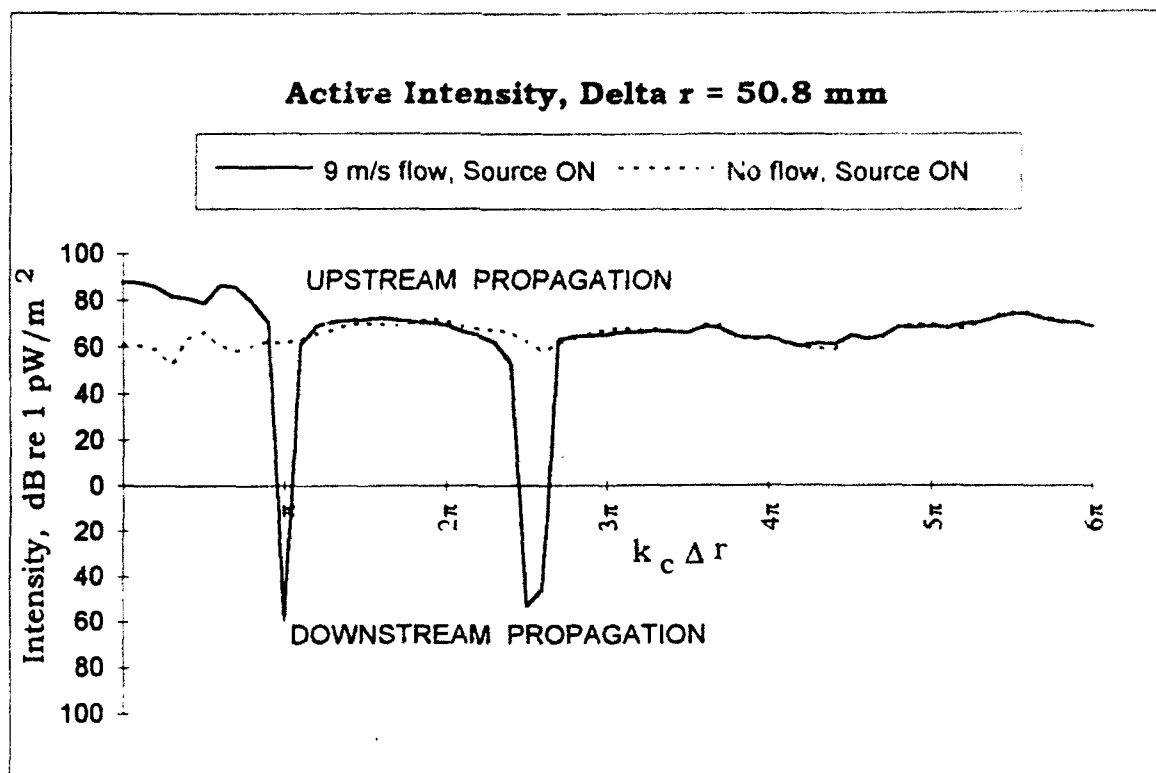


Figure B-5 Active Intensity, 9 m/s flow, Delta $r = 50.8$ mm

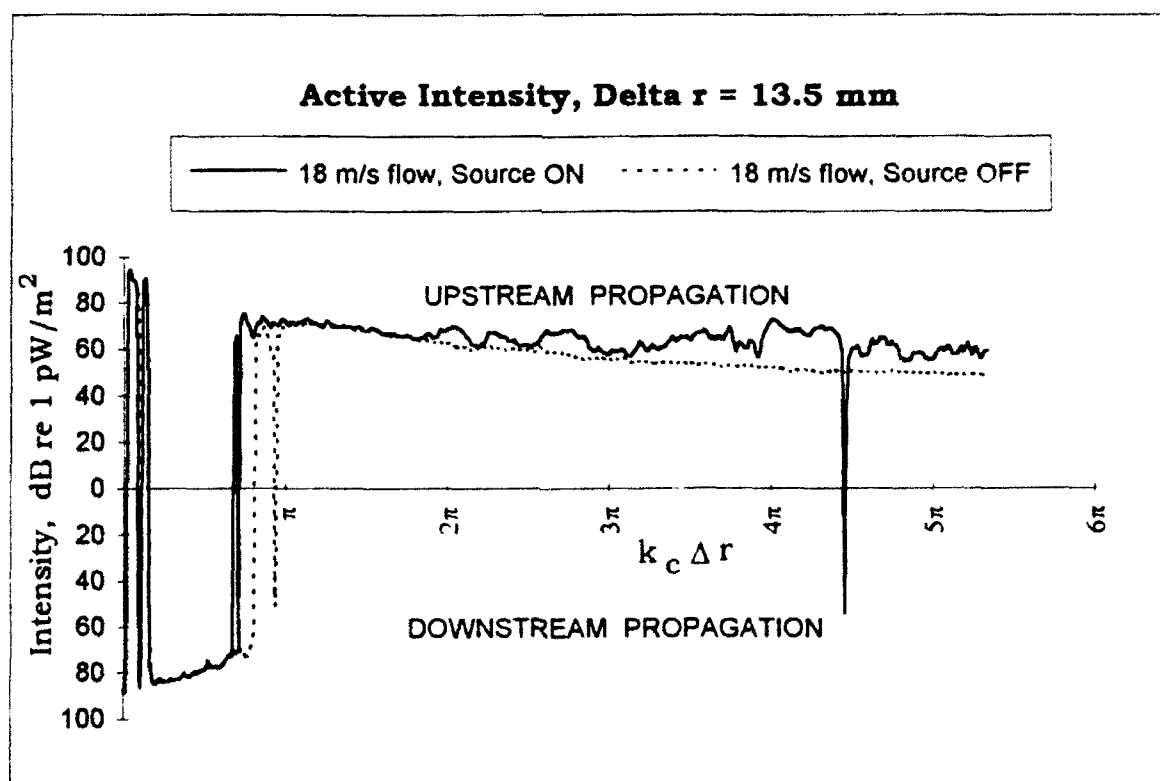
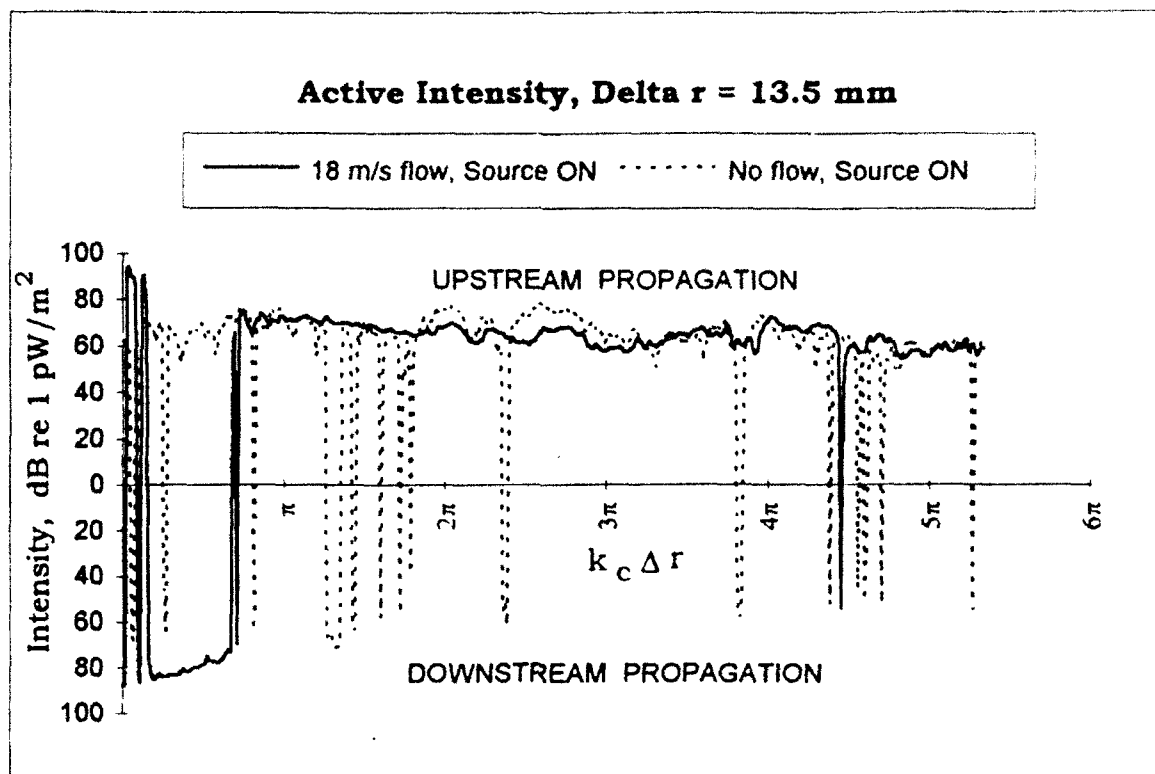


Figure B-6 Active Intensity, 18 m/s flow, Delta $r = 13.5$ mm

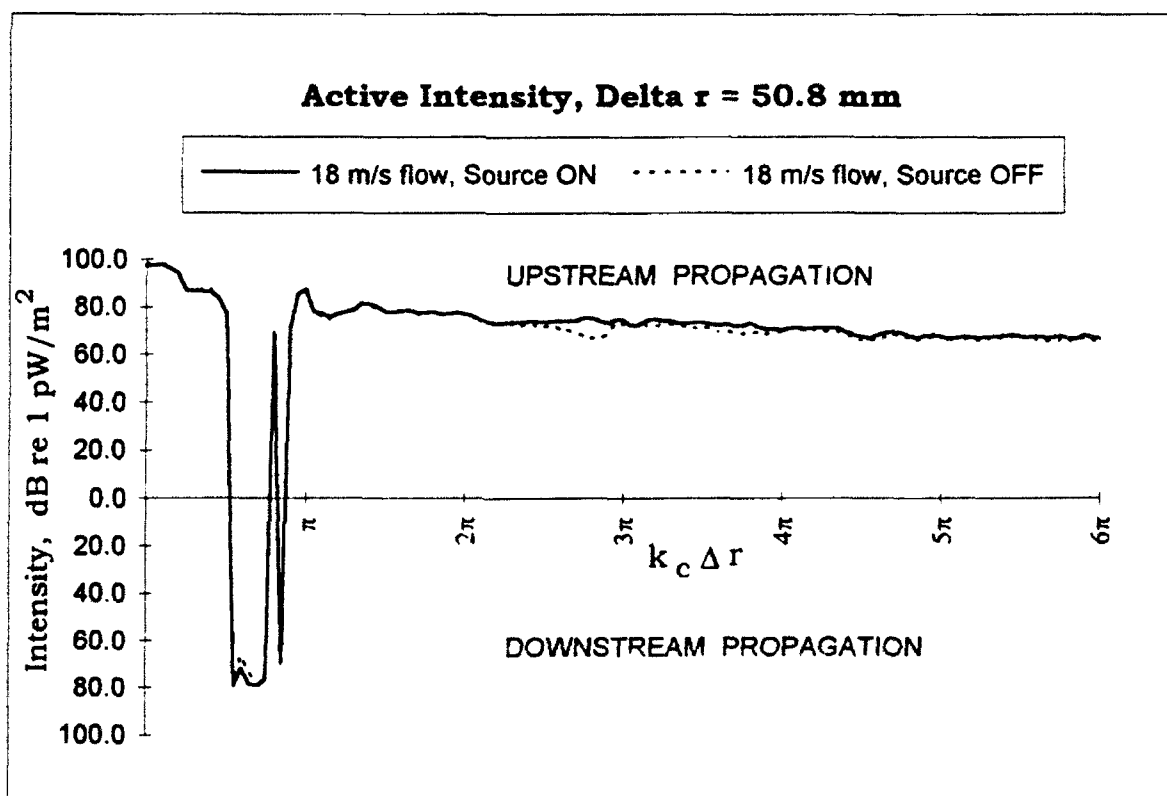
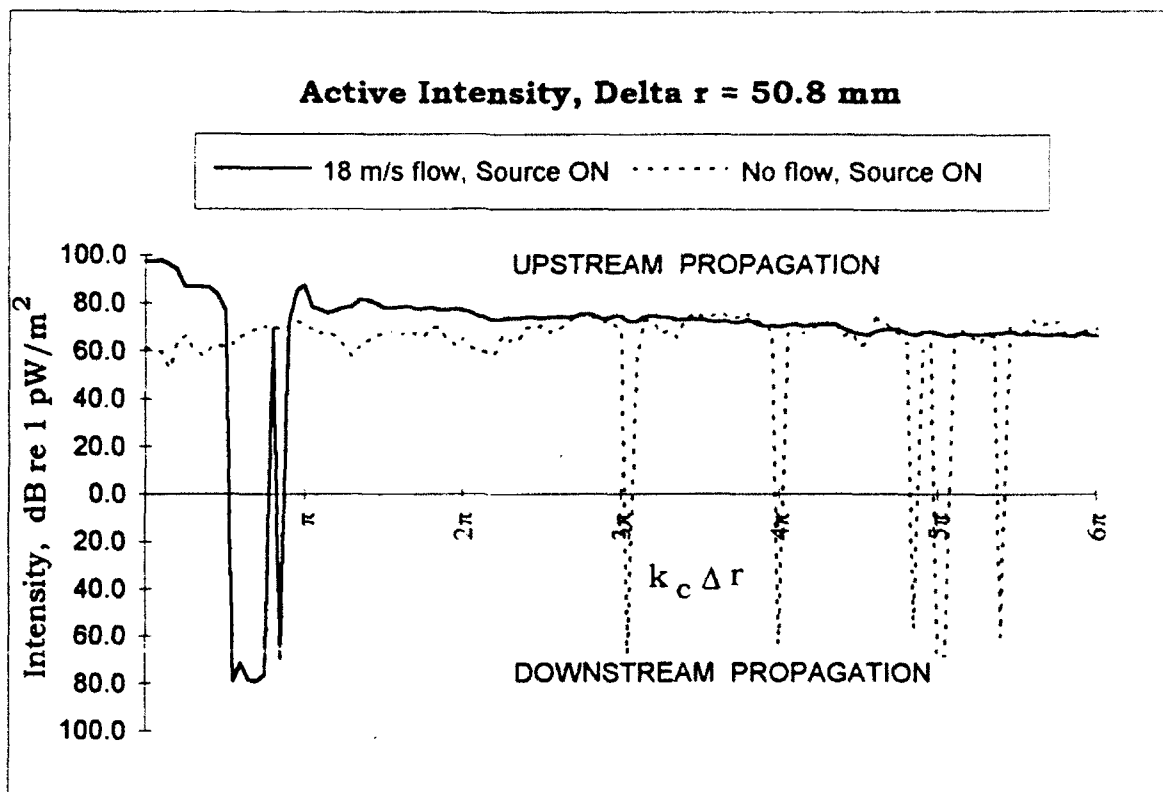


Figure B-7 Active Intensity, 18 m/s flow, Delta $r = 50.8$ mm

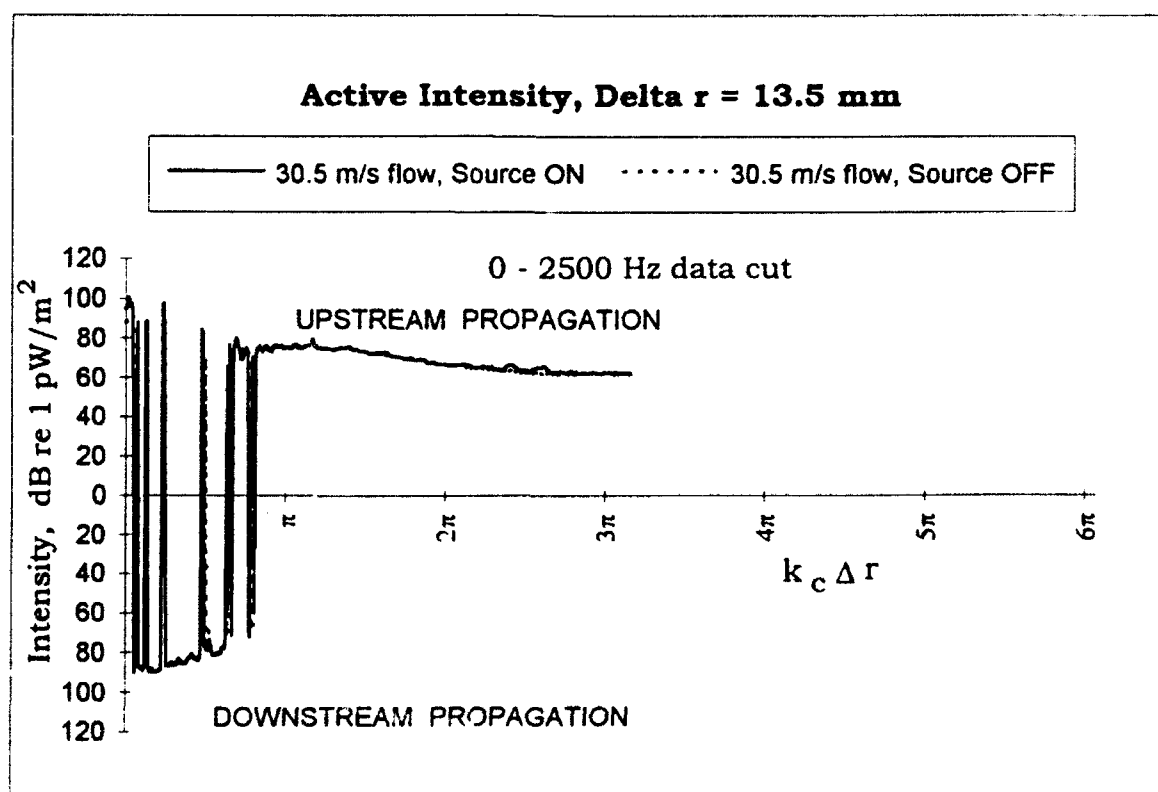
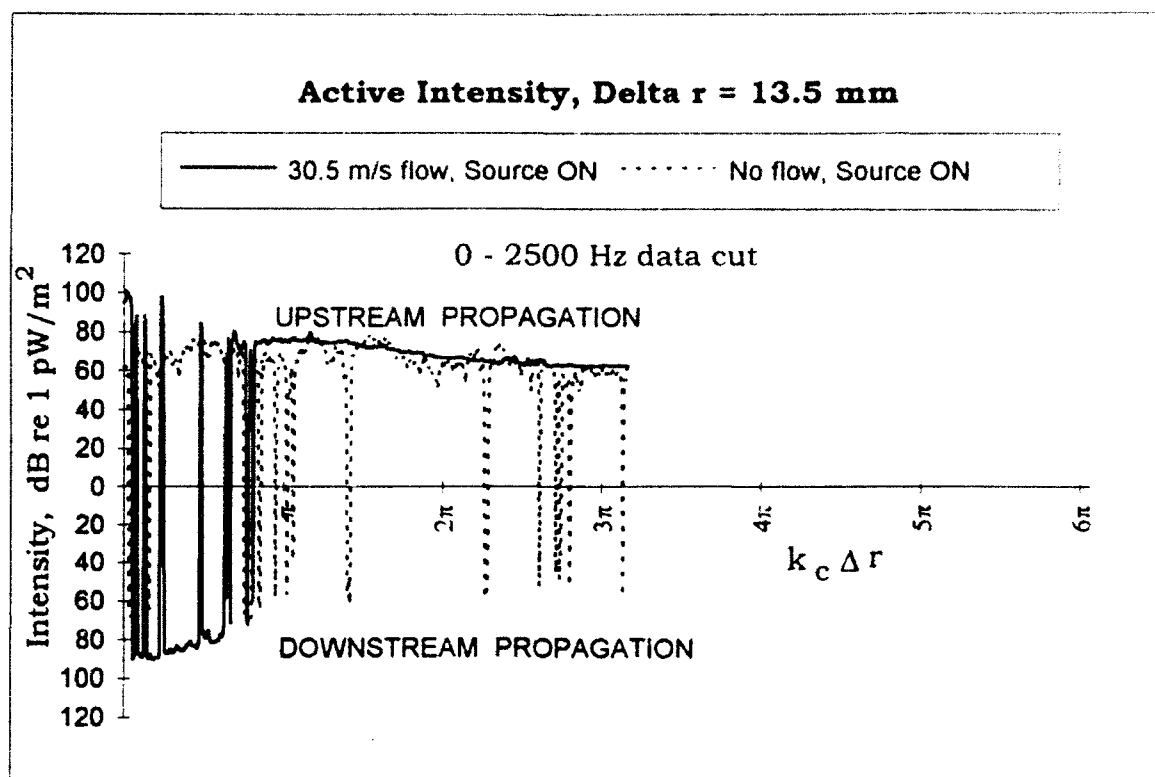


Figure B-8 Active Intensity, 30.5 m/s, Delta r = 13.5 mm

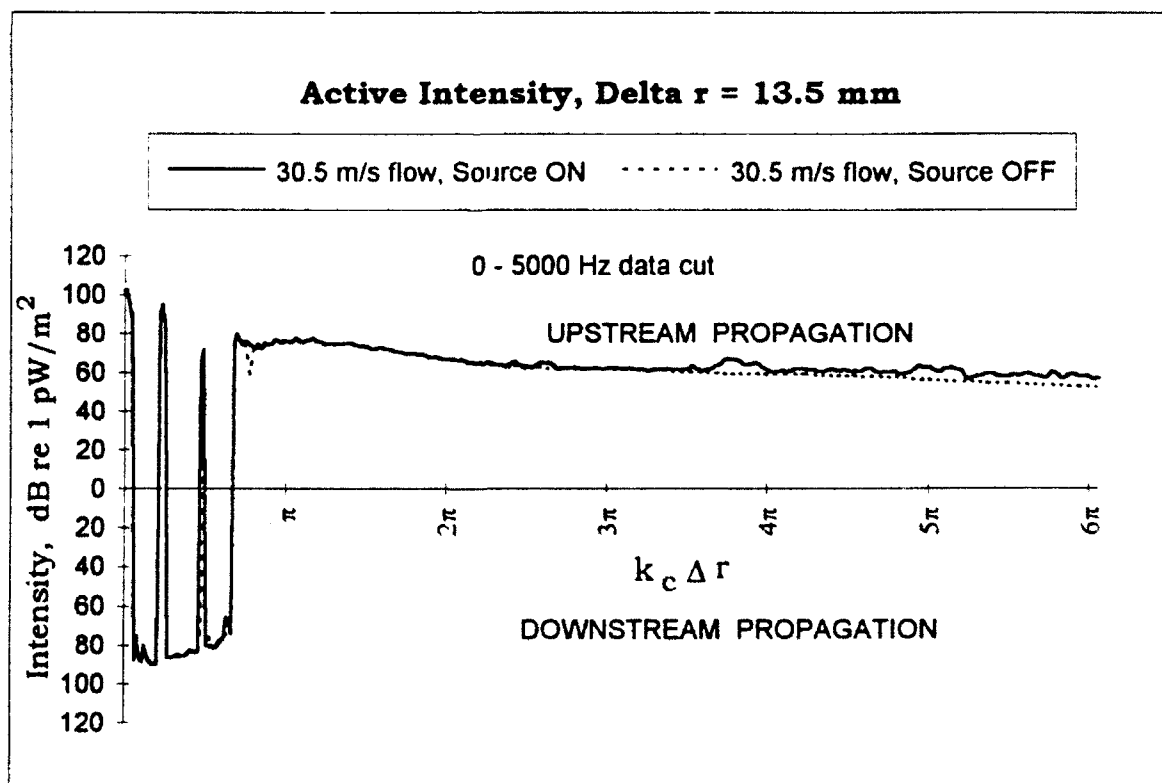
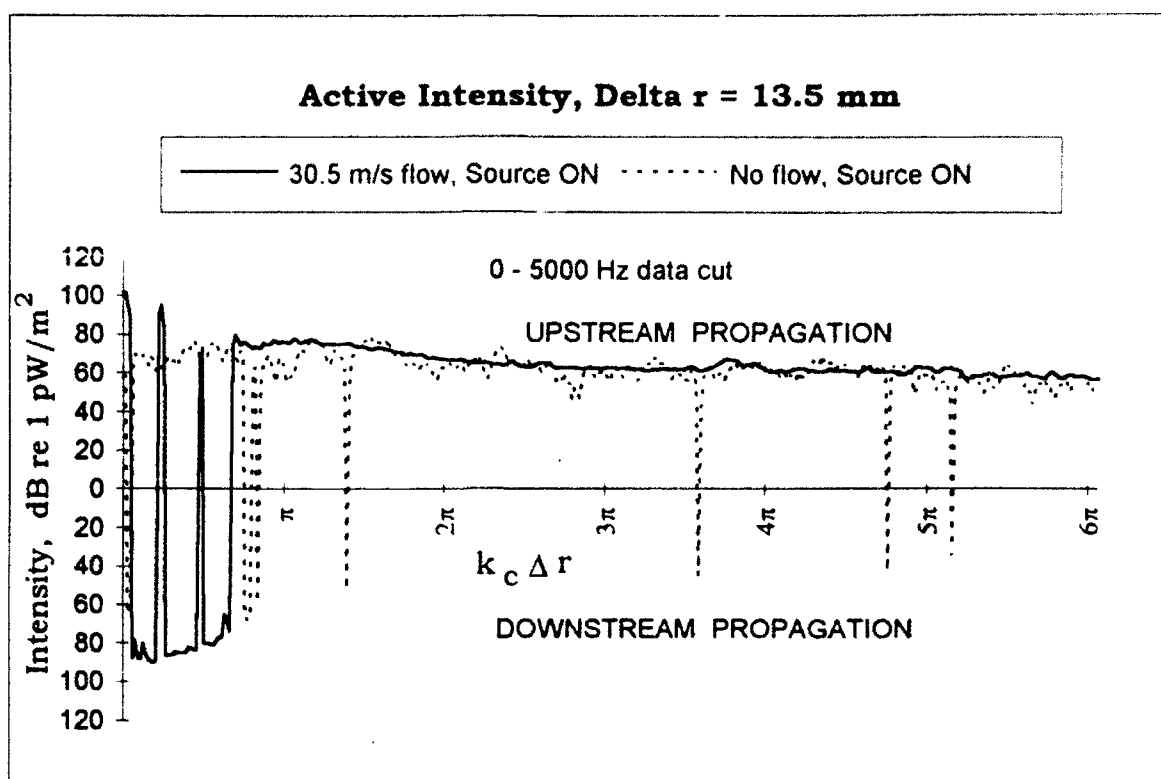


Figure B-9 Active Intensity, 30.5 m/s flow, Delta $r = 13.5$ mm

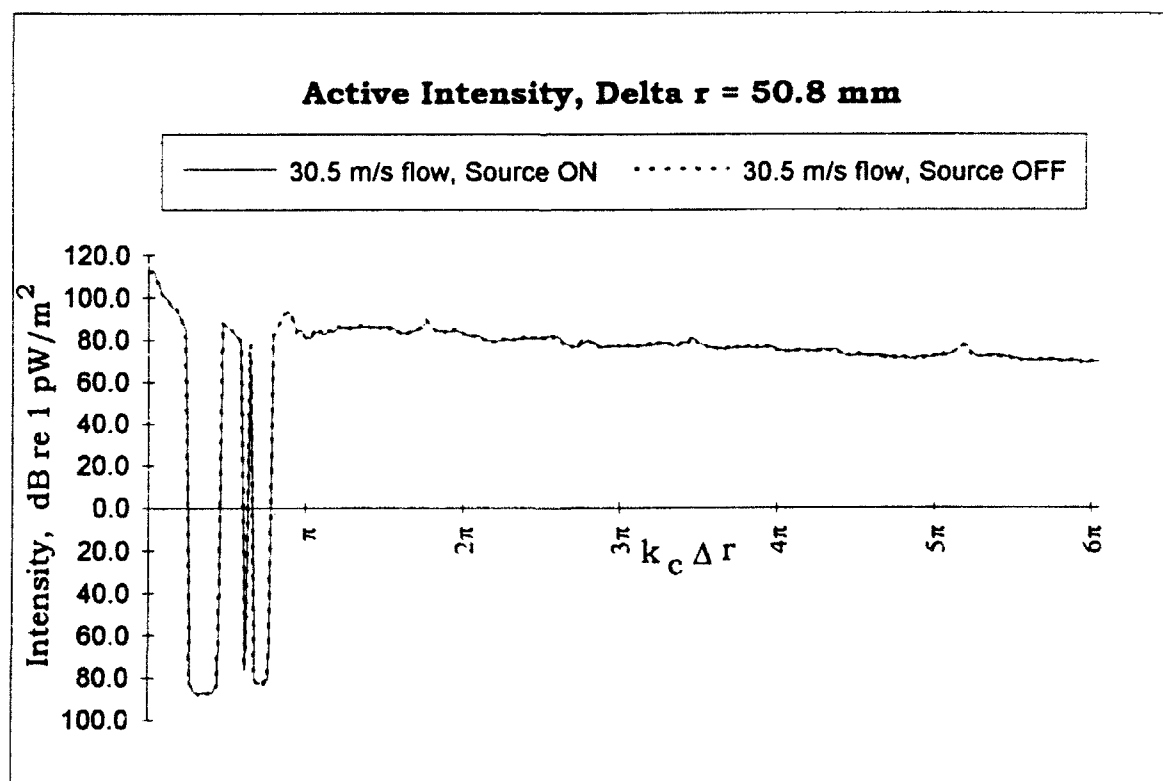
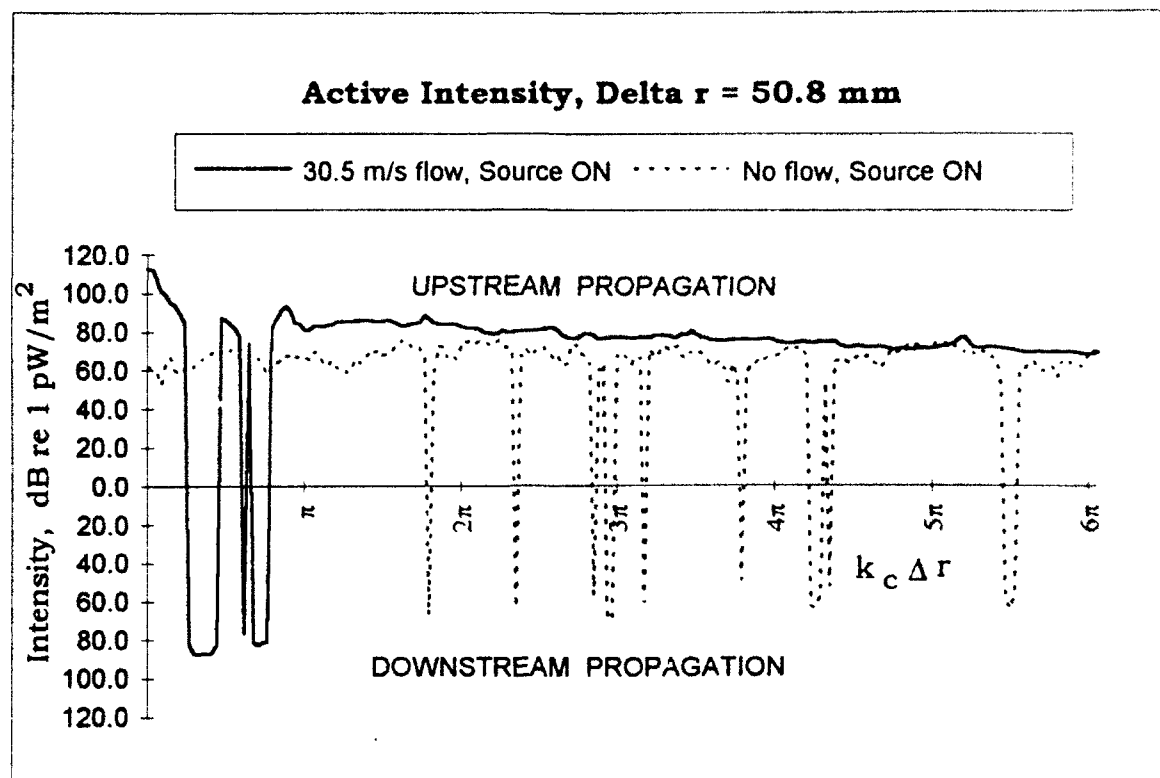


Figure B-10 Active Intensity, 30.5 m/s flow, Delta $r = 50.8$ mm

Appendix C
PRESSURE INTENSITY INDEX OVERLAY PLOTS

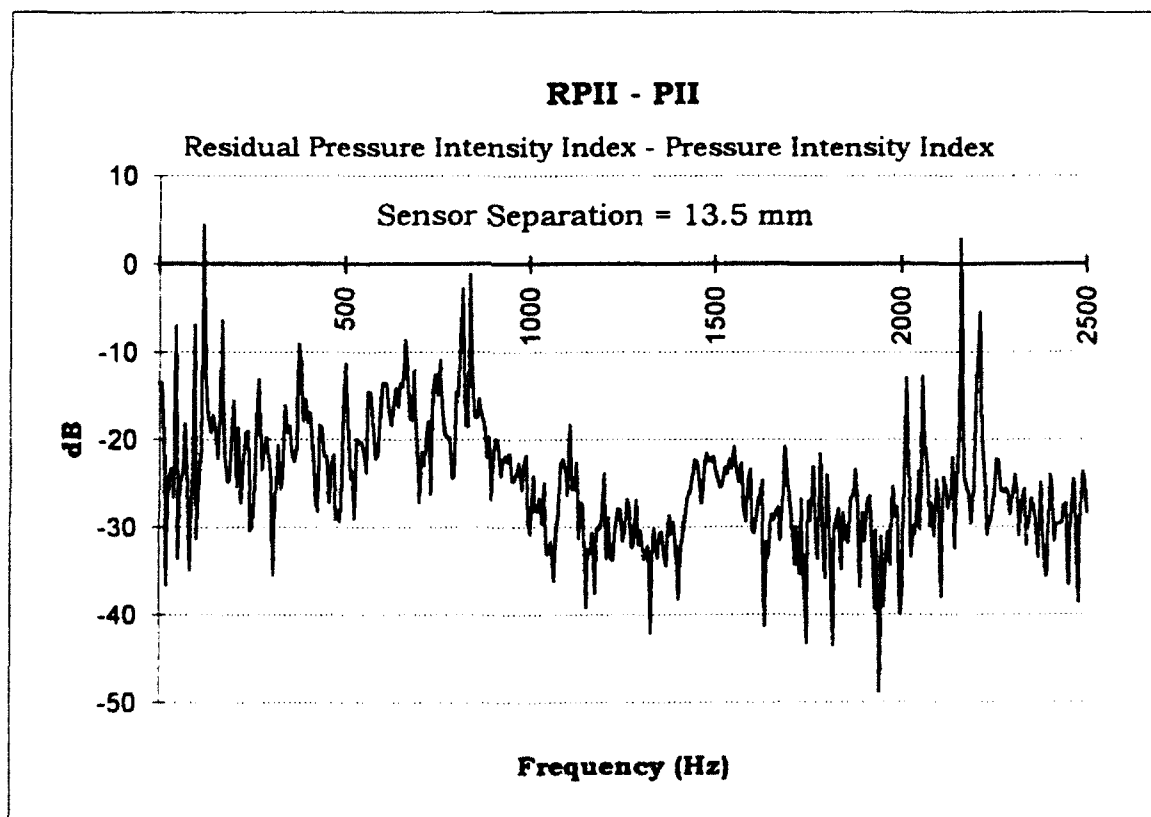
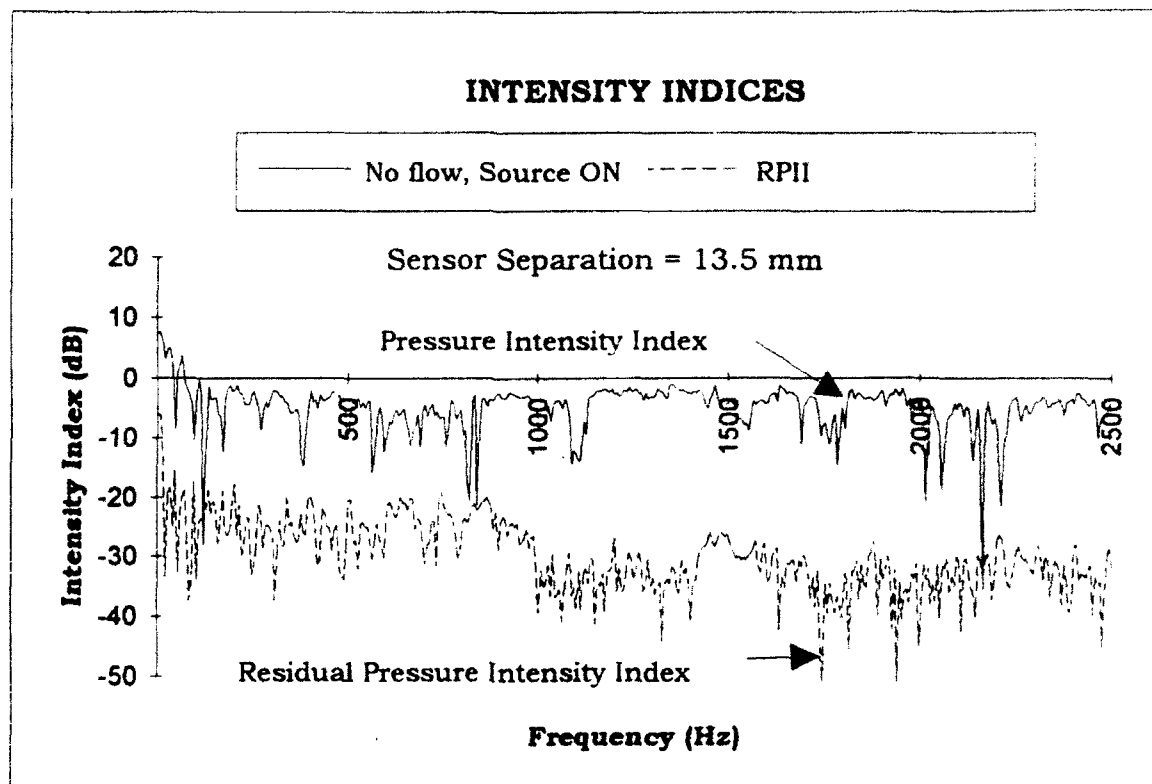


Figure C-1 Intensity Indices, no flow, Delta r = 13.5 mm

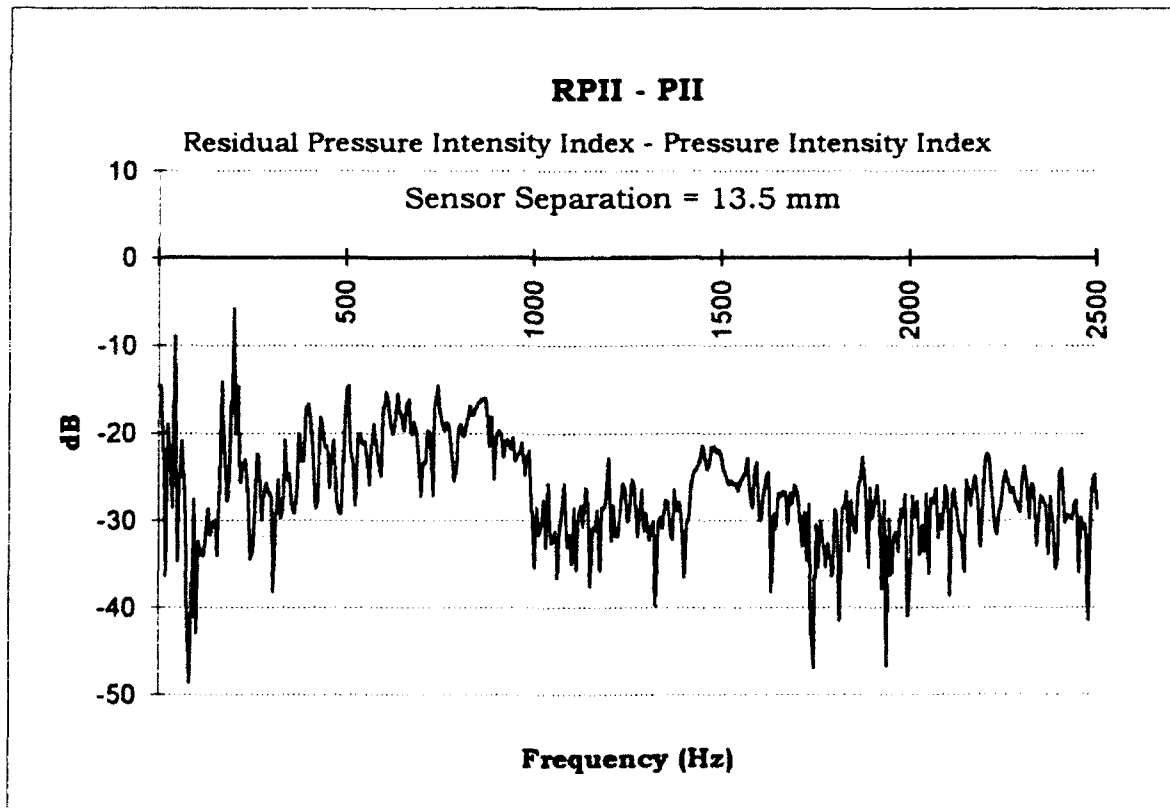
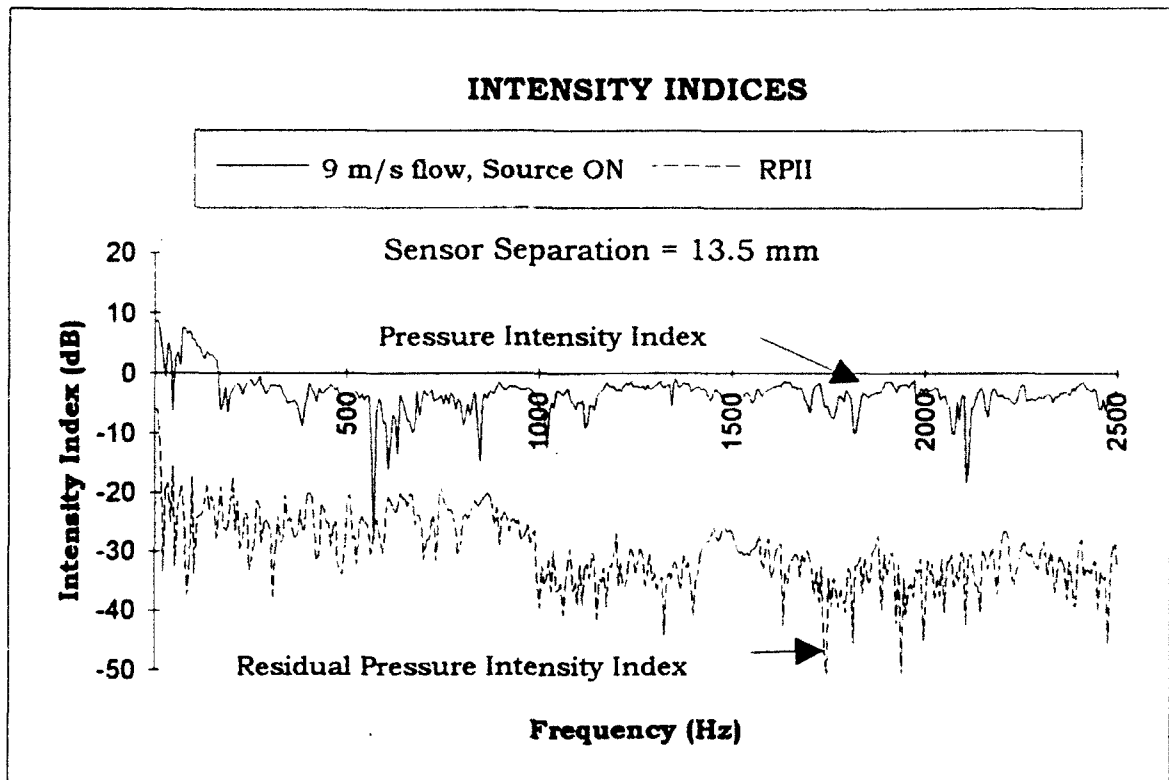


Figure C-2 Intensity Indices, 9 m/s flow, $\Delta r = 13.5$ mm

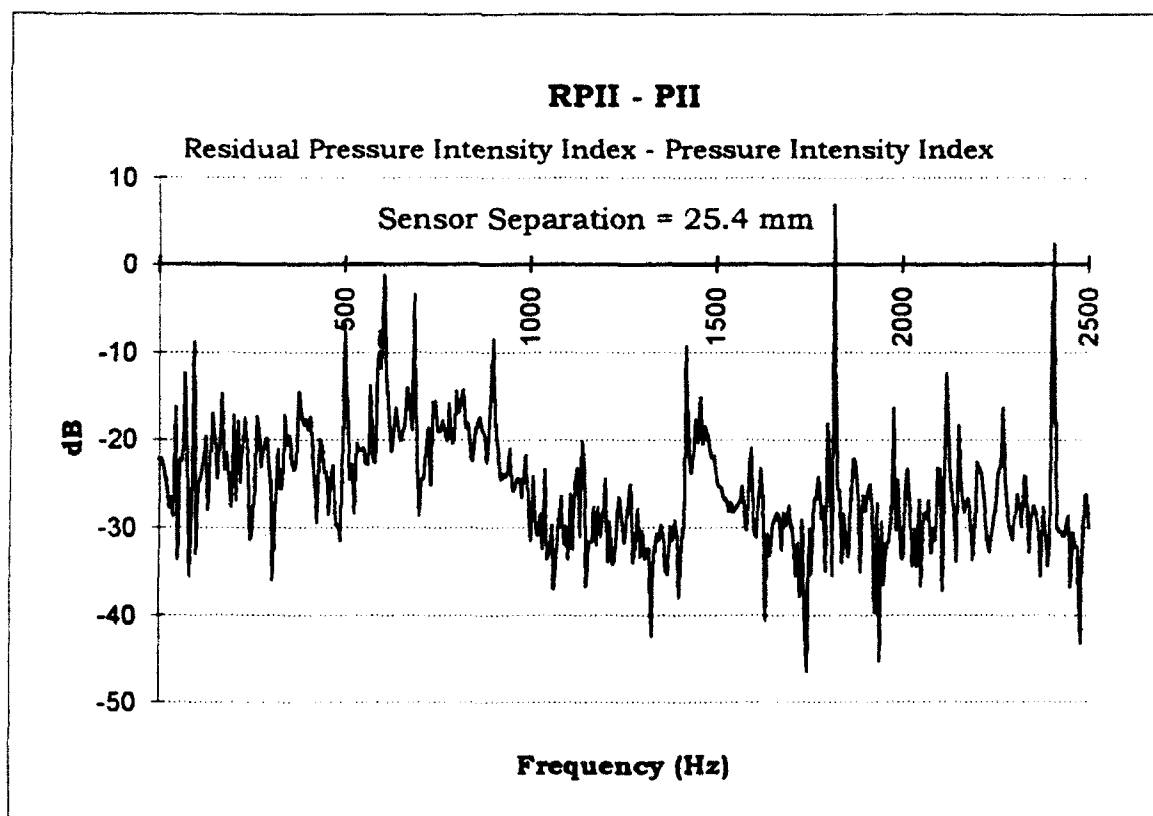
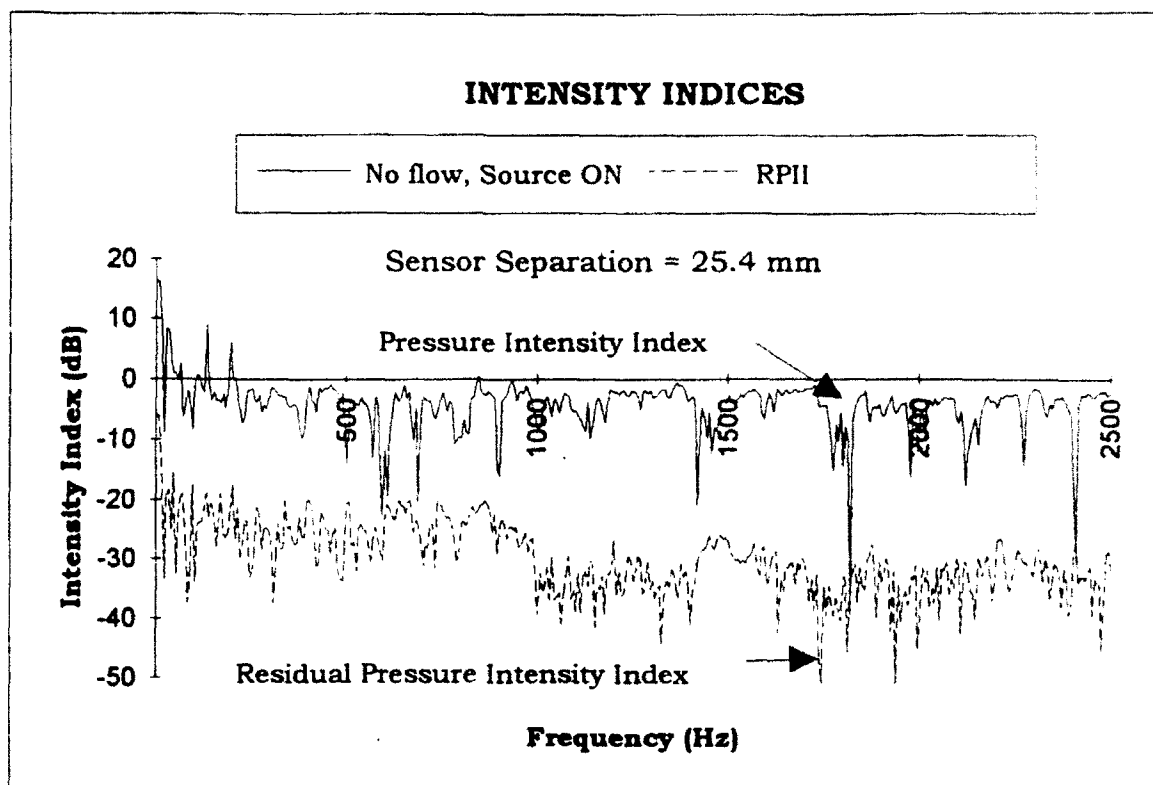


Figure C-3 Intensity Indices, no flow, Delta r = 25.4 mm

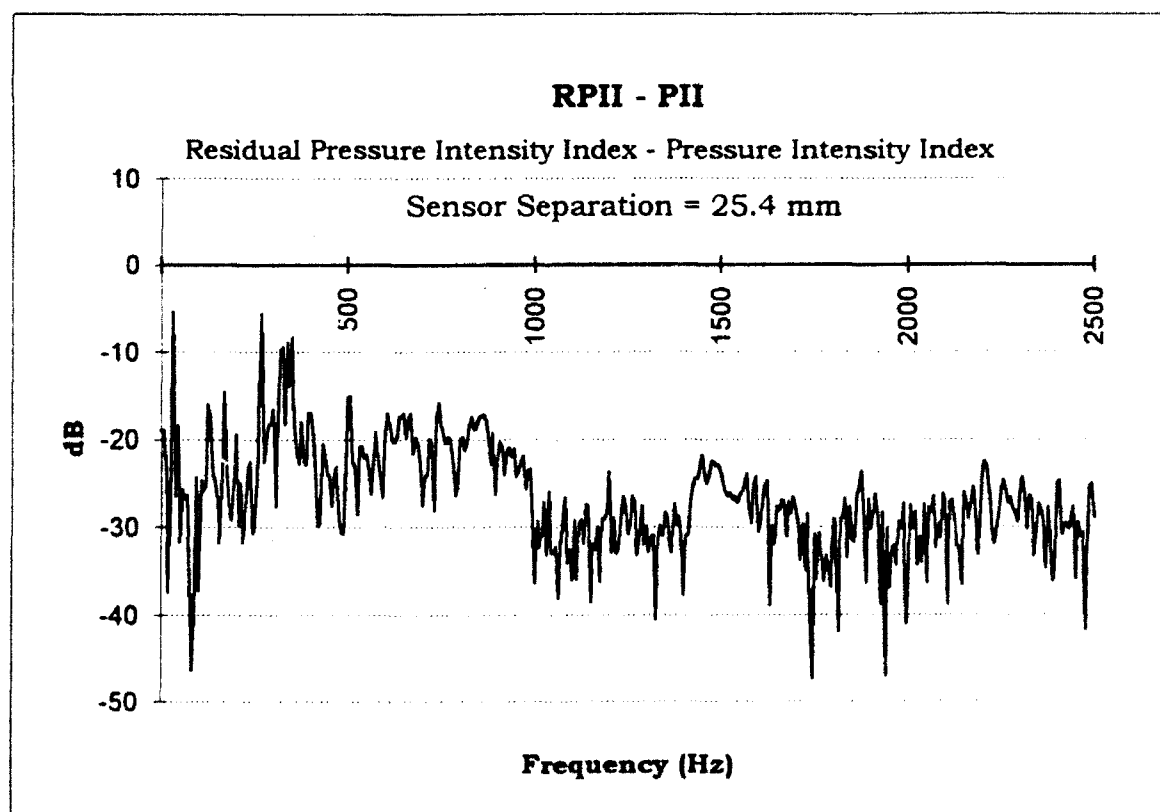
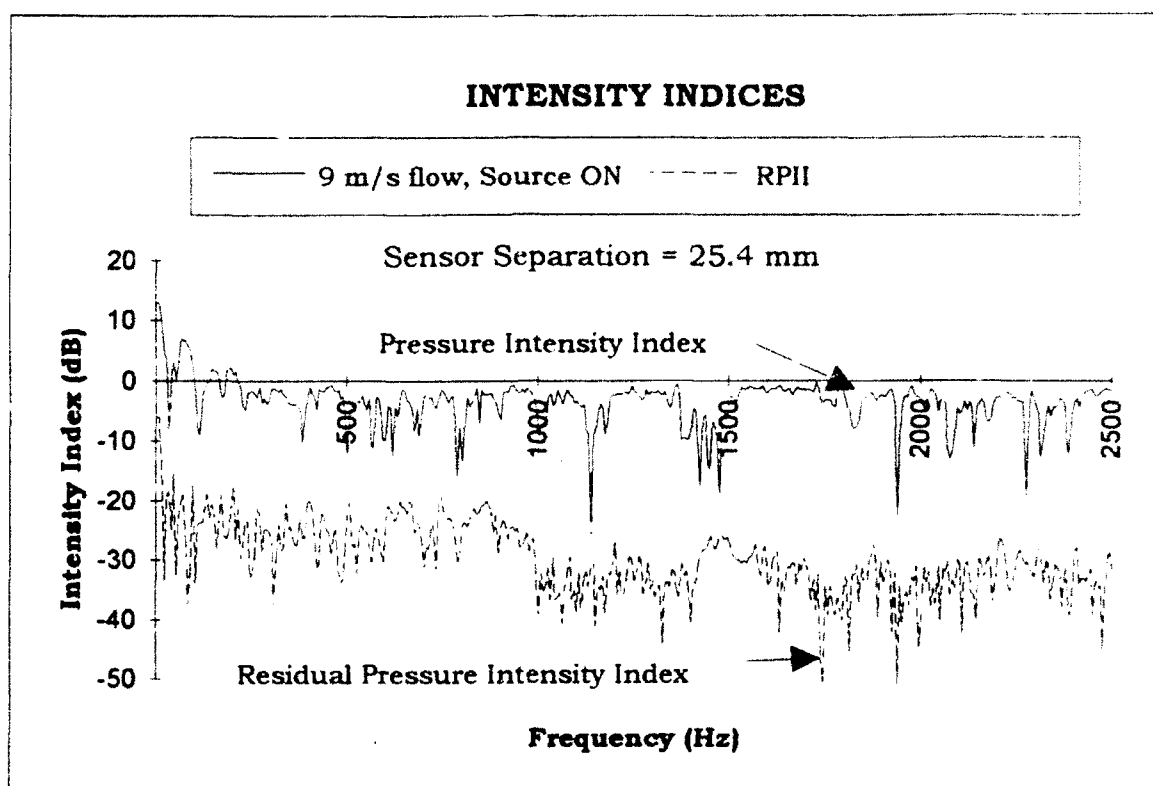


Figure C-4 Intensity Indices, 9 m/s flow, Delta r = 25.4 mm

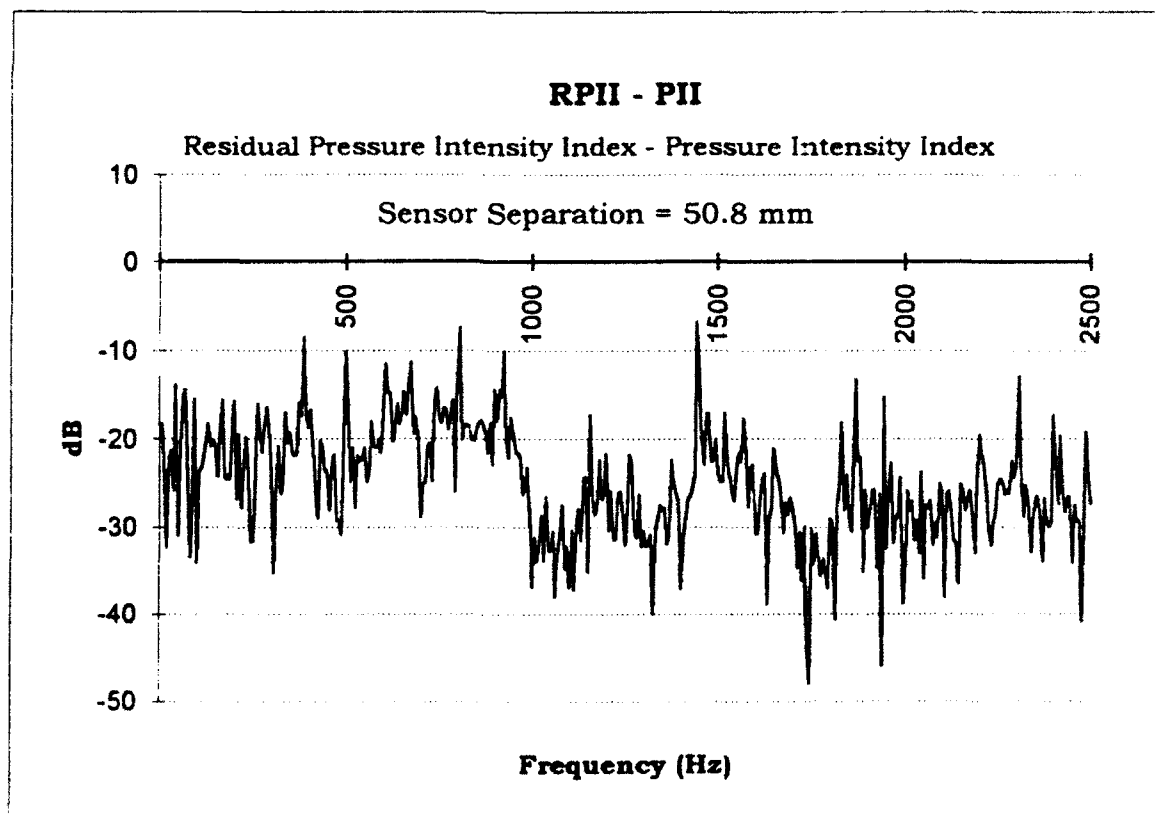
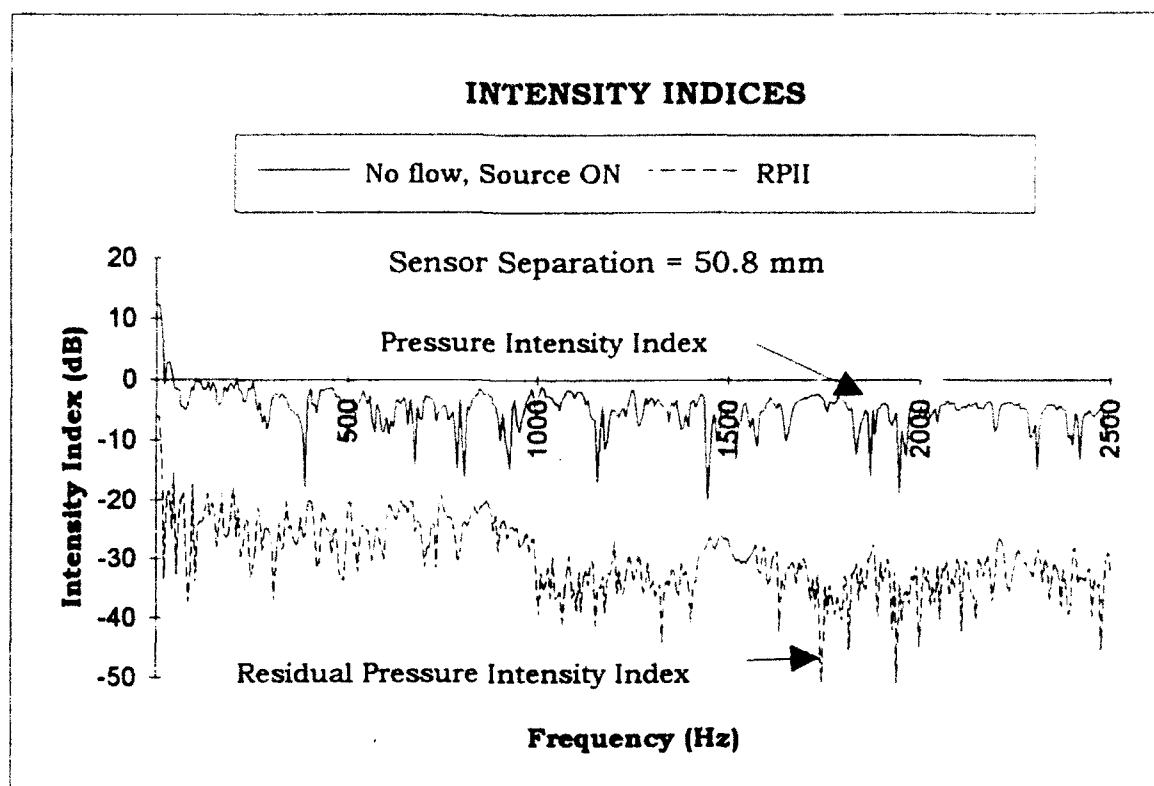


Figure C-5 Intensity Indices, no flow, $\Delta r = 50.8$ mm

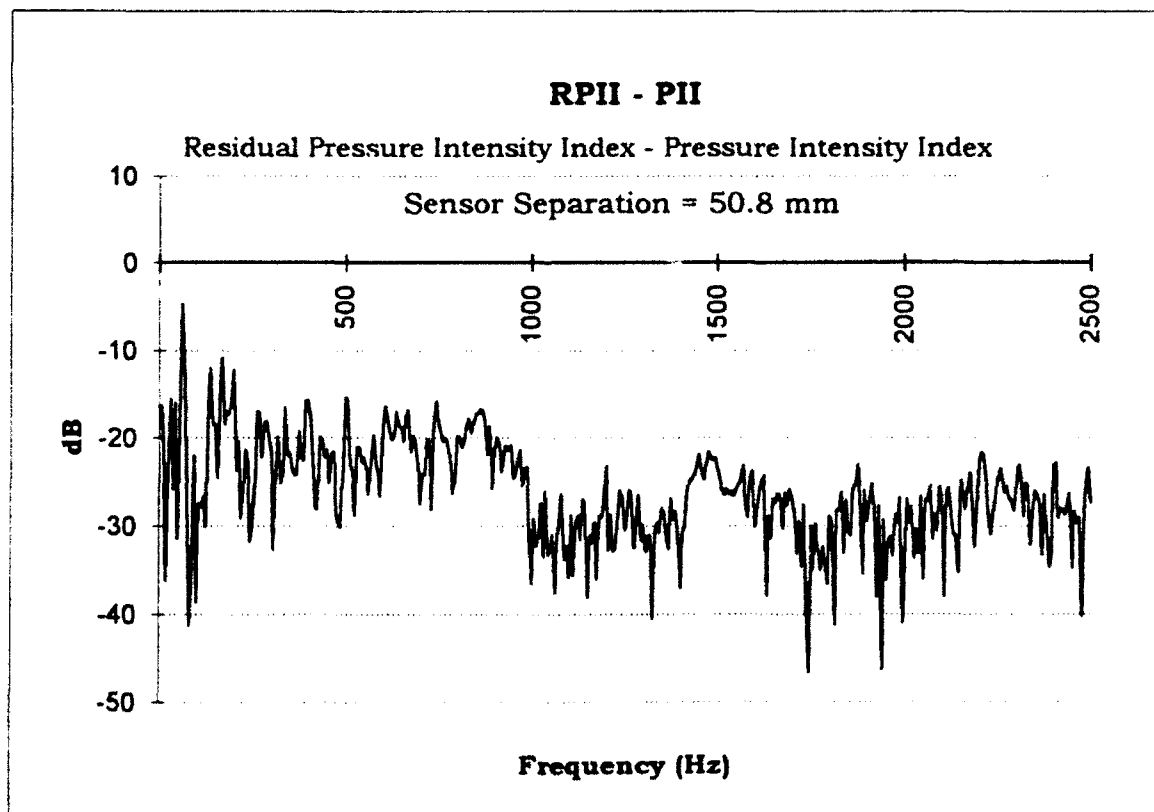
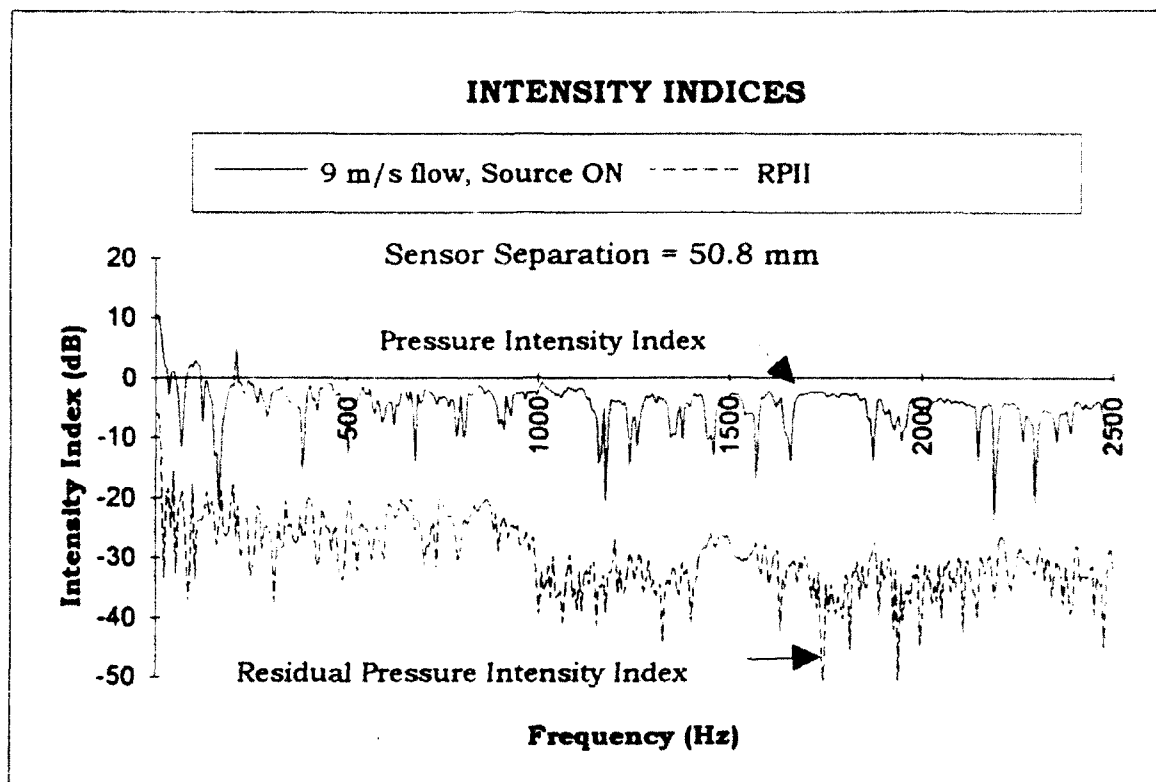


Figure C-6 Intensity Indices, 9 m/s flow, Delta r = 50.8 mm

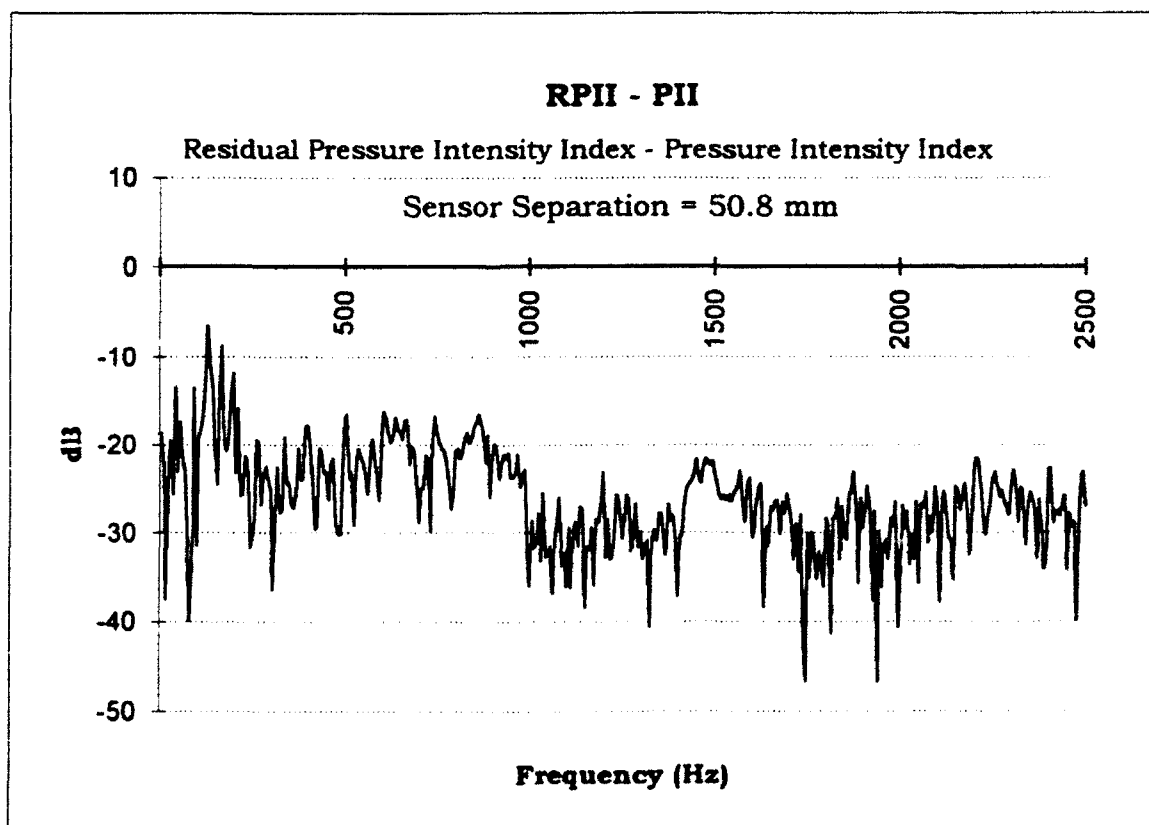
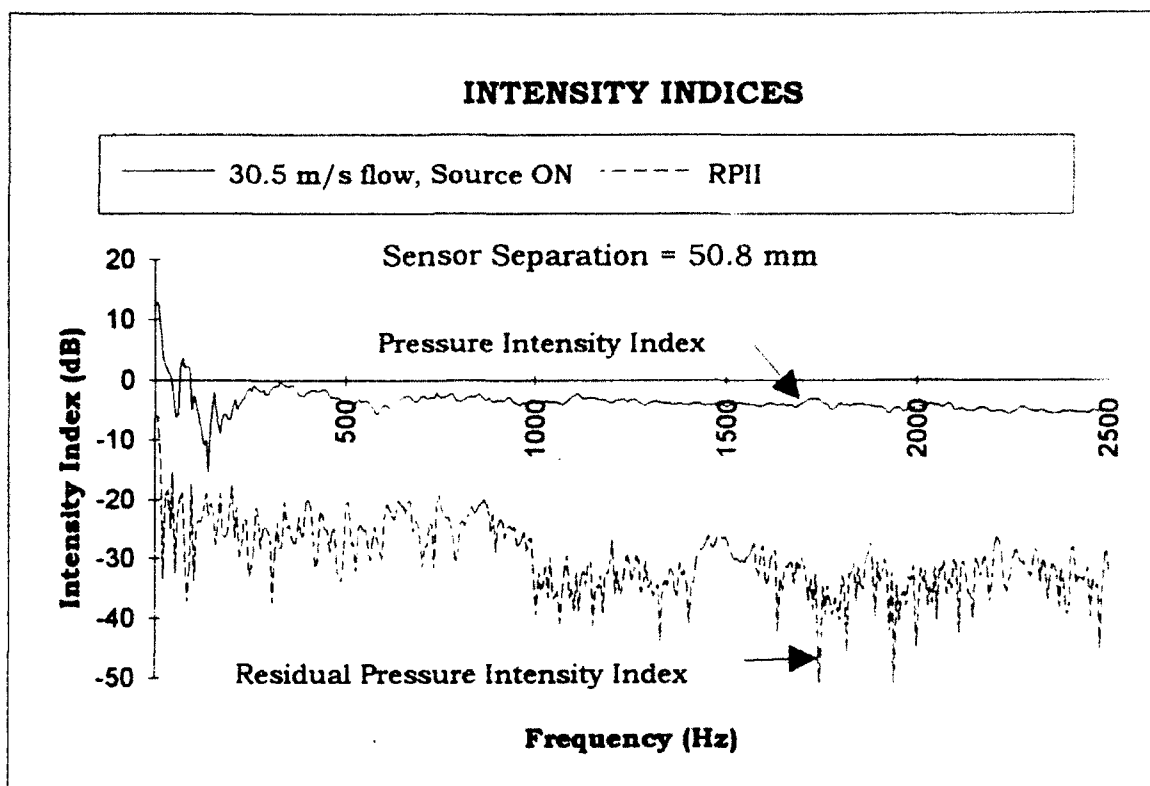


Figure C-7 Intensity Indices, 30.5 m/s flow, $\Delta r = 50.8$ mm